Master's thesis

NTNU
Norwegian University of Science and Technology
Faculty of Engineering
Department of Geoscience and Petroleum

Isak Hågensen

Landslide Susceptibility in Ottadalen, Norway: Investigating Forest Parameters and Spatio-Temporal Modelling with Logistic Regression and Random Forest Models

Master's thesis in Engineering Geology
Supervisor: Ola Fredin
Co-supervisor: Rosa Maria Palau Berastegui
June 2024

NTNU
Norwegian University of
Science and Technology

Isak Hågensen

Landslide Susceptibility in Ottadalen, Norway: Investigating Forest Parameters and Spatio-Temporal Modelling with Logistic Regression and Random Forest Models

Master's thesis in Engineering Geology
Supervisor: Ola Fredin
Co-supervisor: Rosa Maria Palau Berastegui
June 2024

Norwegian University of Science and Technology
Faculty of Engineering
Department of Geoscience and Petroleum

NTNU
Norwegian University of
Science and Technology

Abstract

The goal of this study is to further investigate multiple landslides in Ottadalen, Norway, following the extraordinary storm *Hans* in 2023. One interesting observation is that landslides initiated significantly more in birch forests compared to spruce and pine forests and non-forested areas. To advance this research and gain further insight into one of the most destructive natural hazards, an investigation into forests and forest parameters was conducted to understand their role in landslide triggering. Additionally, two different machine learning (ML) models, Logistic Regression (LR) and Random Forest (RF), were utilized to compare the two models and explore their predictive abilities on landslides. Dynamic parameters, such as rainfall and soil saturation, were implemented in the RF model. The approach proposes a method for generating spatio-temporal landslide susceptibility maps, which is still in the preliminary phase for ML-based methods.

The study found that in respective areas, the weight of the forest and a thin soil layer might have contributed to the larger number of landslides initiated in forested areas compared to non-forested areas. Birch forests, in particular, likely experienced more landslides due to these trees having leaves, larger canopies and a shallow root system. Also, birch forests covers a relatively large area in addition to the possibility of the forest being old – providing more weight and less stabilization due to root strength loss. Additionally, the performance of both the RF and LR models to predict landslides was considered excellent for both static and dynamic approaches, with a slightly better performance for the RF model. It seems likely that the models are efficient in producing accurate susceptibility maps over large regions. However, they are quite site- and storm-specific and would most likely not perform well if applied to other areas in Norway that rely on different input parameters, or other meteorological conditions than *Hans*.

Sammendrag

Målet med denne studien er å videre undersøke en rekke skred i Ottadalen, Norge, etter den ekstraordinære stormen *Hans* i 2023. En interessant observasjon er at skred initierte betydelig hyppigere i bjørkskog sammenlignet med gran- og furuskog samt områder uten skog. For å se nærmere på denne observasjonen og får å få en bedre forståelse rundt jordskred, en av de mest ødeleggende naturfarene, ble det gjennomført en undersøkelse av skog og skogparametere for å forstå deres rolle i utløsningen av jordskred. I tillegg ble to forskjellige maskinlæringsmodeller (ML), Logistisk Regresjon (LR) og Random Forest (RF), brukt for å teste deres prediktive evner på skred og for å muliggjøre en sammenligning av de to modellene. Implementeringen av dynamiske parametere, som nedbør og jordsmetning, i RF modellen ble også utført, og gir en foreslått metode for å generere dynamiske aktsomhetskart som fortsatt er i den innledende fasen når det gjelder ML-baserte tilnærminger.

Studien fant at i det respektive området kan vekten av skogen og det tynne jordlaget i området ha bidratt til det større antallet skred som initierte i skogkledde områder sammenlignet med ikke-skogkledde områder. Bjørkskog, spesielt, opplevde flere skred på grunn av at de har blader, større trekroner og et grunt rotsystem. Samtidig dekker bjørkskogen et relativt stort område og innehar muligheten for å være en gammel skog – som bidrar til mer vekt og mindre stabiliserende krefter på grunn av svakere rotstyrke. Resultatene fra både RF- og LR-modellene var utmerket, med tanke på både statisk og dynamisk tilnærming, med en noe bedre ytelse for RF-modellen. Modellene kan effektivt lage nøyaktige aktsomhetskart over store områder. De er imidlertid ganske sted- og stormsensitive og vil mest sannsynlig ikke prestere like godt hvis de brukes på andre områder i Norge som er avhengige av andre parametere, eller ved andre meteorologiske forhold enn *Hans*.

Forord

Oppgaven markerer enden på et femårig masterprogram i *Ingeniørgeologi* ved Norges teknisk-naturvitenskapelig universitet (NTNU) i Trondheim. Prosjektrådgiverne har vært professor Ola Fredin ved Institutt for geovitenskap og petroleum ved NTNU og Rosa Maria Palau Berastegui ved NGI.

Jeg ønsker å uttrykke min takknemlighet til Rosa Maria Palau Berastegui for å ha delt sin ekspertise og verdifulle veiledning kontinuerlig under arbeidet til enhver tid. Jeg ønsker også å takke henne for tålmodigheten, da hun har måttet holde ut med meg ikke bare under Masteroppgaven, men også under Speisaliseringprosjektet i høst. På samme premiss ønsker jeg å takke professor Ola Fredin, for uvurdelig oppfølging og innspill.

Jeg vil også uttrykke min takknemlighet til Anders Kleiven (NGI), Denise Rüther (HVL) og NVE for å ha levert et omfattende skredinventar som muliggjorde undersøkelsen. Samtidig må jeg få takke Zhongqiang Liu for gode svar på spørsmål om Machine Learning. Jeg vil også takke Meteorologisk Institutt, Norges Geologiske Undersøkelse, Høydedata og Norsk Institutt for Bioøkonomi for å holde data tilgjengelig og til bruk for alle.

Til slutt ønsker jeg å takke alle medstudenter, venner, familie, kjæreste, kaffe og selvfølgelig NTNU, som har gjort mine fem år i Trondheim til en uforglemmelig opplevelse jeg aldri ville vært foruten.

Table of contents

List of Figures viii

List of Tables xiv

1 Introduction 1

1.1 Background . . . 2

1.2 Research questions . . . 3

1.3 Thesis structure . . . 4

2 State of the art 5

2.1 Landslide classifications . . . 5

2.1.1 Shallow landslides . . . 7

2.1.2 Debris flow . . . 7

2.1.3 Debris slide . . . 8

2.1.4 Debris avalanche . . . 8

2.1.5 Debris flood . . . 8

2.2 Landslide causes and triggers . . . 9

2.3 Landslide susceptibility, hazard assessment and risk zoning . . . 10

2.3.1 Scales . . . 10

2.3.2 Inventory . . . 11

2.3.3 Susceptibility maps . . . 11

2.3.4 Hazard and risk maps . . . 12

2.4 Machine learning . . . 12

2.4.1 Random Forest algorithm (RF) . . . 13
2.4.2 Logistic Regression algorithm (LR) . . . 14
2.4.3 Machine learning challenges . . . 15
2.4.4 Model performance assessment . . . 17
2.5 Forest parameters . . . 21
2.5.1 Norwegian forests . . . 22
2.5.2 Root cohesion . . . 23
2.5.3 Tensile strength . . . 23
2.5.4 Underground biomass . . . 24

3 Study area **25**

3.1 Geology . . . 26
3.1.1 Bedrock geology . . . 26
3.1.2 Surficial deposits . . . 26
3.2 Climate . . . 27
3.3 Description of the storm *Hans* . . . 28

4 Data and Methods **30**

4.1 Data . . . 30
4.1.1 Terrain data . . . 30
4.1.2 Landslide inventory data . . . 31
4.1.3 Precipitation data . . . 34
4.1.4 Soil saturation degree data . . . 34
4.2 Methods . . . 36

4.2.1 Landslide frequency 36
4.2.2 Computation of parameters with GIS tools 37
4.2.3 Method to obtain root cohesion 38
4.2.4 Preparation of total dataset 39
4.2.5 General preparation of training and test set 41
4.2.6 Method to assess static landslide susceptibility 42
4.2.7 Method to assess dynamic landslide susceptibility 45

5 Results **49**

5.1 Analysis of forest parameters 49
5.2 Results static susceptibility maps 57
5.2.1 Maps 57
5.2.2 Evaluation of model performance 59
5.3 Results of dynamic susceptibility maps 62
5.3.1 Maps 62
5.3.2 Evaluation of model performance 66

6 Discussion **72**

6.1 Forest and terrain influence on landslide initiations 72
6.1.1 Birch forests vs. spruce and pine forests 75
6.2 Static susceptibility maps 77
6.2.1 Model performance 77
6.2.2 Input parameters 78
6.2.3 Limitations 80

6.3 Dynamic susceptibility maps 81

6.3.1 Model performance 82

6.3.2 The role of input parameters 83

6.3.3 Limitations 84

6.4 Future studies 85

6.4.1 Future research with significant resources 85

6.4.2 Future research (master theses) with limited resources 86

7 Conclusion **88**

Bibliography **90**

8 Appendix **I**

8.1 Study area with 4 points I

8.2 Analysis of landslide inventory data and terrain conditions II

8.3 Analysis of the hydrometeorological conditions leading to landslides . . . IX

List of Figures

1 The Varnes classification system distinguishes type of landslides based on the material (rock, debris or earth) and the type of movement. The illustration is based on Varnes (1978) and Cruden and Varnes (1996). . . . 6

2 Illustration of the Random Forest algorithm. The figure is taken from Merghadi et al. (2020). 14

3 Illustration of the Sigmoid function applied to the linear fitting function for the Logistic Regression algorithm. The figure is taken from Merghadi et al. (2020). 15

4 Illustration of the Reciever Operating Characteristic (ROC) curve. The Area Under the Curve (AUC) is the gray area, and the yellow dotted line indicates a random classifier. The ROC curve is generated based on the False Positive Rate (FPR) on the x-axis and the True Positive Rate (TPR) on the y-axis. The orange star in the top left corner indicates a perfect classifier. The figure is taken from MathWorks (n.d.). 20

5 Map of the study area. The study area is in Ottadalen, indicated by the red square. The brown dots are release points of landslides. North arrow and scale bar is added to both maps. Vågåmo is marked with a blue star. The background map is the OpenStreetMap from ArcGIS Pro. 25

6 Map showing the meteorological situation of *Hans* over Norway at 11 a.m. for three consecutive days, 7-9 August 2023. The black lines are showing borders, the blue lines are showing the pressure contour lines in Pascal and the red areas are showing precipitation. The colorbar is indicating the amount of rain in mm. The map is based on data from METNorway (2023). 29

7 Flow chart showing the process from data collection in (1.) to generating landslide susceptibility maps in (2). The flow chart offers an overview, but especially (2.) should be linked to the method descriptions for both static and dynamic approaches to provide a complete understanding, as these approaches differ slightly. 40

8 Illustration of three maps showing slope angle (top), slope aspect (middle) and flow accumulation (bottom). Corresponding values and colors are described in the legend. Vågåmo is marked with a blue star and the landslides are marked as brown points. 43

9 Illustration of three maps showing soil type (top), tree type (middle) and root cohesion (bottom). Corresponding values and colors are described in the legend. Vågåmo is marked with a blue star in the maps and the landslides are marked as brown points. The background map is the OpenStreetMap in ArcGIS Pro. 44

10 Illustration of the precipitation from August 7 at the top to August 10 at the bottom. The legend is the same for all figures and going from 0 mm (red colors) to 108 mm (blue colors). Vågåmo is marked with a star, and landslides as brown points. 47

11 Illustration of the soil saturation degree from August 7 at the top to August 10 at the bottom. The legend is the same for all figures and going from 32% (red colors) to 128% (black colors). Vågåmo is marked with a star, and landslides as brown points. 48

12 a) is illustrating the number of landslides versus the tree type, while b) is showing the number of landslides versus the leaves coverage. The blue bars are showing the amount of landslides and the red line is showing the landslide frequency, which indicates how “often” landslides initiate for the respective parameters, see Equation 6 for description. 50

13 a) shows trees with a diameter at breast height (1.3 meter above ground) bigger than 5 cm and b) shows trees with a diameter bigger than 16 cm at breast height. The blue bars are showing the landslide amount and the red, dotted line is indicating the landslide frequency, which indicates how "often" landslides initiate for the respective parameters, see Equation 6 for description. 52

14 a) is illustrating the number of landslides versus the mean tree height (dm), while b) is showing the number of landslides versus the mean tree diameter (cm) at breast height (1.3 meters above ground). The blue bars are showing the amount of landslides and the red line is showing the landslide frequency, which indicates how "often" landslides initiate for the respective parameters, see Equation 6 for description. 54

15 a) shows the mean tree diameter (cm) distribution at breast height (1.3 meters above ground) for the different trees while b) shows the mean tree height (m) distribution. The blue bars shows spruce, the green bars shows pine and the orange bars shows birch (deciduous) inside the study area. . 56

16 Comparison of susceptibility maps generated from Random Forest (a) and Logistic Regression (b). The range between 0-0.25 probability has no color in the map. This was done to emphasize the other probabilities. Vågåmo is marked with a blue star, and a north arrow and scale bar is placed inside the map. The background map is the OpenStreetMap in ArcGIS Pro. 58

17 Area percentages of the landslide probabilities shown in Figure 16. The map generated with Random Forest is shown as green bars and the map generated with Logistic Regression is shown as red bars. The respective probability zones are indicated on the x-axis and the area percentages are shown on the y-axis. 59

18 Reciever Operating Characteristic (ROC) curve of Random Forest (green) and Logistic Regression (red) models, indicating the relationship between True Positive Rate and False Positive Rate. The Area Under the Curve (AUC) is indicated in the legend and a random predictor model is shown as a grey, dotted line. 61

19 Comparison of susceptibility maps generated from Random Forest model for August 7 and 8. The range between 0-0.1 probability has no color in the map. The background map is the OpenStreetMap in ArcGIS Pro. . . . 63

20 Comparison of susceptibility maps generated from Random Forest model for August 9 and 10. The range between 0-0.1 probability has no color in the map. The background map is the OpenStreetMap in ArcGIS Pro. . . . 64

21 Percentages of the different landslide probabilities during August 7-10. The respective probability zones are indicated on the x-axis and the area percentage is shown on the y-axis. 65

22 Susceptibility maps and corresponding landslide initiation points on different dates, August 8 and 9. The range between 0-0.1 probability has no color in the map. The background map is the OpenStreetMap in ArcGIS Pro. 66

23 Receiver Operating Characteristic (ROC) curve of August 8 and 9 with Random Forest. The ROC curve is indicating the relationship between True Positive Rate and False Positive Rate. The Area Under the Curve (AUC) is indicated in the legend and a ROC curve equal to 0.5 is shown as a grey, dotted line. 69

24 Discrimination Diagram for August 7 to 10. The likelihood represent the probability that a given prediction falls within a specific bin. The specific bins of probability for landslides is shown on the x-axis. The orange bars are cases of “Not Observed” cases (Not landslides). “Observed” cases are shown as blue bars and indicate cases of landslides. 70

25 Picture of a landslide in Ottadalen after *Hans* in August, 2023. The picture is taken by Anders Kleiven, NGI. The thin soil layer on top of bedrock is clearly seen along with quite dense forest in the area. 73

26 Box plot illustrating the distribution of landslide occurrences based on slope angle, categorized by whether they initiated in forested or non-forested areas. Outliers are represented as dots outside the box, and the orange line indicates the median value. 75

27 Map of the study area. The study area is in Ottadalen, indicated by the red square. The brown dots are release points of landslides. North arrow and scale bar is added to both maps. Vågåmo, Otta and point 1-4 is marked with a red star. This is because the locations and points are used later in the report. The background map is the OpenStreetMap from ArcGIS. . . . I

28 Stack bar showing amount and type of landslides based on slope aspect or slope angle. Abbreviations: DFd - debris flood, DFw - debris flow, DS - debris slide. Overview of aspect division is found in Table 7. III

29 Stack bar showing amount and type of landslides based on soil type or area type. Abbreviations: DFd - debris flood, DFw - debris flow, DS - debris slide, WM - weathered material, MMD - mass movement deposits, Thin veg. cover - thin vegetation cover. IV

30 Stack bar showing amount and type of landslides based on forest type. Abbreviations: DFd - debris flood, DFw - debris flow, DS - debris slide, Mix P & S - mix of pine and spruce. V

31 Graphs showing landslide amount and landslide frequencies of soil type and tree basal area at breast height. Blue bars are showing the amount of landslides and the red line is showing the frequency of the landslides. . . VII

32 Graphs showing landslide amount and landslide frequencies of slope aspect, slope angle and flow accumulation. Blue bars are showing the amount of landslides and the red line is showing the frequency of the landslides. VIII

33 Figure showing the 100 year return period for a duration of 24 hours in the study area. The four NGI points and Vågåmo is marked as red dots and can also be seen in Figure 27. The red square is the study area. Northing and easting are shown on the y- and x- axis, respectively. Amount of precipitation [mm] is shown in the colorbar. IX

34 Figure showing precipitation in mm as histograms, soil saturation degree in % as orange line and the T = 100 years as a red, dotted line which indicates the 100 year return period for the specific point. The time period is starting from 1 July and going until 16 August 2023 at 24 hours. Time is spanning from 00:00 until 24:00 for each day. The plots are representing points 1 and 2 from Figure 33. X

35 Figure showing precipitation in mm as histograms, soil saturation degree in % as orange line and the T = 100 years as a red, dotted line which indicates the 100 year return period for the specific point. The time period is starting from 1 July and going until 16 August 2023. Time is spanning from 00:00 until 24:00 for each day. The plots are representing points 3 and 4 from Figure 33. XI

36 Soil legend from NGU part 1 XII

37 Soil legend from NGU part 2 XIII

List of Tables

1 Confusion matrix representing True negative (TN), False negative (FN), False positive (FP) and True positive (TP). The green cells indicate a correct classification, while the white cells indicates an incorrect classification. 17

2 Performance indicators used to evaluate the performance of the models. The performance indicators are based on the confusion matrix. The table is inspired by Chawla et al. (2002) and Liu et al. (2021). 18

3 Overview of the collected data used for both landslide investigation and ML methods. The resolution and source of the data is stated. The table is taken from Hågensen (2023). 30

4 Summary of data points provided by contributors to the inventory within the study area. 33

5 Overview of amount of landslides on respective dates based on the assumptions mentioned and the landslide inventory provided. 33

6 Average, modelled precipitation and soil saturation over the total study area for each day. The table illustrate the reference time for the different dates, and the averaged amount of precipitation and soil saturation for each day. 35

7 Slope aspect with corresponding degrees. 37

8 Values used to generate the root cohesion suggested by Capobianco et al. (2024) are shown. Reference to Norway Spruce: Bischetti et al. (2007). Reference to Pine: Genet, Stokes, Salin et al. (2005). Reference to Deciduous: Mao et al. (2012). 39

9 Values indicating the Variance Inflation Factor (VIF) and the Feature Importance for Random Forest and Logistic Regression. 60

10 Confusion Matrix from Random Forest and Logistic Regression, indicating the amount of landslide pixels predicted as TN, FP, FN, and TP. . . . 60

11 Performance indicator values based on the confusion matrix in Table 10. 61

12 Overview of actual landslide pixels overlaid on the predicted maps generated by the Random Forest (RF) and Logistic Regression (LR) models. . 62

13 Feature importance from Random Forest model with dynamic approach. . 67

14 Confusion Matrix from Random Forest, indicating the amount of landslide pixels predicted either as TN, FP, FN, and TP for August 7 and 8. . . 67

15 Confusion Matrix from Random Forest, indicating the amount of landslide pixels predicted either as TN, FP, FN, and TP for August 9 and 10. . 67

16 Performance indicator values of August 8 and 9 based on the confusion matrices in Table 14 and 15. 68

17 Overview of actual landslide pixels on respective dates from the inventory overlaid on the predicted rasters generated by the Random Forest model for August 8 and 9. 71

18 Different landslide types that initiated inside the study area. The landslide types and amount was extracted from the landslide inventory. The landslide types are also classified in Hungr et al. (2013). II

19 The frequency of landslides is shown for LULC, soil type and forest type. VI

Nomenclature

AUC - Area Under the Curve

DTM - Digital Terrain Model

DFd - Debris flood

DFw - Debris flow

DS - Debris slide

EI - Efficiency Index

FN - False Negative

FP - False Positive

FPR - False Positive Rate

GIS - Geographic Information System GWB - Gridded Water Balance

HVL - Western Norway University of Applied Sciences

IPCC - The Intergovernmental Panel on Climate Change

LiDAR - Light Detection and Ranging

LR - Logistic Regression

LULC - Land Use and Land Cover

MET - Meteorological Institute

ML - Machine Learning

MMD - Mass Movement Deposits

MORLE - Multiple-Occurrence Regional Landslide Events

NIBIO - Norwegian Institute of Bioeconomy Research

NGI - Norwegian Geotechnical Institute

NGU - Norwegian Geological Survey

NVE - The Norwegian Water Resources and Energy Directorate

RF - Random Forest

ROC - Reciever Operating Characteristic

SMOTE - Synthetic Minority Oversampling Technique

THREDDS - Thematic Real-time Environmental Distributed Data Service

TN - True Negative

TP - True Positive

TPR - True Positive Rate

VIF - Variance Inflation Factors

WM - Weathered Material

1 Introduction

Landslides are among the most common geohazards globally, causing significant damage to both life and property (W. Chen, Z. Sun et al. 2019; W. Chen, Xie et al. 2017; Dai et al. 2002; Merghadi et al. 2020). It is established that extreme weather bringing significant amounts of precipitation is the most common trigger for landslides (Bogaard and Greco 2016; Gariano and Guzzetti 2016; Nocentini et al. 2023; Sandersen et al. 1997; Wieczorek and Glade 2005). Norway's landscape, characterized by high peaks, low valleys and steep terrain throughout its expanse are expected to experience more intense precipitation and higher temperatures due to climate change (Hanssen-Bauer et al. 2015; Ramberg et al. 2006). Increased urbanization, deforestation and precipitation in the future will likely lead to more frequent and severe landslide events (Ado et al. 2022; Mondini et al. 2023; Ren et al. 2024).

Hans was an extraordinary storm that affected large parts of southeastern Norway between 7-9 August 2023, bringing substantial amounts of precipitation (Granerød et al. 2023). Due to climate change, it is reasonable to assume that possible "normal" storms in the future will be similar to *Hans*. *Hans* initiated a multiple-occurrence regional landslide event (MORLE), which can be defined as several landslides occurring almost simultaneously over a large area (Crozier 2005). During *Hans*, 2900 people had to be evacuated from their homes in the affected areas (Revheim-Rafaelsen et al. 2023). The material cost of *Hans* turned out to be 1.8 billion Norwegian kroner (Torkelsen et al. 2023).

The wetter, wilder climate of the future is, in other words, already affecting people and infrastructure today. The current expected cost of weather and natural disaster damages in Norway is 5.5 billion Norwegian Kroner per year, and this is projected to rise to 19 billion by 2100 if our current level of mitigation efforts remains unchanged (Pedersen et al. 2024). Further preventing activities is therefore important, but to a broader, better and with more urgency than we see today. These measures include mapping and securing landslide-prone areas, as well as improving warning systems and preparedness (Pedersen et al. 2024).

1.1 Background

It is well known that forests contribute positively to the stabilization of slopes (Cohen and Schwarz 2017; Dorren and Schwarz 2016; Z. Guo et al. 2023; Saito et al. 2017; Wu et al. 1979). Tree roots contribute to removal of water from the soil due to evapotransporation and provide additional lateral reinforcement (Ziemer 1981b). However, in the study done by Hågensen (2023) (literature review preceding this Master's thesis), it was shown that a large number of the reported landslides initiated in forested areas compared to non-forested areas in Ottadalen, Norway. The study also highlighted that generally deciduous forests had a significantly higher amount of landslides compared to spruce and pine forests. Because of this, a further investigation was deemed interesting and necessary.

Prediction of when and where landslides will occur is a key ability for the future, and up to date knowledge about landslides may aid in minimizing the material cost and danger to human lives (Bogaard and Greco 2016; Mondini et al. 2023). Regional landslide susceptibility mapping is a critical step in the prediction and mitigation of future landslide occurrences (Merghadi et al. 2020). Susceptibility maps show the probability of spatial occurrence of landslides given a set of geoenvironmental conditions (Guzzetti et al. 2006). However, generating accurate landslide susceptibility maps for a large area is difficult and time consuming and at least until recently required extensive field work (Liu et al. 2021; Rickli and Graf 2009).

Dai et al. (2002) stated that new methodologies are required to investigate landslide hazard and susceptibility efficiently. Several methods have been applied since, like heuristic, statistical or physically based models (Guzzetti et al. 2006; Korup and Stolle 2014). The rapid advance in computing technology during later years have included the development of fast algorithms and large storage space, allowing for Machine learning (ML) techniques in earth sciences (Korup and Stolle 2014). Numerous studies have investigated the effectiveness of various ML algorithms, and the results have been rather positive. ML-generated landslide susceptibility maps could therefore enhance susceptibility mapping and potentially serve as a useful tool for identifying landslide-prone areas (Kavzoglu et al. 2019; Liu et al. 2021; Merghadi et al. 2020).

A constraint of susceptibility maps is that they generally do not include dynamic inform-

ation related to the triggering and pre-conditioning factors of landslides (Nocentini et al. 2023). These factors, for instance rainfall and soil water saturation, are essential when determining the timing of landslides, since the immediate risk depends on how quickly water is supplied and to which extent the soil is saturated with water (Crozier 2010; J. Li et al. 2021; NGI 2014). Different attempts and methodologies have been proposed to incorporate dynamic factors and create spatio-temporal susceptibility maps, for instance with the implementation of rainfall thresholds (Huang et al. 2022; Ng et al. 2021). However, the use of ML techniques to obtain spatio-temporal landslide susceptibility maps is still largely in the preliminary phase (Ado et al. 2022; Merghadi et al. 2020; Nocentini et al. 2023; Tehrani et al. 2022).

Given the current upswing in the use of ML algorithms, alongside numerous studies demonstrating their effectiveness and a strong interest in their potential applications, this study aims to explore the feasibility of the algorithms for the MORLE triggered by *Hans*, both spatially and spatio-temporally. Also, a further analysis of different forests and forest parameters was conducted to gain supplemental insights regarding landslides initiating in forested areas and to assess whether some factors are more significant than others.

1.2 Research questions

Considering the topics discussed, this study seeks to address three research questions:

- Is it possible to identify whether certain forests or forest parameters are common for landslide triggering?
- Can machine learning models create efficient, spatio-temporal landslide susceptibility maps?
- Can machine learning models be utilized for other areas or storm events in Norway to predict landslides?

1.3 Thesis structure

This thesis is structured into seven sections. The first section is the Introduction. In section 2 we delve into the theory. Landslide classifications, conditioning and triggering factors of landslides in general and susceptibility and hazard maps are explained. Two different ML algorithms are examined and explained, both how the algorithms work and how to analyze the performance. Additionally, typical Norwegian forests and root cohesion is explained. The study area is presented in Section 3 and shows the landslide distribution in Ottadalen, Norway after the storm *Hans* based on a gathered inventory. Geology and climate of the study area is analyzed and described. In Section 4 the different parameters and corresponding data collection is presented. Furthermore, the method and handling of data is explained before the results are presented in Section 5. A discussion of the results is provided in Section 6 and a conclusion is given in Section 7.

The literature review in section 2 and data description and collection in section 4 was partly done in the TGB4575, "Engineering geology, Specialization project" in 2023. It has been modified and new information relevant for the thesis has been added. Wherever necessary, it is stated that large or parts of the text is taken from Hågensen (2023).

2 State of the art

2.1 Landslide classifications

The following subsection is largely taken from Hågensen (2023).

A landslide is generally a mass of soil or rock that moves downslope due to the action of gravity (Cruden and Varnes 1996; Gariano and Guzzetti 2016). The word landslide however, is a widely used term to describe slope movement that does not necessarily have true sliding (Varnes 1978). The range of processes regarding landslides makes it impossible to have a common term for all. Because of this, several different classifications exists. The Norwegian Water Resources and Energy Directorate (NVE) created a natural hazards classification based on collection of data and development of existing classifications in cooperation with the Norwegian railway authority and the Norwegian Public Roads Administration (Kristensen et al. 2015). The Varnes classification system, illustrated in Figure 1, categorizes landslides based on various movements such as falling, toppling, sliding, spreading, and flowing. Furthermore, these landslides involve different materials, including rock, debris, or earth (Varnes 1978).

Landslides are a complex phenomena (Hungr et al. 2013). It is important to be able to classify the different landslide types in order to reconstruct future landslides and understand their distribution (Crozier 2010). Inconsistencies across the definitions would lead to confusion and contradictions (Y. Li and Mo 2019). Hungr et al. (2013) modified the Varnes classification from 1978, defining 32 different landslides. In this report the classification is based on Hungr et al. (2013) and Varnes (1978).

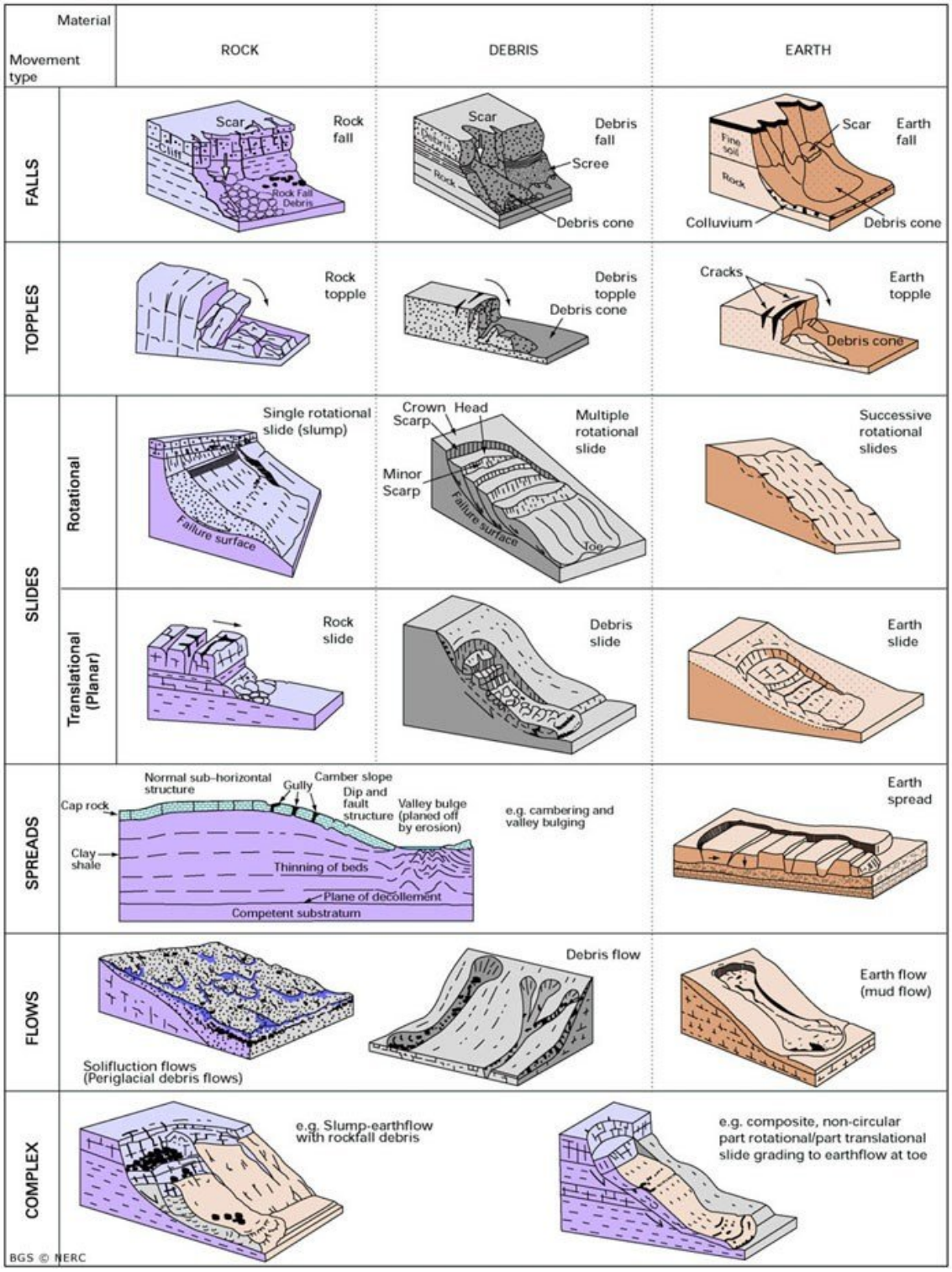

Figure 1: The Varnes classification system distinguishes type of landslides based on the material (rock, debris or earth) and the type of movement. The illustration is based on Varnes (1978) and Cruden and Varnes (1996).

In this study we will focus on landslides triggered in soil in steep terrain and the landslides consisting of debris and earth in a flowing or sliding motion. Shallow landslides can generally be classified as debris flows, debris slides and debris avalanches and are distinguished from debris floods (Ruther et al. 2022). Herein is a more detailed explanation of the characteristics of each of these events.

2.1.1 Shallow landslides

The following sub-sub-section is largely taken from Hågensen (2023).

Shallow landslides are characterized by a fracture depth ranging from a few decimeters to a couple of meters. The sliding plane is located within the soil cover or in contact with the bedrock (Crosta and Frattini 2003; Melchiorre and Frattini 2012). They have a small source area and can be characterized as point release (Ruther et al. 2022). The slipped material evolves into a debris flow propagating and entraining material as it moves downwards (Crosta and Frattini 2003). Material like sand, till and gravel usually generate shallow landslides (Emdal 2022).

2.1.2 Debris flow

The following sub-sub-section is largely taken from Hågensen (2023).

Debris flows are landslides that move downslope with a flow-like movement due to the water content (Figure 1)(NGI 2014). They are a rapid, saturated debris in a steep channel where most of the material in the flow comes from the entrainment of material along the way (Hungr et al. 2013). Debris flows typically follow the natural drainage paths of water but can also deviate into areas not typically traversed by water (Hungr et al. 2013; NVE 2022). Typically, debris flows initiate on slopes with angles larger than 25°, but under extreme precipitation events, they can occur on slopes with angles as low as 10° (NGI 2014).

2.1.3 Debris slide

The following sub-sub-section is largely taken from Hågensen (2023).

Debris slide is defined as a sliding of granular mass on a shallow, planar surface parallel to the ground (Hungr et al. 2013). These slides are between 0.5-2 meters thick and initiate in slope angles between 30-60° primarily (Hungr et al. 2013). Many debris slides become flow-like after a short distance and transform into debris avalanches or debris flow (Hungr et al. 2013). The debris slides can either be rotational or translational (planar) (Figure 1).

2.1.4 Debris avalanche

The following sub-sub-section is largely taken from Hågensen (2023).

Debris avalanches are shallow slides and can be found anywhere on a steep slope. They initiate as debris slides and move at extremely high velocities (more than 70km/h) (Hungr et al. 2013). A debris avalanche move open-slope while a debris flow moves in a more channeled matter (Ruther et al. 2022). Debris avalanches can be triggered due to a rock fall because of the quickly undrained loading process. Once initiated, this continues progressively and can entrain many thousands squared meters of material (Hungr et al. 2013).

2.1.5 Debris flood

The following sub-sub-section is largely taken from Hågensen (2023).

Debris flood moves with a flow like movement and has a very rapid flow of water (Hungr et al. 2013). The maximum discharge of water flow is comparable to a water flood (Hungr et al. 2013). The main difference between a debris flood and debris flow is the amount of water. Generally, debris floods are more diluted while debris flows have a larger amount of debris (Ilinca 2021). The velocities of debris floods are typically lower than those of debris flows, resulting in lower impact forces and reduced potential for damage to structures. However, debris floods can occur in large watersheds, often called “flash floods”. They extend further down slope compared to debris flows (Hungr et al. 2013).

2.2 Landslide causes and triggers

The following sub-section is largely taken from Hågensen (2023).

The conditioning factor for a landslide is the processes that happen over time, setting the slope up to fail (Bogaard and Greco 2016). This goes back to the beginning of formation of rock itself and the creation of the landscapes that exists today (Schuster and Wieczorek 2018). Conditioning factors include crustal movement, erosion, weathering, geology, soil, geomorphology (slope, elevation, aspect etc.) vegetation, previous landslides and human activity (roads, changed drainage etc.) (Kavzoglu et al. 2015; Schuster and Wieczorek 2018). Also volcanic eruptions that produce pyroclastic flows can mobilize landslides on the volcano's slopes (Jaedicke et al. 2014; Wieczorek and Glade 2005). The diverse range of conditioning factors complicates the determination of the most significant contributors to a specific landslide problem (Kavzoglu et al. 2015).

A trigger is what finally makes a slope unstable (Bogaard and Greco 2016). It is an external stimulus that causes an immediate or near immediate reaction from the slope (Schuster and Wieczorek 2018). Triggering factors can be heavy precipitation events, earthquakes, erosion processes and external influence of rock fall or rock slides (Gariano and Guzzetti 2016; NGI 2014; Wieczorek and Glade 2005). Human activities like excavation and construction can alter the natural landscape and the stability of slopes, making them more susceptible to landslides. Deforestation can reduce the stability of slopes by increasing surface runoff and soil erosion (Gariano and Guzzetti 2016; Highland and Bobrowsky 2008).

Extraordinary precipitation events are one of the most common triggering factor of landslides (Bogaard and Greco 2016; Gariano and Guzzetti 2016; Ma et al. 2021; Sandersen et al. 1997; Wieczorek and Glade 2005). The rapid infiltration of water is causing the soil to be saturated, increasing pore pressure and decreasing the effective stress (Abanco et al. 2021; Iverson 2000; Medina et al. 2021; Nocentini et al. 2023; Terzaghi et al. 1996). Heavy precipitation/snowmelt or large water discharge/erosion are the usual trigger mechanisms for debris flows, slides, and floods (Hungr et al. 2013; NVE 2022).

2.3 Landslide susceptibility, hazard assessment and risk zoning

The following sub-section is largely taken from Hågensen (2023).

Authorities need to depict areas that may be affected by future landslides. Considerations with respect to development plans and appropriate risk mitigation measures can then be implemented (Fell et al. 2008). Landslide inventories, susceptibility maps, hazard maps and risk maps serve as useful tools for providing information about these areas. Improved susceptibility maps can reduce the impact of landslides on infrastructure and human population (Goetz, Guthrie et al. 2011).

2.3.1 Scales

The following sub-sub-section is largely taken from Hågensen (2023).

The first step in landslide susceptibility, hazard and risk zoning is determining the scale of the analysis. Different scales can for instance be global, continental or regional (Reichenbach et al. 2018). In an even smaller study area, physically-based models can be employed. They involve numerical simulations and equations that describe the physics of landslides. A comprehensive analysis can be conducted to try and accurately determine the most critical soil properties (Medina et al. 2021). This requires information on the geotechnical parameters. Collecting this information over large areas can be challenging due to the spatial variability of the parameters (Tofani et al. 2017). The expense can be big and the computational capacity could also be demanding (Medina et al. 2021). They are therefore suited to study specific events and applied to single slopes (Micheletti et al. 2014).

If the scale is over larger regions, empirical models should be used. These models are based on observed data from historical landslide and statistical relationships between landslide occurrence and various influencing factors (Goetz, Guthrie et al. 2011; D. Guo et al. 2014). Empirical models do not consider the underlying physical processes. They are relatively simple and easy to implement and therefore often used for broad-scale landslide susceptibility mapping, hazard assessment, and early warning systems (Goetz, Guthrie et al. 2011).

2.3.2 Inventory

The following sub-sub-section is largely taken from Hågensen (2023).

A landslide inventory is a systematic and comprehensive database that documents information about landslides that have occurred in a particular area or region (Wubalem 2021). It typically includes detailed information about each landslide event such as a classification of landslide, location, date, extent, travel distance, validation, uncertainties and limitations (Fell et al. 2008). A landslide inventory is necessary to evaluate the conditioning and triggering factors of a landslide (Abanco et al. 2021). The inventory can be created using several methods, including satellite data, field work or evaluation of archived data coupled with Geographic Information System (GIS) tools (Wubalem 2021).

2.3.3 Susceptibility maps

The following sub-sub-section is partly taken from Hågensen (2023), but with additional information.

Landslide mapping can be divided into three consecutive levels such as susceptibility, hazard and risk (Vakhshoori et al. 2019). Landslide susceptibility refers to the probability of an area to experience landslides based on local terrain conditions (Fell et al. 2008; Ma et al. 2021; NVE 2023b; Reichenbach et al. 2018). It is basically trying to estimate "where" landslides are likely to happen based on the landslide inventory (Ma et al. 2021; Reichenbach et al. 2018). Conditions that led to landslides in the past facilitates the assessment of potential future landslides (Canoglu et al. 2019; Fell et al. 2008; Guzzetti et al. 2006; J. Li et al. 2021; Vakhshoori et al. 2019). Susceptibility mapping can be done through either quantitative or qualitative methods (Vakhshoori et al. 2019). Qualitatively methods are based on experts opinion and are subjective (Vakhshoori et al. 2019; Wang, Wen et al. 2021). Quantitative methods are based on using statistical and/or mathematical modelling techniques (Vakhshoori et al. 2019; Wang, Wen et al. 2021). This can for instance be ML methods (Ma et al. 2021).

Previous research on landslide susceptibility mapping has primarily focused on static factors, as the specific time and date of landslides are often unknown (Ng et al. 2021;

Nocentini et al. 2023). A map based on static factors indicates a spatial susceptibility map. Spatial susceptibility maps only highlight where landslides are likely to occur in the future, without specifying when (Nocentini et al. 2023). By adding dynamic factors, the susceptibility maps rather becomes spatio-temporal. The attempt to obtain spatio-temporal landslide susceptibility maps by applying ML models is however still in the preliminary phase (Nocentini et al. 2023).

2.3.4 Hazard and risk maps

The following sub-sub-section is largely taken from Hågensen (2023).

Landslide hazard zoning is utilizing the landslide susceptibility zoning and attempting to quantify the level of hazard by considering the frequency of the possible landslide (Fell et al. 2008; NVE 2023b). It includes categorizing areas into different hazard levels. This is valuable information regarding land-use planning and safety measures.

The risk is often estimated by taking the product of the probability of a landslide times the consequence. Consequence would involve potential damage to persons, property and environmental features (Fell et al. 2008; NVE 2023b).

2.4 Machine learning

Machine learning (ML) is a subfield of artificial intelligence, which is broadly defined as the capability of a machine to imitate human behaviour (Brown 2021). The functionality of ML is broad and used in several different fields like image analysis, self driving cars and personalized recommendations for new shows and songs on platforms like Netflix and Spotify (Brown 2021). The availability of online data and low-cost computation has improved the development of new learning algorithms and furthermore the progress in ML (Jordan and Mitchell 2015).

ML methods were introduced to the field of landslides in the early to mid 2000s (Merghadi et al. 2020). Since then, ML methods have rapidly evolved the scope, applications, precision and accuracy of susceptibility models (Merghadi et al. 2020). Predicting landslides

is a binary classification problem, where the two outcomes are either landslide or no-landslide (Navlani 2019). The ML algorithms try to assess whether a correlation exists between the observed landslides and various parameters related to conditioning and triggering factors (Ma et al. 2021). A variety of ML algorithms are available, offering a wide range of approaches (Ado et al. 2022; Merghadi et al. 2020).

In this thesis, the Random Forest (RF) and Logistic Regression (LR) models have been tested for landslide prediction in Ottadalen, Norway after the storm *Hans* in 2023. Both models are supervised learning models, so-called "soft-coded". That means the machine learns from the input provided by the user and produces an output that is most likely to occur (El Naqa and Murphy 2015; Jordan and Mitchell 2015; Ma et al. 2021; Tavasoli 2024). The algorithms adapt or change their architecture through repetition and experience so they become better at achieving the desired task.

2.4.1 Random Forest algorithm (RF)

The RF algorithm is a suitable ensemble model to predict the spatial distribution of landslides over a large area (Achu et al. 2023; W. Chen, Xie et al. 2017; Goetz, Brenning et al. 2015; Kavzoglu et al. 2019; Liu et al. 2021; Ma et al. 2021; Merghadi et al. 2020; Wang, Wen et al. 2021). The algorithm was proposed by Breiman (2001) and is composed of multiple decision trees, hence the term "forest" (Liu et al. 2021). A decision tree is like a flowchart where an internal node represents a parameter, the branch represents a decision and each leaf node represents the outcome of either landslide or non-landslide (Navlani 2023). The algorithm uses bootstrapping, which means that it generates random datasets based on the original dataset for each decision tree. This is done to prevent the trees from using the same data (Smolic 2023). Based on the outcome of the decision trees the algorithm does an aggregation. Aggregation means, in the case of a binary classification system, that it combines the results from the different decision trees and makes a final prediction, hence the term "ensemble" (Liu et al. 2021; Merghadi et al. 2020; Smolic 2023). Shafi (2023) illustrates the idea of the RF algorithm this way: "*Imagine you have a complex problem to solve, and you gather a group of experts from different fields to provide their input. Each expert provides their opinion based on their expertise and experience. Then, the experts would vote to arrive at a final decision.*" An illustration of how the

algorithm works is shown in Figure 2.

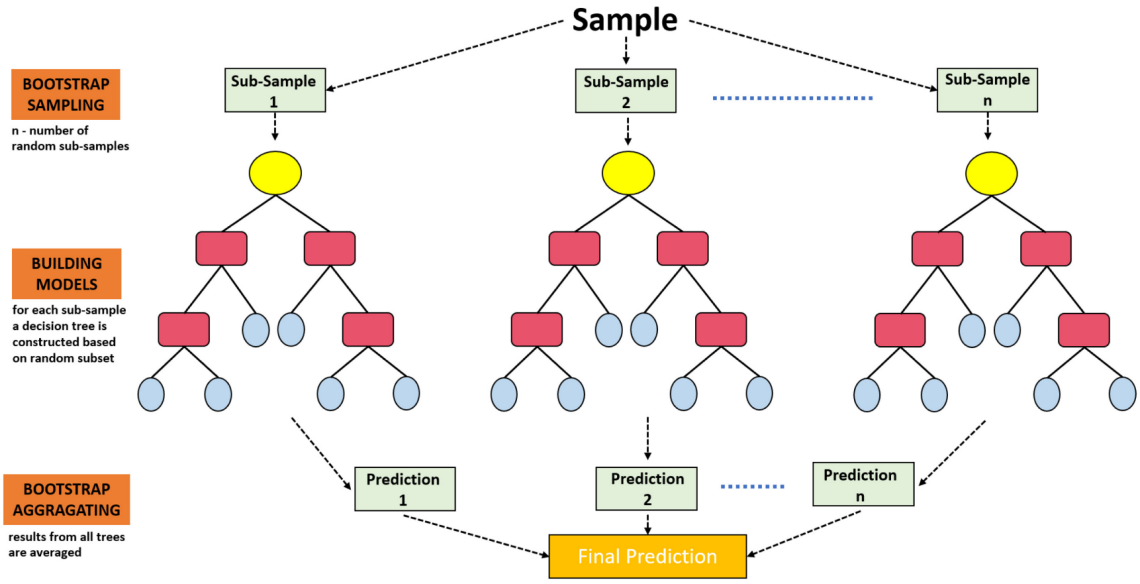

Figure 2: Illustration of the Random Forest algorithm. The figure is taken from Merghadi et al. (2020).

2.4.2 Logistic Regression algorithm (LR)

The LR algorithm is one of the ten most popular ML algorithms, initially applied from statistics and is one of the earliest ML methods (Ma et al. 2021; Merghadi et al. 2020; Ng et al. 2021). It has a straightforward algorithmic architecture, making the underlying concept easy to understand (Navlani 2019). The LR algorithm describes the relationship between a dependent variable (the presence or absence of landslides) and independent variables (conditioning and triggering factors) through a linear fitting model (Kavzoglu et al. 2019). The linear fitting function for the LR algorithm is expressed in Equation 1.

$$z = \beta_0 + \beta_1 x_1 + \beta_2 x_2 + ... + \beta_i x_i + e \tag{1}$$

z is the output, x_i is the i-th parameter, β indicates the learned parameter weights and e is the error (Budimir et al. 2015; Khaliq et al. 2023; Merghadi et al. 2020; Molnar 2020). The LR algorithm then adds a Sigmoid function to the linear combination of inputs which converts the output to a probability between 0 and 1 (Merghadi et al. 2020; Molnar 2020). The Sigmoid function is shown in Equation 2 and illustrated in Figure 3. The z from

Equation 1 is used in Equation 2. In this study the result outputs the probability of a landslide.

$$P = \frac{1}{1+e^{-z}} = \frac{e^{z}}{e^{z}+1} \tag{2}$$

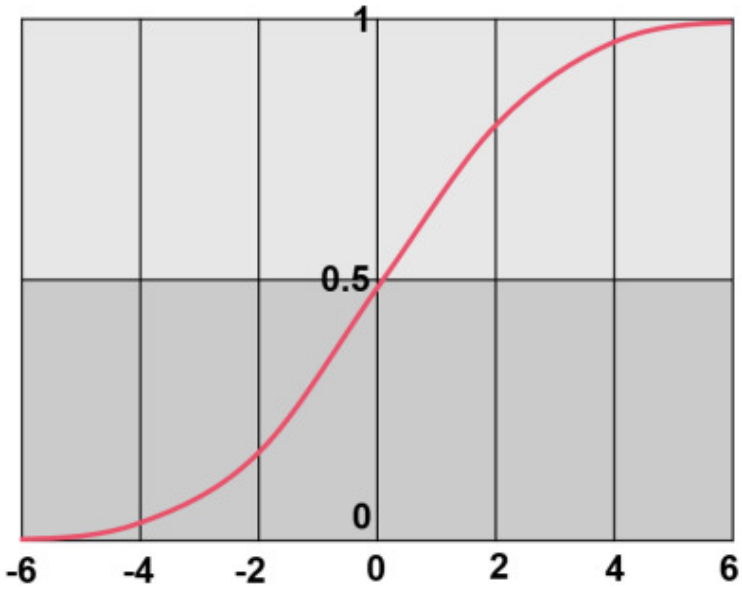

Figure 3: Illustration of the Sigmoid function applied to the linear fitting function for the Logistic Regression algorithm. The figure is taken from Merghadi et al. (2020).

2.4.3 Machine learning challenges

There are several factors to consider while utilizing ML algorithms, for example: (i) Imbalance in the dataset, (ii) bias, (iii) underfitting and overfitting, and (iv) multicollinearity. Imbalance in the dataset means that the no-events (no landslides) significantly outnumber the events (landslides). The no-events represent the majority of the dataset, while events represent the minority. Such imbalance can cause an algorithm to be biased (Ma et al. 2021). A biased algorithm consistently makes incorrect predictions due to its inability to represent the relationship between input and output (Barcelos 2022; GeeksforGeeks 2024b).

One way to handle imbalance is to undersample the no-events. Undersampling can be done in several different ways, where the simplest method is randomly selecting a certain

amount of the data (Brownlee 2021b). A major drawback of this method is the possible removal of important data (Brownlee 2021b; Merghadi et al. 2020). Another way to deal with imbalanced datasets is by utilizing the data augmentation Synthetic Minority Oversampling Technique (SMOTE) (Brownlee 2021a). The SMOTE technique propose an oversampling approach of the minority class (Chawla et al. 2002). This is achieved by selecting an instance from the minority class. Then it locates its k nearest neighbor, establishes a connection, and generates an artificial point within the expanse of the feature space between the two points (Ge et al. 2024). According to Chawla et al. (2002), a combination of undersampling and SMOTE provides better classifier performance to imbalanced datasets.

Algorithms can also experience underfitting or overfitting. Underfitting happens when the algorithm is too simple to capture the data complexities (GeeksforGeeks 2024b). It results in models giving poor accuracy from both training and test data (Amazon n.d.[b]; GeeksforGeeks 2024b). Overfitting occurs if a model is too complex and the algorithm learns noise and irrelevant details from training data and applies it when making predictions on unrevealed data (Amazon n.d.[b]; GeeksforGeeks 2024b). Indication of overfitting is when the model performs well on training data but poor on new, unseen data (Amazon n.d.[b]). If the performance on the training data matches that on the test data, overfitting is not an issue.

Multicollinearity indicates a linear relationship among the parameters, making it difficult to decide the individual contribution. This especially disturbs the weights in a LR algorithm (Molnar 2020). Variance Inflation Factors (VIF) is used to detect and quantify multicollinearity (Merghadi et al. 2020). VIF measures how much the variance of an algorithm increases when adding more variables, showing how much they are related (Merghadi et al. 2020). VIF can be described by Equation 3.

$$VIF = \frac{1}{1 - R^2} \tag{3}$$

The VIF procedure involves fitting a linear regression model to one of the independent inputs (for example the slope angle). The R^2 of the linear regression model evaluates how well the data predicts the values of the slope angle (O'brien 2007). Generally, if

VIF is equal to 1 the variables are not correlated. If VIF is between 1 and 5 the variables are moderately correlated and if VIF is greater than 5 the multicollinearity can be a problem (O'brien 2007; Zhou et al. 2018). This does not hold true for every parameter or algorithm, but it serves as a guideline to understand how various VIF values can be interpreted (O'brien 2007).

2.4.4 Model performance assessment

There are various performance metrics that can be employed to evaluate the effectiveness of the model (Bajaj 2023). One example is the confusion matrix. The confusion matrix divides the model prediction into either positive or negative classes depending on whether they indicate a landslide or not (Liu et al. 2021). The confusion matrix is shown in Table 1. It consists of four possible outcomes in the binary classification. True negative (TN) indicates that the model correctly predicts a no-landslide. False negative (FN) would mean an actual landslide was predicted to be a no-landslide. False positive (FP) indicates that a no-landslide is incorrectly marked as a landslide. True Positive (TP) indicate correctly predicting a landslide (Chawla et al. 2002; Liu et al. 2021). The TN and TP has a green color in Table 1. They are both positive outcomes indicating correct prediction of the model.

Table 1: Confusion matrix representing True negative (TN), False negative (FN), False positive (FP) and True positive (TP). The green cells indicate a correct classification, while the white cells indicates an incorrect classification.

	Predicted Negative "0"	Predicted Positive "1"
Actual Negative "0"	TN	FP
Actual Positive "1"	FN	TP

Based on the confusion matrix, several performance indicators can be determined. Table 2 indicates the different performance indicators.

Table 2: Performance indicators used to evaluate the performance of the models. The performance indicators are based on the confusion matrix. The table is inspired by Chawla et al. (2002) and Liu et al. (2021).

Formula	Range	Optimal Value
Accuracy = $\frac{TN+TP}{TN+TP+FN+FP}$	[0,1]	1
Precision = $\frac{TP}{TP+FP}$	[0,1]	1
Efficiency Index = $\frac{TP}{FP+TP+FN}$	[0,1]	1
True Positive Rate = $\frac{TP}{TP+FN}$	[0,1]	1
False Positive Rate = $\frac{FP}{FP+TN}$	[0,1]	0

Accuracy is the most used indicator to analyze the confusion matrix (Liu et al. 2021). It considers all cells of the confusion matrix and the optimal value of 1 would indicate a perfect prediction. A value of 0 indicates that the model did not predict any TN or TP. The accuracy can be misleading in the concept of landslide classification, as it is heavily influenced by the most common category which is the no-events (CAWCR 2015; Liu et al. 2021).

Precision is the proportion of positive results that were correctly classified. The indicator gives credit only for the correctly predicted landslide occurrences, not for all the no-landslide occurrences predicted correctly. It is therefore not affected by the potential imbalance of the dataset, emphasizing the correctness of positive predictions (Chawla et al. 2002). The optimal value of 1 indicates that the model correctly identified all events that actually happened. A value of 0 indicates that the model was not able to predict any landslides.

Efficiency Index (EI) takes a broader approach compared to *precision*, which describe the ratio of TP to the sum of TP and the unsuccessful predictions (Liu et al. 2021). Like *precision*, it does not get credit for the correctly predicted TN, which often overestimates the model prediction (CAWCR 2015; Liu et al. 2021). It evaluates the accuracy where the positive class is of specific interest, accounting for both FP and FN. The optimal value of 1 indicates the model correctly predicting all landslides. A value of 0 means the model is not able to predict any actual landslides.

The *True Positive Rate* (TPR) shows the ratio of an actual landslide being predicted as a landslide. A TPR value of 1 means a perfectly predicted landslide occurrence. A value of 0 means the model is not able to predict any actual landslides. The *False Positive Rate* (FPR) measures the ratio of events that was incorrectly identified. A FPR value of 1 means the model only predicts no-landslides as landslides, while a value of 0 means no falsely predicted landslides was made.

The TPR plotted against the FPR is used to generate the Reciever Operating Characteristic (ROC) curve. The ROC curve is illustrated in Figure 4. The ROC curve is an analytical method used to evaluate the performance of a binary classification method (Nahm 2022). It generates the curve by setting different thresholds of probability. The TPR and FPR are assigned a value based on a given threshold and the corresponding amount of TP, TN, FP and FN. A point can then be placed in the graph, and several points generate the curve. Point (1,1) (top right corner of the graph, Figure 4) indicates that all landslide points was correctly classified, but the model also incorrectly classified all no-landslide points as landslides. The point (0,1) shows a perfectly predictive model discriminating correctly between landslides and no-landslides. The yellow, diagonal line (Figure 4) indicates a random classifier, which means that the proportion of correctly predicting landslides is the same as incorrectly predicting landslides.

The Area Under the Curve (AUC) is the area under the ROC curve. The indicator makes it easy to compare ROC curves of different ML models. According to Ado et al. (2022), which studied 119 articles and provides a comprehensive overview of ML-based landslide susceptibility mapping, the AUC is considered the best evaluation method to assess the performance. An AUC of 1 represents perfect discrimination (Hoo et al. 2017).

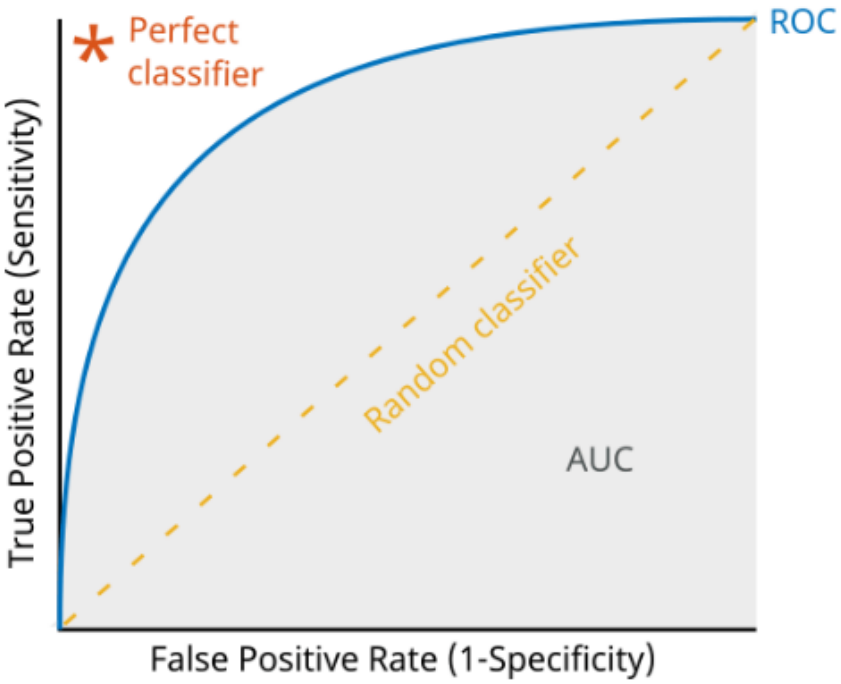

Figure 4: Illustration of the Reciever Operating Characteristic (ROC) curve. The Area Under the Curve (AUC) is the gray area, and the yellow dotted line indicates a random classifier. The ROC curve is generated based on the False Positive Rate (FPR) on the x-axis and the True Positive Rate (TPR) on the y-axis. The orange star in the top left corner indicates a perfect classifier. The figure is taken from MathWorks (n.d.).

The feature importance can be specified in the RF and LR models. This indicates which features (slope angle etc.) that are most relevant for the models predictive abilities (Shin 2023). In LR, the feature importance can be calculated through the coefficients after fitting the data (Filho 2023). Since the algorithm is operating on different units of the features, a standardization allows for comparison on equal terms. The coefficients (β's in Equation 1) and the corresponding feature importance are found through maximum likelihood estimation. This is a process that assigns a value to the features to maximize the likelihood that the process described by the algorithm was actually observed (Brooks-Bartlett 2018). The feature importance in RF is calculated as the mean and standard deviation of the accumulation of impurity decrease across all the trees in the forest (ScikitLearn n.d.[a]). Each time a feature is used to split a node, the impurity is calculated before and after the split, and the difference represents the decrease in impurity. Impurity measures how mixed the data is within a node. If a node contains data points from only one class, it

is very pure (low impurity). If a node contains a mix of data points from different classes, it is less pure (high impurity) (GeeksforGeeks 2024a).

Hyper-parameter tuning is a technique that allows for optimization of the models (Feurer and Hutter 2019). The hyper-parameters are external to the algorithms and can for instance be the depth of trees in a RF algorithm (Amazon n.d.[a]; Merghadi et al. 2020). There are no set rules as to which hyper-parameters that works best (Amazon n.d.[a]). One need to experiment to find the most optimal hyper-parameters (Amazon n.d.[a]). Experimenting manually can be time consuming. Therefore, different approaches of hyper-parameter tuning algorithms exists. Bayesian optimization and grid search are examples of such tuning techniques (Amazon n.d.[a]; Feurer and Hutter 2019).

Cross-validation is a technique used in ML to evaluate the performance of a model on unseen data. It can be used to detect overfitting, and several cross-validation methods exists (GeeksforGeeks 2023). A k-fold cross-validation involves dividing the available data into multiple (k) folds, using one of them as a validation set and the remaining (k-1) as a training set (Amazon 2024). This process is repeated k times, each time using a different fold as the validation set. Finally, the results from each validation step are averaged to produce the overall estimate of the models performance (GeeksforGeeks 2023). This is done to ensure that the actual discriminating abilities works on unseen data. It also detects overfitting and reduces bias as more of the data is being used (GeeksforGeeks 2023; Gupta 2017).

2.5 Forest parameters

It is well known that forests and plants contribute positively to stabilization of slopes (Cohen and Schwarz 2017; Z. Guo et al. 2023; Saito et al. 2017; Wu et al. 1979; Ziemer 1981b). Roots provide increasing shear resistance to the ground both hydrologically and mechanically (L. Zhang et al. 2021). Hydrologically, the roots contribute to less water in the soil due to evapotranspiration (Gariano and Guzzetti 2016; L. Zhang et al. 2021) and facilitates drainage by increasing permeability (Hwang et al. 2015; Shen et al. 2017). This leads to less pore water pressures. High pore water pressures are a known trigger for landslides (Gariano and Guzzetti 2016; Nocentini et al. 2023; Sidle et al. 2006).

Mechanically, roots enhance slope stability by providing lateral reinforcement (Ziemer 1981b). They anchor through the soil mass into bedrock fractures or more stable soil layers, and contribute interlocking binders within weaker soil masses (Ziemer 1981b). Also, the roots produce an apparent cohesion through root fiber reinforcement (Schmidt et al. 2001). This is reffered to as "root cohesion", which is the shear strength originating from the root system and improves stability of the slope (L. Zhang et al. 2021).

2.5.1 Norwegian forests

Norway has a large range of trees covering around 30 different types (NIBIO n.d.). Around 39% of Norway is covered by forests (Kildahl 2020). It is dominated by three tree types; pine & spruce (coniferous) and birch (deciduous). These together cover more than 90% of the forests in Norway (NIBIO n.d.).

There are roughly 1.5 billion pine trees in Norway (Dalen 2022). Pine trees (*Pinus sylvestris*) have deep-going, robust taproots that extends straight down into the ground (Sunding et al. 2024). This results in a highly storm-resistant tree species. They are however unable to develop taproots in areas with little loose material. Instead, they will spread outwards, making them more vulnerable to storms (Sunding et al. 2024). The tree height is usually between 20-30 meters, but can reach 40 meters. The lifetime of a pine tree can be as long as 600 years (Sunding et al. 2024).

There are approximately 3.2 billion spruce trees in Norway (Dalen 2022). Spruce forest (*Picea abies*) are conifers - cone bearing seed plants. Spruce is a part of the pine family, has a flat root system and can survive in quite shallow soil depths (Aarnes 2014; Christensen 2012). The tree height can reach 40-50 meters and they can live for 400 years (Aarnes 2014)

Deciduous trees has leaves compared to spruce and pine which has needles (Larsson 2024). Deciduous trees is a term that encompasses several different trees. In Norway, birch is the most common type of deciduous tree (Grindeland and Larsen 2024), reaching a total of probably around 4.9 billion trees in all of Norway (Dalen 2022). Birch has a shallow and wide root system (Planteportalen n.d.). The tree height is usually between 3 and 15 meters and they have a lifetime of around 300 years (Grindeland 2023).

2.5.2 Root cohesion

Root cohesion enhances the mechanical stabilization of a soil slope via root fiber reinforcement, providing increased resistance against shallow landslides (Schmidt et al. 2001; L. Zhang et al. 2021). Root reinforcement, the increase of tensile strength in soils due to the root network (Masi, Segoni et al. 2021), is difficult to measure (Schmidt et al. 2001). The magnitude of root cohesion depends on several factors like vegetation type, age, root architecture and root tensile strength (Schmidt et al. 2001; L. Zhang et al. 2021). Therefore, root cohesion values are typically back-calculated because direct field measurements are time-consuming and challenging to conduct over large areas (Schmidt et al. 2001). It can therefore be described as a function of the number and distribution of roots within a soil column and their elastic properties (Hwang et al. 2015). Hwang et al. (2015) proposes a way to calculate the root cohesion through Equation 4.

$$C_r = K \cdot T_r \cdot \frac{B_r}{\rho_r} \tag{4}$$

C_r [kPa] is the root cohesion of the specific tree root, K is a constant equal to 1.2 [m^{-1}], T_r [MPa] is the tensile strength of the specific root, B_r [$\frac{tonnes}{hectare}$] is the total below ground biomass and ρ_r [$\frac{kg}{m^3}$] is the density of the root. This method provides a very simple and computationally efficient estimation of the spatial pattern of root cohesion (Hwang et al. 2015).

2.5.3 Tensile strength

In order to use Equation 4, the tensile strength is needed. Wide variations in root tensile strength have been reported in the literature and appear to depend on species and site factors such as the local environment, season, root diameter, and orientation (Genet, Stokes, Salin et al. 2005; Ziemer 1981a). The seasons affect tensile strength, with roots being stronger in winter than in summer due to the decrease in water content. Also, the tensile strength usually decrease with increasing root size (Genet, Stokes, Salin et al. 2005; Hales 2018; Mao et al. 2012; Mattia et al. 2005). From literature, the tensile strength can be based on Equation 5.

$$T_{rn} = \alpha \cdot d_n^{\beta} \tag{5}$$

α and β are empirical constants depending on different tree species and d is the diameter of the tree root, while n assigns the specific tree species.

2.5.4 Underground biomass

Underground biomass is the organic material below ground (Ravindranath and Ostwald 2008). The biomass produced by trees and plants drives productivity in forest ecosystems (Smith 2020). Older forests for instance, have more underground biomass than younger forests (Hwang et al. 2015). Defining the underground biomass is however difficult and is therefore often sampled and scaled-up to component estimates (Smith 2020). Information on underground biomass is provided by the Norwegian Institute of Bioeconomy Research (NIBIO) and can be extracted from the forest resource map (SR16R). This is described more thoroughly in Section 4.

3 Study area

Section 3 is partly taken from Hågensen (2023).

The work presented herein focuses in the Ottadalen area, an east-west trending valley situated in the heart of southern Norway (Figure 5). It is surrounded by the mountainous expanses of Jotunheimen, Rondane, and Dovrefjell. These mountain massifs all have peaks surpassing 2000 meters above sea level. Positioned at approximately 360 meters above sea level, Vågåvatnet (lake) at the bottom of Ottadalen is centrally located in the study area (Kartverket 2023b). Consequently, the area exhibits considerable altitude relief. The study area (red square) is approximately 3071.1 km^2.

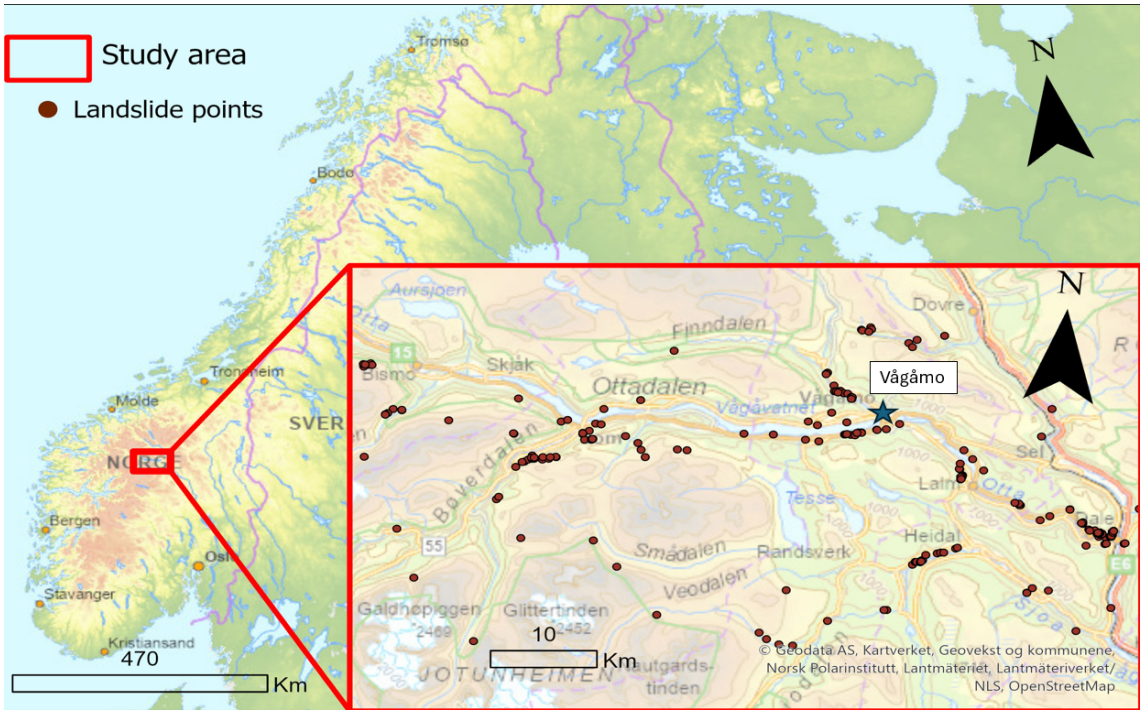

Figure 5: Map of the study area. The study area is in Ottadalen, indicated by the red square. The brown dots are release points of landslides. North arrow and scale bar is added to both maps. Vågåmo is marked with a blue star. The background map is the OpenStreetMap from ArcGIS Pro.

3.1 Geology

3.1.1 Bedrock geology

Large parts of central and mountainous Norway has bedrock geology originating from the formation of the Caledonian mountain range around 400 million years ago (Bryhni and Fossen 2023). The process of mountain range formation, known as orogeny, consists of large-scale movements, folding, magmatic activity, and overthrusting (Fossen 2023b). Overthrust sheets are large sheets of the earths crust being pushed by tectonic forces over the already existing lithosphere, making it both deeper and thicker (Fossen 2023a). It can be referred to four levels of overthrust sheets in Norway after the Caledonian orogeny; lower, middle, upper, and uppermost allochthon (Bryhni and Fossen 2023).

The bedrock geology in Ottadalen primarily consists of the lower, middle and upper allochthons, as well as Precambrian bedrock. These allochthons contribute to the study area's diverse geology, which includes igneous, sedimentary, and metamorphic rocks, along with numerous faults and shear zones (NGU 2023). Granitic gneiss, predominantly of Precambrian age, dominates the northwestern part of the study area (Hole and Bergersen 1981; NGU 2023). The rest of the study area is extensively influenced by the overthrust sheets, resulting in complex geology. Various rock types, including granite, quartzite, sandstone, conglomerate, phyllite, calcareous phyllite, greenschist, mica schist and different types of gneisses are found in the area (NGU 2023). Common for the rocks in the area, with some exceptions, is that they break down easily and that they form a fine-grained moraine soil (Kleiven 2022; Nystuen 2013).

3.1.2 Surficial deposits

Norway's landscape has been significantly shaped by multiple large ice sheets, intermittently covering the country over the past 2.6 million years (Vorren and Mangerud 2013). Most of the surficial deposits found in Norway today are geologically young, dating back to the last ice sheet known as the Weichselian glaciation, which ended approximately 10,000 years ago (Lundqvist 1986; NGI 2014). The relatively young deposits is because glaciers typically (though not always) remove existing deposits and materials in

their path (Lasberg 2014; Vorren and Mangerud 2013). Deglaciation leave behind unsorted sediments of various sizes, also known as till and glaciomarine deposits (Vorren and Mangerud 2013). Till is the most widespread type of sediment in Norway by far (Bergersen and Garnes 1972; NGU n.d.).

Ottadalen, a part of Gudbrandsdalen, is a classic U-shaped valley originating from glacial erosion (Mæhlum 2023; Thorsnæs 2023; Vorren and Mangerud 2013), where till of varying thickness is the primary surficial deposit (NGU n.d.; Romundset et al. 2023). Three different tills have been distinguished in the study area on the basis of textural and structural analyses and an investigation of the till stratigraphy was performed (Bergersen and Garnes 1972; Hole and Bergersen 1981). Of special interest is the finding that the basal part of the till is sandy-gravelly, somewhat sorted and more rounded. Higher up, the material is distinctly less sorted and richer in clay. The different tills have been exposed to different depositional conditions. The lowest part of the till is assumed to originate from the sub-till sediments which were deposited before the last glaciation. The finer materials in the top layer of the till can be correlated to the deglaciation period. During this period, several glacier dammed lakes existed, for instance *Store Dølasjø* which extended across Northern Gudbrandsdalen and Ottadalen towards the end of the Weichselian glaciation (Kleiven 2022; Romundset et al. 2023). A material richer in clay is more susceptible for landslides, as pore pressures can build up over time due to low permeability (NGI 2014).

Other surficial deposits are also found in the study area. Most of the valley floor is covered in alluvial deposits from the Ottariver and glaciolacustrine deposits from the glacier dammed lakes (Romundset et al. 2023). Glaciofluvial deposits is scattered around the study area due to interstadial deglaciation periods (Kleiven 2022; Romundset et al. 2023). Avalanche activity and weathered materials are also profound in the area (Kleiven 2022; NGU n.d.). A map showing the different deposits can be found in Figure 9.

3.2 Climate

Ottadalen has a relatively continental climate. Continental climates often have a significant annual variation in temperature compared to the coastal areas, which have more even annual temperatures (NationalGeographic 2023). On average, since 1991 the study area

has been colder than the coastal areas (SeNorge 2023). The mean annual temperature in Otta since 2018 is 4.2°C (Klimaservicesenter 2023).

Ottadalen is one of the locations in Norway with the least precipitation. SeNorge (2023) shows the average precipitation from 1991-2020. The study area has less than 500 mm annually. The average yearly precipitation since 2020 was 410 mm (Klimaservicesenter 2023). Compared to the average annual precipitation of 3000 to 4000 mm observed on the western coast of Norway, the study area experiences a relatively low average annual precipitation (SeNorge 2023). The low precipitations are due to the surrounding high mountains "protecting" the inner areas of Norway from the moist air (Dannevig and Harstveit 2022).

3.3 Description of the storm *Hans*

On Monday 7 August 2023, large parts of south-central Norway were hit by the storm *Hans*. *Hans* was a combination of low pressure systems from both the Atlantic Ocean and Mediterranean Sea that "joined forces" over central Europe and took a westerly turn as they merged over southern Sweden and the Baltic Sea (Granerød et al. 2023). As the low pressure system progressed northward, it accumulated a significant amount of moisture along its path (Andreassen 2023). The fact that the low pressures were coming towards Norway from the southeast meant no protection from the mountains on the west coast. In the flat, eastern landscapes, water lingers long, flows slowly, and accumulates. Heavy rainfall affects these areas on a larger scale compared to the west coast where the steep mountainsides quickly drains water. Figure 6 shows the progression of the low pressure during *Hans* between 7-9 August 2023.

Neither nature nor people were prepared for the rainfall intensity during *Hans*. As a result of the extreme precipitation event, large areas were flooded (Bugge and Borgmo 2023; Ekroll 2023). *Hans* initiated a MORLE and almost 2900 people had to be evacuated from their homes (Revheim-Rafaelsen et al. 2023). Landslides were hitting houses and damaging infrastructure. The material cost of *Hans* turned out to be 1.8 billion Norwegian Kroner (Torkelsen et al. 2023).

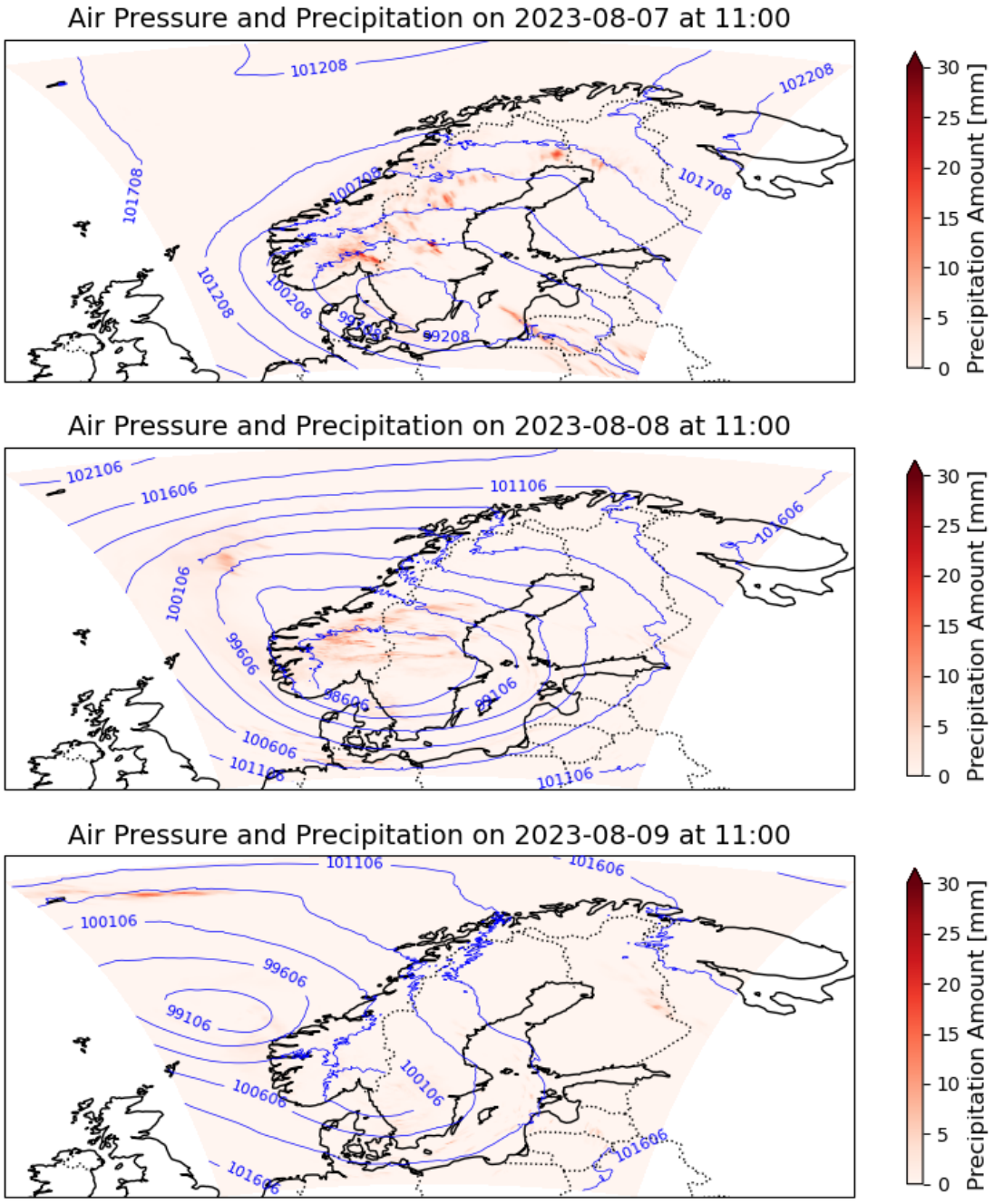

Figure 6: Map showing the meteorological situation of *Hans* over Norway at 11 a.m. for three consecutive days, 7-9 August 2023. The black lines are showing borders, the blue lines are showing the pressure contour lines in Pascal and the red areas are showing precipitation. The colorbar is indicating the amount of rain in mm. The map is based on data from METNorway (2023).

4 Data and Methods

4.1 Data

The parameters used for landslide investigation and in the ML models included the soil type, tree type, root cohesion, slope angle, slope aspect, flow accumulation, precipitation and soil saturation. To facilitate the examination of these parameters, data collection was necessary. Table 3 outlines the type of data, its resolution and the sources used to enable the analysis.

Table 3: Overview of the collected data used for both landslide investigation and ML methods. The resolution and source of the data is stated. The table is taken from Hågensen (2023).

Data	Resolution/Quality	Source
DTM	10 m^2	Høydedata
Quaternary map	1:50 000	NGU
Vegetation SR16	16 m^2	NIBIO
Precipitation/Soil saturation	1 km^2	MET Norway

4.1.1 Terrain data

The following sub-sub-section is partly taken from Hågensen (2023).

To measure slope angle, slope aspect and flow accumulation, a 10 m^2 resolution Digital Terrain Model (DTM) from Høydedata was used (Kartverket 2023b). The data is established as "point clouds" based on Light detection and ranging (LiDAR) from planes and aerial photos (Kartverket 2023a). LiDAR determines the distance from a sensor to a target by analyzing half of the time it takes for a laser pulse to be emitted and then reflected back (Baltensweiler et al. 2017; StatensKartverk 2018). Kartverket classifies precision into classes from A to D. A DTM of 10 m^2 can be fulfilled with class C, which indicates a minimum of two point per m^2 (StatensKartverk 2018).

Information about the surficial formations existing in the study area was obtained from the

Quaternary geology map of Norway (NGU n.d.). The map is produced by the Norwegian Geological Survey (NGU). The Quaternary geology map in this report has a resolution of 1:50 000. The data distributed from NGU are collected from detailed surveys in the field, based on a thorough prestudy of maps, topographic maps and air photos. The survey also includes reports, scientific publications and data from ground investigations (NGU n.d.). An important note is that the quaternary map is showing the soil only in the top meters of the terrain. Thick and thin layers of other types of soil can be found beneath this top layer, but are not necessarily shown (NGU n.d.).

The SR16 is a forest resource map from the Norwegian Institute of Bioeconomy Research (NIBIO) with a resolution of 16 m^2 (NIBIO 2023). The primary method of generating the dataset involves automated processing of remote sensing data, which includes techniques like photogrammetry and laser technology. Other methods of creation are terrain models, satellite data and existing data like AR5. The AR5 map shows land use and land cover (LULC) and is continuously updated based on administrative tasks fulfilled by the municipality (Tenge 2016). The SR16 map is divided into SR16R and SR16V which are raster map and vector map, respectively. The SR16R mostly consists of three band rasters representing the minimum, maximum and mean values. These numerical values naturally consists of uncertainties, and this is dealt with by using a 95% prediction interval. The SR16R includes information about several different forest parameters. Different forest parameters examined in this study are the amount of trees per hectare with varying tree diameter at breast height, the leaves coverage, tree height, tree diameter at breast height and the different forest types. Breast height is 1.3 meters above ground (Bækkelund 2024).

4.1.2 Landslide inventory data

The following sub-sub-section is partly taken from Hågensen (2023).

A systematic and comprehensive landslide inventory for the study area is a combination of three different databases and was gathered with diverse methods; (i) An inventory from field observations after *Hans* gathered by Norwegian Geotechnical Institute (NGI), (ii) a database provided by Denise Rüther from Western Norway University of Applied

Sciences (HVL) on landslide observations based on satellite imagery (Rüther et al. 2024), and (iii) landslides that were recorded in The Norwegian Water Resources and Energy Directorate's (NVE) database.

Field data was collected by NGI on foot utilizing mapping tools and drones. The drones were only used for photography. In national park areas where drones were prohibited and the landslides was hard to reach by foot, mapping was conducted using cameras and binoculars. The mapping had focus on parameters that can be used for landslide hazard modelling like extent, vegetation and soil properties. Additionally, the triggering cause of the landslides was investigated. In total, the inventory contained 53 landslides initiation points. 33 of these landslides were additionally mapped as polygons.

The satellite inventory provided by Denise Rüther from HVL was obtained primarily from remote sensing comparison of pre-event and post-event images of the area (Lindsay et al. 2022; Rüther et al. 2024). This approach is highly effective in terms of covering a lot of area but requires cloud free images before and after the event within a sensible time period (Abanco et al. 2021). Due to the difficulty of classifying landslides solely based on satellite images, multiple validation methods were used. This included either field work, field reconnaissance, orthophoto, national databases, newspaper articles, Copernicus emergency response or other high resolution satellite data (Rüther et al. 2024).

Data from NVE was extracted from their website (NVE 2023a). The website has several different maps. The map of "avalanche events" was used. It is a database containing more than 94,000 landslide observations all over Norway. The resolution "varies" according to NVE (2018) and Rüther et al. (2024). The map reaches a scale of 1:20 m. The registration of observations is open for anyone and the road and rail authorities are continuously updating their data to the website. Quality control of the observations is happening constantly and the observations are marked with three different quality levels (NVE 2018). In order to focus on the landslides that initiated during *Hans*, the dates was filtered to include observations that had been registered from 1 August until 16 October 2023. The decision to set it until 16 October was to ensure that landslides during *Hans* had been recorded in the database. The gathered landslide inventory from NVE was then merged with the inventory from NGI and HVL. The resulting landslide inventory was manually checked to remove duplicates. It was afterwards confirmed that the six NVE slides in this

report was between 8-10 August and inside the respective study area in Ottadalen. This means that *Hans* initiated the slides. Additionally, the locations of the slides was usually at the observation point down by the road instead of at the actual release area. The points was therefore manually placed in the most natural location based on the description of the landslide and the surrounding terrain.

Table 4: Summary of data points provided by contributors to the inventory within the study area.

Name	Number of landslides
NGI	53
NVE	6
HVL	171
Total	230

When implementing dynamic factors, it is important to know the initiation date of the landslides (Nocentini et al. 2023). The landslide inventory used in this study contained this information for 39 landslides. Since the most common triggering factor of landslides is precipitation, the date that provided most precipitation during *Hans* at the landslide locations would be considered the initiation date. This approach resulted in landslides on respective dates as shown in Table 5, with 175 landslides on August 8, 52 on August 9 and no landslides on August 7 and 10. The reason for 227 landslides instead of 230 is explained in the Methods section (4.2).

Table 5: Overview of amount of landslides on respective dates based on the assumptions mentioned and the landslide inventory provided.

Date	Landslides
August 7	0
August 8	175
August 9	52
August 10	0

4.1.3 Precipitation data

The following sub-sub-section is partly taken from Hågensen (2023).

In order to investigate the precipitation, data from MET Norway was used (METNorway 2023). The data include measurements since 1957 for large parts of Norway (Lussana 2023; SeNorge n.d.). The precipitation data are based on measurements with either instrumental or manual rain gauges (METNorway 2017). In order to interpolate the precipitation values for all of Norway, a statistical method is used with 1 km^2 grids (Lussana et al. 2019). Measurements have been adjusted with regards to wind-induced under-catch, that considers disruption of the measurements due to wind (Lussana 2023; Lussana et al. 2019). In addition to observations, the spatial interpolation utilize information provided by a climate model (Lussana et al. 2019).

The precipitation data used in this study represents the modeled values accumulated over 24 hours for August 7 to 10. This time frame was selected because the storm *Hans* impacted Norway from August 7 to August 9, delivering significant rainfall (Granerød et al. 2023). Also, MET Norway collects precipitation data from 06:00 "yesterday" to 06:00 "today". The precipitation data for August 7 is therefore measurements from 06:00 on August 6 to 06:00 on August 7 (Lussana 2023). Table 6 illustrates the modelled average precipitation and soil saturation degree across the entire study area during the different dates and times.

4.1.4 Soil saturation degree data

The following sub-sub-section is partly taken from Hågensen (2023).

The soil saturation degree is determined using a model that computes the quantity of water coming from rainfall and snowmelt. It is a time dependent parameter and combines the groundwater conditions and the conditions in the root zone (soil water) (SeNorge n.d.). Additionally, it considers how long the water remains in the soil before it drains as groundwater or evaporates (SeNorge n.d.). The soil saturation degree are shown as a percent-wise unit. The percentage describes the relationship between today's simulated water storage compared to maximum simulated water storage in the reference period 1981-2010 with

the use of the Gridded Water Balance (GWB) model. The GWB-model is a spatially distributed version of the Hydrologiska Byråns Vattenbalansavdelning-model (Beldring et al. 2003; Boje et al. 2018; SeNorge n.d.). The GWB-model is a 1 km^2 grid based version and considers how the topography and vegetation are distributed within each grid-cell (SeNorge n.d.). The values for soil saturation degree was in this study extracted every 24h. The values was gathered for the same dates as the precipitation data, between 7 to 10 August. The only difference is that the soil saturation degree value is generated at 08:00 every day instead of 06:00 (*Xgeo* n.d.). The soil saturation degree is showed with red text in Table 6 to distinguish it from the precipitation data.

Table 6: Average, modelled precipitation and soil saturation over the total study area for each day. The table illustrate the reference time for the different dates, and the averaged amount of precipitation and soil saturation for each day.

Date	Modelled Average Precipitation [mm/day]	Modelled Average Soil Saturation Degree [%]
August 7, 2023 (August 6, 06:00 - August 7, 06:00) (August 6, 08:00 - August 7, 08:00)	3.7	63.6
August 8, 2023 (August 7, 06:00 - August 8, 06:00) (August 7, 08:00 - August 8, 08:00)	63.9	87.3
August 9, 2023 (August 8, 06:00 - August 9, 06:00) (August 8, 08:00 - August 9, 08:00)	53.9	104.1
August 10, 2023 (August 9, 06:00 - August 10, 06:00) (August 9, 08:00 - August 10, 08:00)	18.2	101.8

4.2 Methods

All data regarding the different parameters was investigated with the use of Python and ArcGIS Pro. Python is an interpreted, high level programming language. It has a simple, easy to learn syntax and provides access to several open source libraries essential for data handling and implementation of ML models. It is free and one of the most popular programming languages in data science and ML (Python n.d.).

Geographic Information System (GIS) is a system that creates, manages, analyzes and maps all types of data and connects where things are with all type of descriptive information (Esri n.d.). ArcGIS Pro is a software from ESRI that allows for exploring, visualizing and analyzing spatial data. Through the application you can store maps, layouts, tables and work with them as needed (ArcGISPro n.d.[e],[f]). The combination of Python and ArcGIS Pro allows for a thorough analysis of the data.

4.2.1 Landslide frequency

The following sub-sub-section is partly taken from Hågensen (2023).

The landslide frequency is a value that helps assess "where" landslides are likely to occur. It provides a better understanding of the landslide risk associated with specific areas. It is a key parameter and provides valuable information for hazard assessment and land-use planning and helps evaluate the effects of specific site characteristics on slope stability (Reichenbach et al. 2018; Rickli and Graf 2009). In this study, the frequency is employed to identify and evaluate areas prone to landslides based on the investigated parameters. The frequency can be found with Equation 6.

$$\text{Frequency} = \frac{\left(\dfrac{\text{Number of landslides in class 1}}{\text{Total number of landslides}}\right)}{\left(\dfrac{\text{Area of class 1}}{\text{Total area}}\right)} \tag{6}$$

"Class 1" represents the number of landslides and the corresponding area for one of the parameters. The total area corresponds to the study area, facilitating the comparison of frequencies.

4.2.2 Computation of parameters with GIS tools

The following sub-sub-section is partly taken from Hågensen (2023).

Slope angle and slope aspect have been computed using the "Slope" and "Aspect" tool in ArcGIS Pro, applied to the DTM. The slope result shows the rate of change in elevation and is given in degrees ranging from 0-90° (ArcGISPro n.d.[h]). The aspect results identifies the compass direction the terrain face. It is measured clockwise in degrees from 0 (north) to 360 (again north) encompassing the whole circle (ArcGISPro n.d.[a]). See Table 7 for division of the different aspects.

Table 7: Slope aspect with corresponding degrees.

N	NE	E	SE
337.5-22.5	22.5-67.5	67.5-112.5	112.5-157.5
S	SW	W	NW
157.5-202.5	202.5-247.5	247.5-292.5	292.5-337.5

The flow accumulation is also computed from the DTM. The "Fill" tool had to be used in order to ensure proper delineation of basins and streams (ArcGISPro n.d.[b]). Afterwards, the "Flow Direction" tool was utilized. This tool generates eight possible directions for water flow in each pixel derived from elevation of the surrounding pixels (ArcGISPro n.d.[d]). The D8 method determines the direction based on the steepest descent. When a direction of steepest descent is found, the output cell is coded with the value representing that direction. The "Flow Accumulation" tool counts total accumulated flow as the sum of weights from all "Flow Direction" cells contributing to each cell positioned downslope. Cells with high flow accumulation values are areas of concentrated flow, while areas of zero flow accumulation are topographic highs (ArcGISPro n.d.[c]).

The "Resample" tool adjusts the spatial resolution of a raster dataset and establishes rules for aggregating the interpolated values across the new pixels (ArcGISPro n.d.[g]). Ensuring the same resolution, which provides a consistent number of pixels, is crucial when running a ML model. A bilinear resampling technique is the best way to deal with continuous data and was therefore utilized in this study (ArcGISPro n.d.[g]). The interpola-

tion exhibit smoother transitions and represent real life better. It is important to keep in mind that the bilinear resampling technique can change a pixel from zero to non-zero (ArcGISPro n.d.[g]). The forest data, soil data, precipitation data and soil saturation degree data were resampled to a 10m x 10m resolution to align with the resolution of the DTM.

4.2.3 Method to obtain root cohesion

To determine root cohesion, information on root tensile strength, underground biomass, root density and root diameter is required. The method, proposed by Capobianco et al. (2024), is employed in this study to derive values for root cohesion. The method applies Equation 4 which is shown below.

$$C_r = K \cdot T_r \cdot \frac{B_r}{\rho_r}$$

The method assumes that roots have a diameter of 3.5 mm. The root diameter is then used to further determine the tensile strength T_r. Table 8 lists the root density and tensile strength values for the different tree species suggested by Capobianco et al. (2024). It is important to keep in mind that the density of trees vary significantly both between and within regions (Fischer et al. 2016). Constant values of density were used for simplicity in this study. The underground biomass, B_r, can be collected from the forest resource map (SR16R) (NIBIO 2023). The root cohesion was then calculated for the different areas covered in either spruce, pine or deciduous forests.

Table 8: Values used to generate the root cohesion suggested by Capobianco et al. (2024) are shown. Reference to Norway Spruce: Bischetti et al. (2007). Reference to Pine: Genet, Stokes, Salin et al. (2005). Reference to Deciduous: Mao et al. (2012).

Species Norwegian Forests	Root Density [kg/m^3]	Reference species	Regression equation for T_r [MPa]	Reference forest
Norway Spruce *Picea Abies*	451	Norway Spruce Picea Abies	$T_r = 28.1d^{-0.72}$	Italian alps Italy
Pine *Pinus Sylvestris*	539	Austrian Pine	$T_r = 18.4d^{-0.52}$	Gironde France
Deciduous	671	Generic for several tree species	$T_r = 28.97d^{-0.52}$	French

4.2.4 Preparation of total dataset

Figure 7 is a flow chart showing the process of producing landslide susceptibility maps, from data collection to complete maps. The process is general for both static and dynamic approaches used in this study, and is mainly supposed to give an overview. Part 2 of the flow chart however is slightly different between the two approaches and is further described in each respective section. A general explanation is given first.

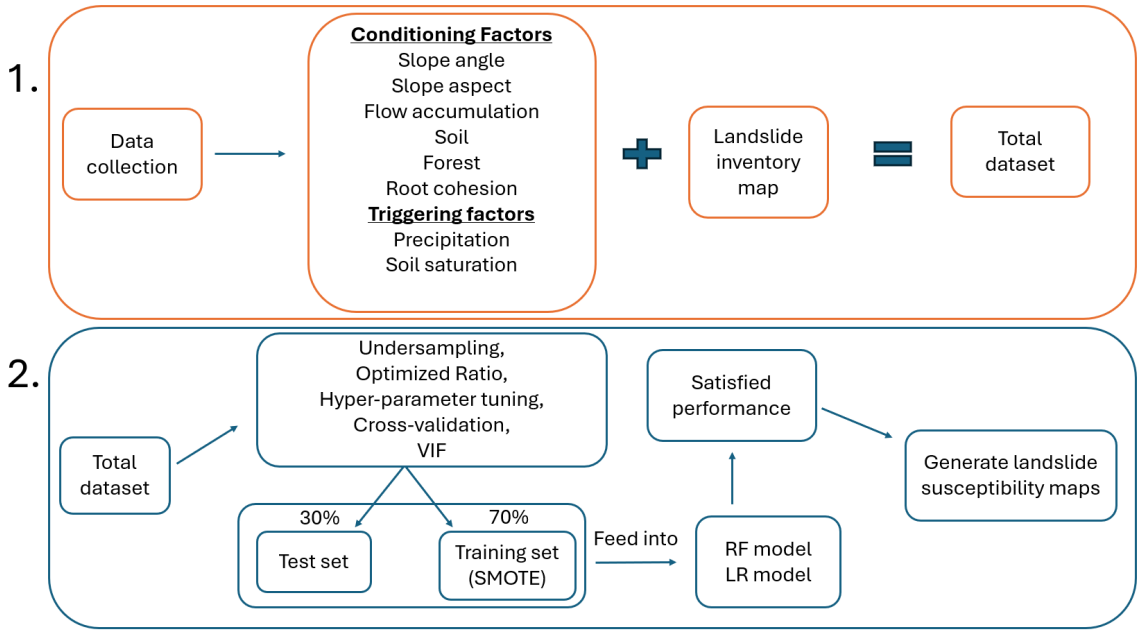

Figure 7: Flow chart showing the process from data collection in (1.) to generating landslide susceptibility maps in (2). The flow chart offers an overview, but especially (2.) should be linked to the method descriptions for both static and dynamic approaches to provide a complete understanding, as these approaches differ slightly.

Firstly looking at Part 1 of Figure 7. After acquiring the total dataset, the "Resample" tool segmented the respective parameters inside the study area into 10m x 10m pixels, totaling 30,711,300 pixels. Each pixel had eight values corresponding to the eight input parameters. Additionally, a ninth value was assigned based on the landslide inventory, indicating whether the pixel represented a landslide or not. Pixels where landslides occurred were given a value of "1", while no landslide pixels were assigned a value of "0". Consequently, the total dataset comprised 30,711,300 pixels, each with nine parameter values.

Only 227 pixels were classified as landslide pixels instead of the expected 230. This discrepancy occurred because three pairs of landslides were located within the same pixel. These pairs of landslides initiated in close proximity to each other and were therefore counted as one.

4.2.5 General preparation of training and test set

Now looking at Part 2 of the flow chart in Figure 7. The total dataset's imbalance needed to be addressed and the no-landslide pixels was therefore randomly undersampled. An optimized ratio $\frac{no-landslide}{landslide}$ had to be found for both static and dynamic approaches. As this was accomplished differently, it is further explained in the respective sections. The resulting dataset with the respective ratios was split into a training and test set with a 70/30 split, a common split used in ML methods (Ado et al. 2022; Liu et al. 2021; Yang et al. 2023; Zhou et al. 2018). Hyper-parameter tuning, VIF investigation and cross-validation was performed to obtain the best model configuration and to ensure no overfitting.

The training set is then presented to the models. During training, all information is provided – the model knows the input parameters and whether the pixel is a landslide pixel or not. Afterwards, the models are presented to the new, unseen data of the test set. During testing, the models are provided with input parameters for each pixel without any information regarding their landslide status. The task of the models is to predict which pixels represent landslides and which do not.

The confusion matrix, generated from the model's predictions on the test set, indicates the amount of TP, TN, FP and FN from testing. This sets the basis for the performance assessment. If the model performance is satisfactory, the models are introduced to the study area and predicts landslide probability for each pixel.

Scikit Learn provides the necessary Python (computer language) libraries for utilizing the RF and LR models. The libraries are relatively accessible to non-specialists, user-friendly and provides tutorials, examples and user guides. The libraries are easily downloaded, and Python was therefore used to run the models (ScikitLearn n.d.[b],[c]). Scripts used throughout this study (also from the Specialization Project) showing data collection, preparation of datasets, creation of plots and figures and running of the RF and LR models are shared (open source, and open science) on Github: (Repository Master thesis) or URL: https://github.com/isakhag/master_thesis.git

4.2.6 Method to assess static landslide susceptibility

For the static factor assessment, precipitation and soil saturation data was removed from the dataset. This allowed for further investigation of the parameters slope angle, slope aspect, tree type, root cohesion, flow accumulation and soil type.

To avoid the imbalance, the no-landslide pixels was randomly undersampled. SMOTE was attempted but did not provide better performance. To facilitate a consistent comparison between RF and LR, the same ratio was used. The optimal ratio varies with different ML models, areas and different split ratios (Yang et al. 2023). A ratio of 3:1 $\frac{no-landslide}{landslide}$ was used. This ratio provided a total of 908 pixels in the dataset, with 681 being random no-landslide pixels and 227 being landslide pixels.

The dataset was further divided into training and testing sets at a 70/30 split. The training set consisted of 635 pixels, comprising 159 landslide pixels and 476 no-landslide pixels. The test set contained 273 pixels, with 68 landslide pixels and 205 no-landslide pixels.

Figure 8 and 9 shows the distribution of the static parameters. The map bounds is the study area as indicated in Figure 5. The position of Vågåmo is marked with a star, landslides are marked as brown points and the different values of the input parameters are illustrated in the legend. The flow accumulation varied greatly between small and large accumulations. It was therefore difficult to illustrate it in a good way. The best attempt is shown in Figure 9, where the largest accumulations are shown as white lines on a purple background that illustrates low flow accumulation. Also, the soil legend in Figure 9 is quite small due to the large amount of different soils. The legend is the same as NGU standards, and can additionally be found in the Appendix (Figure 36 and 37) or on NGU's website (NGU n.d.).

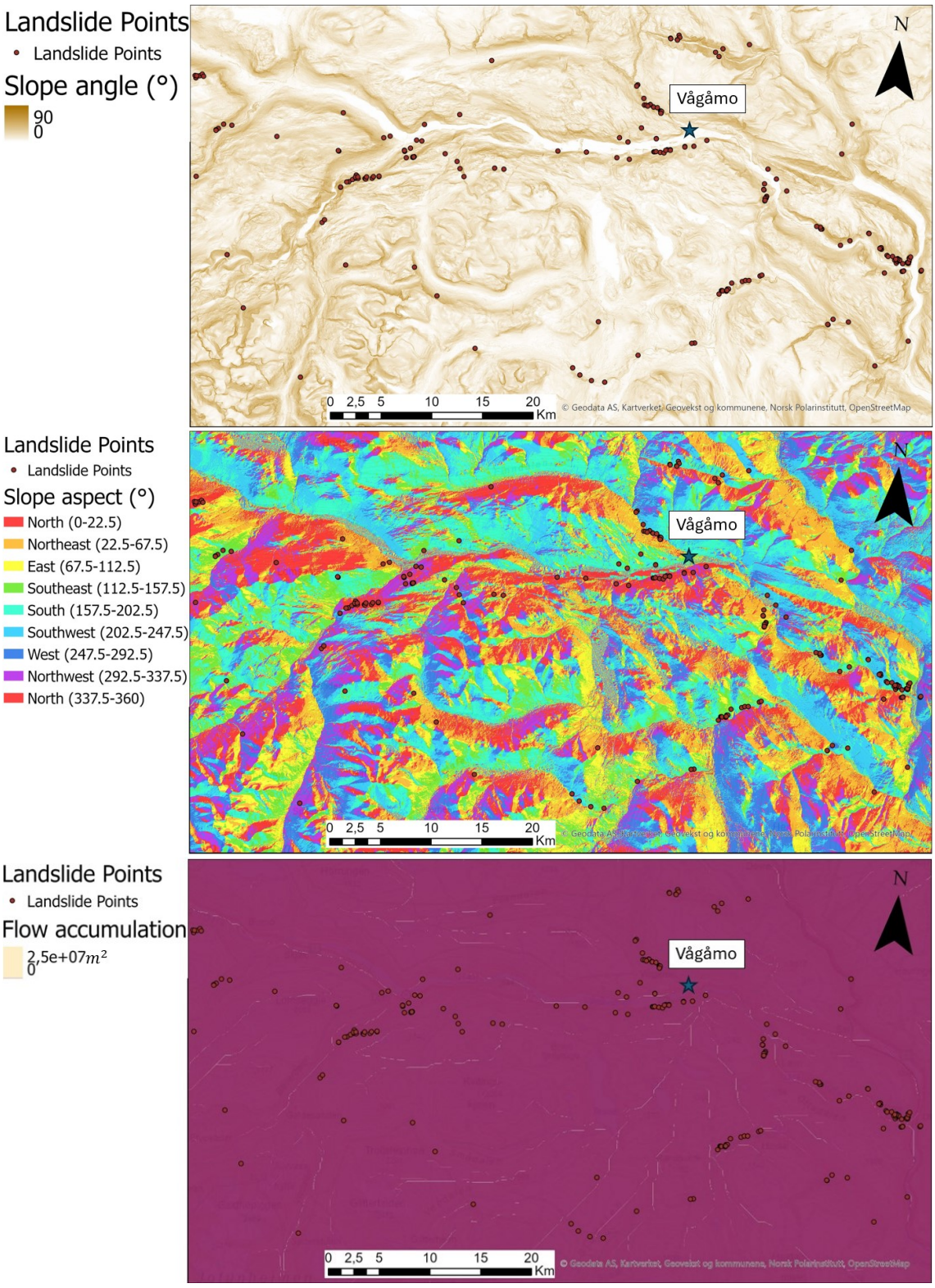

Figure 8: Illustration of three maps showing slope angle (top), slope aspect (middle) and flow accumulation (bottom). Corresponding values and colors are described in the legend. Vågåmo is marked with a blue star and the landslides are marked as brown points.

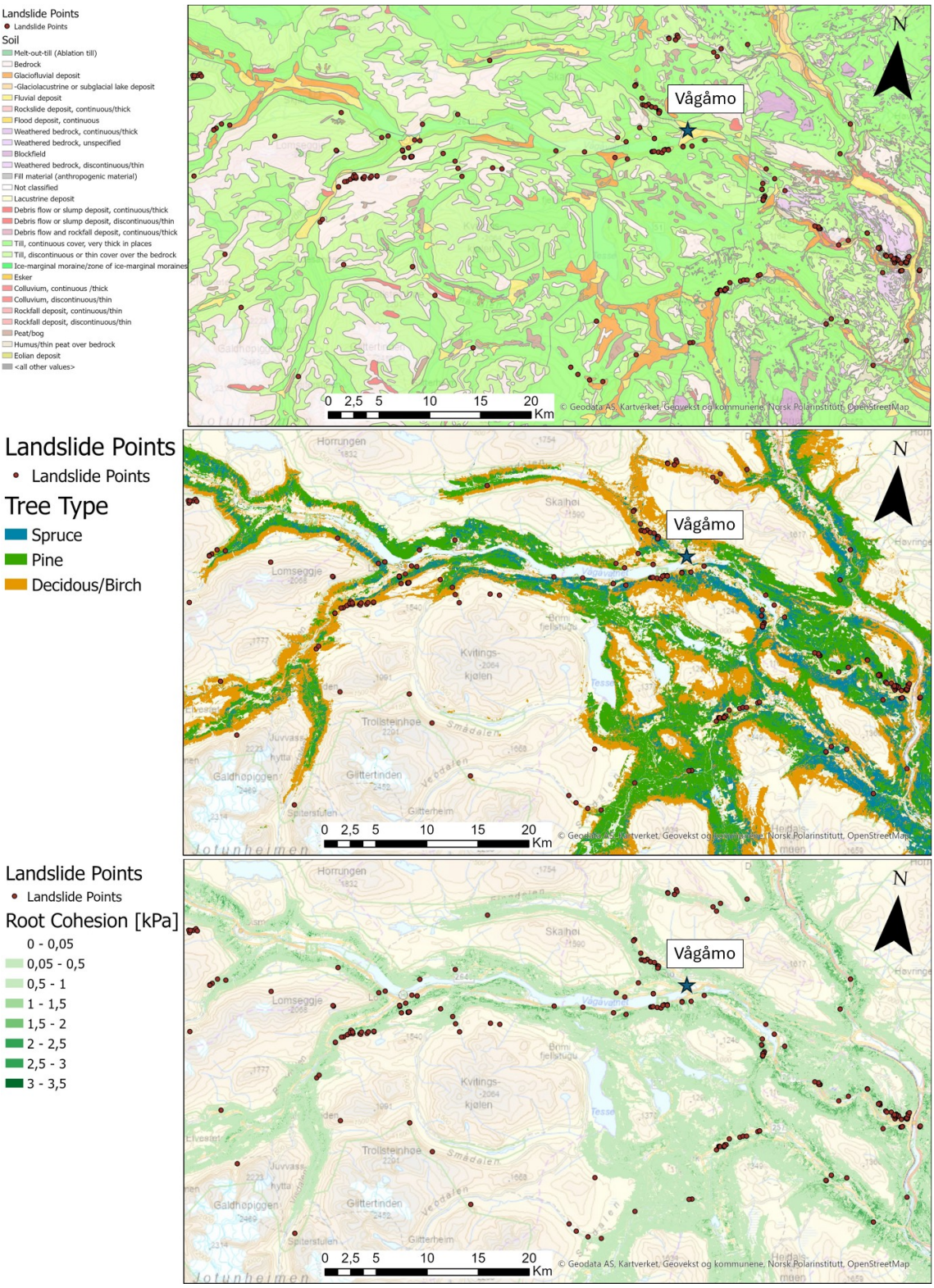

Figure 9: Illustration of three maps showing soil type (top), tree type (middle) and root cohesion (bottom). Corresponding values and colors are described in the legend. Vågåmo is marked with a blue star in the maps and the landslides are marked as brown points. The background map is the OpenStreetMap in ArcGIS Pro.

4.2.7 Method to assess dynamic landslide susceptibility

In a dynamic approach, the input parameters change with time. Information on the landslide initiation date is therefore needed (Nocentini et al. 2023). This information was gathered as described in the Landslide inventory section (4.1.2).

The decision was made to exclusively use the RF model for the dynamic approach. This was because the RF model provided slightly better results regarding performance compared to the LR model. Additionally, the RF model generally performs well according to other studies (Goetz, Brenning et al. 2015; Hussain et al. 2022; Kavzoglu et al. 2019; Khaliq et al. 2023; J. Li et al. 2021; Liu et al. 2021; Merghadi et al. 2020; Ng et al. 2021).

It is essential to remove irrelevant or less relevant parameters in order to improve the efficiency and performance of landslide models as part of the analysis (Liu et al. 2021; Micheletti et al. 2014; Zhou et al. 2018). The precipitation and soil saturation provides additional parameters to the model which further complicates the process. This led to an exclusion of the soil type parameter. The soil type had the least feature importance and was not contributing to the performance of the algorithm.

The dataset used for this approach consisted of 2270 no-landslide pixels and 227 landslides pixels, totaling 2497 pixels. A new "Day" column with the corresponding days between August 7 to 10 was added to the dataset in order to separate them later during testing. This column was removed before training of the model.

The dataset was split into training and test sets with a 70/30 ratio. Using SMOTE, 170 synthetic landslide pixels were generated based on the 158 landslides present in the training set. Consequently, the training dataset comprised 1589 no-landslide pixels and 328 landslide pixels, giving a ratio of $5:1$ $\frac{no-landslide}{landslide}$. The test set consisted of 750 pixels, with varying distributions across the four days. August 7 had 149 pixels, August 8 had 239 pixels, August 9 had 184 pixels, and August 10 had 178 pixels. The datasets was presented to the RF model.

The difference in pixel counts between the days can be attributed to the stratification performed during the train-test split. The stratification was based on the presence of landslides, not the specific day. This approach ensures that both the training and testing sets

contain a balanced number of landslides, which is crucial for maintaining the representativeness and effectiveness of the model (ScikitLearn n.d.[d]). Stratifying by landslides ensures that the model is trained and tested on equally representative samples of landslide and non-landslide data, matching the desired dataset split (70/30).

Figure 10 and 11 shows the precipitation and soil saturation distribution for August 7 to 10. The map bounds is the study area as indicated in Figure 5. The position of Vågåmo is marked with a star, landslides are marked as brown points and the different values of the precipitation and soil saturation are illustrated in the legend.

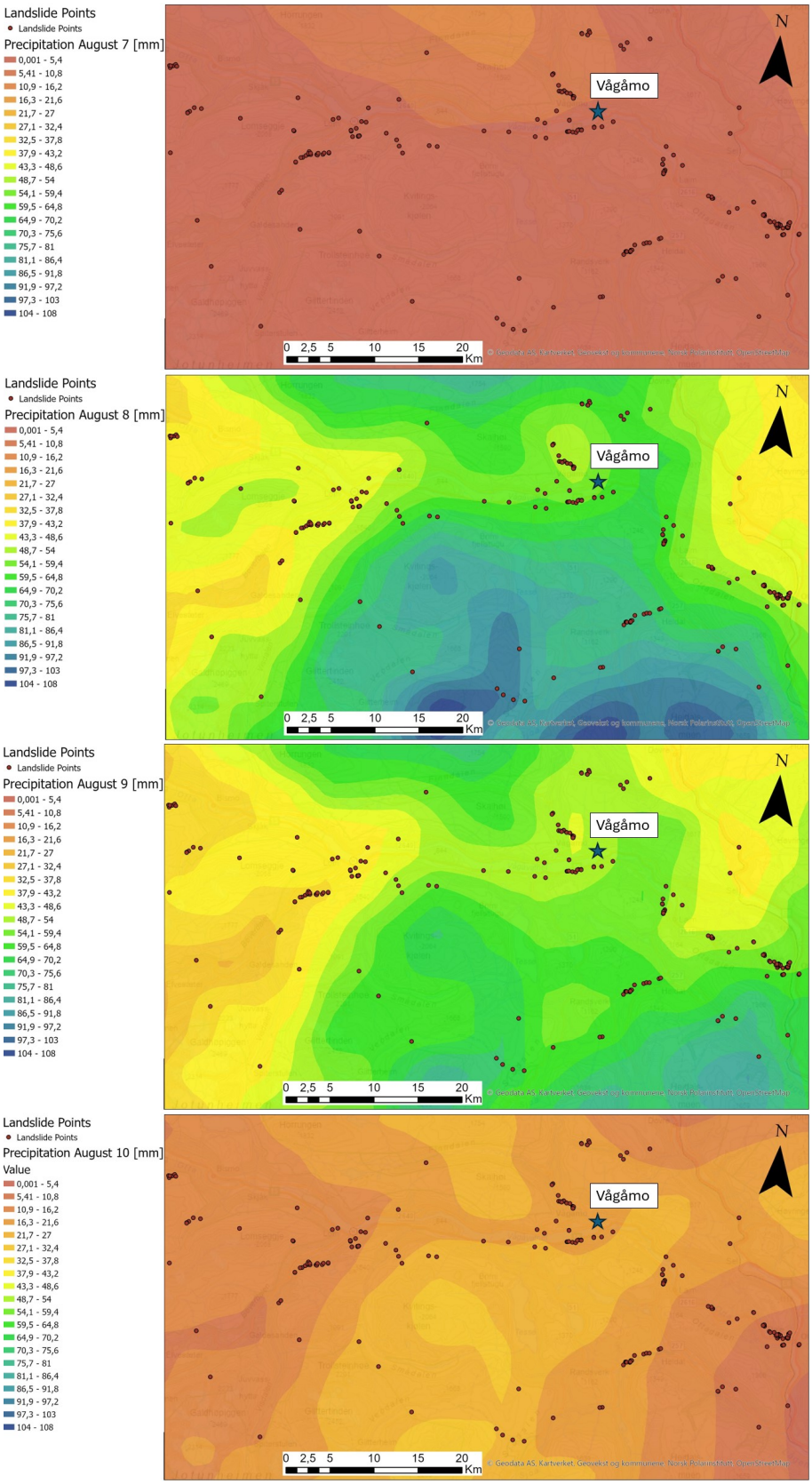

Figure 10: Illustration of the precipitation from August 7 at the top to August 10 at the bottom. The legend is the same for all figures and going from 0 mm (red colors) to 108 mm (blue colors). Vågåmo is marked with a star, and landslides as brown points.

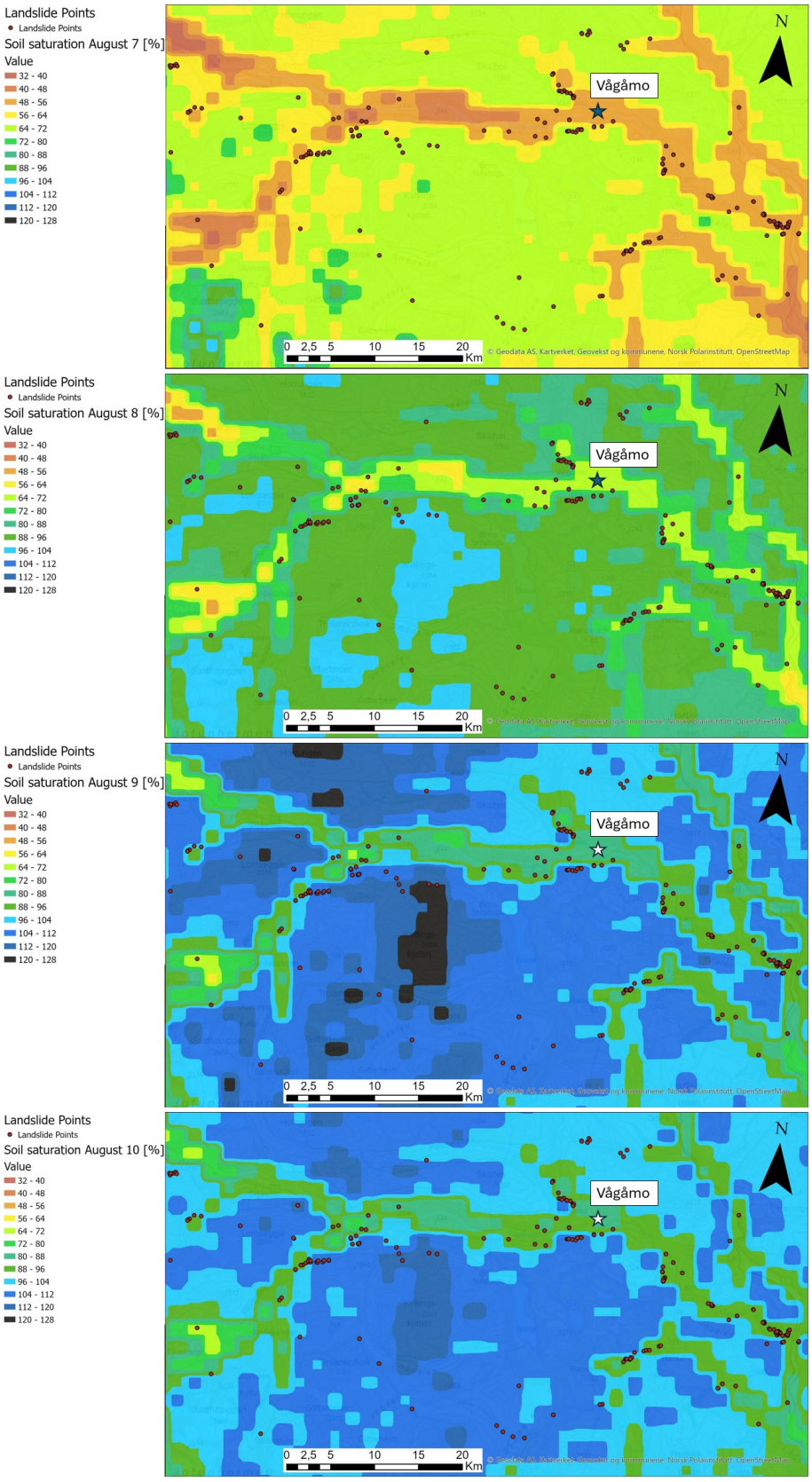

Figure 11: Illustration of the soil saturation degree from August 7 at the top to August 10 at the bottom. The legend is the same for all figures and going from 32% (red colors) to 128% (black colors). Vågåmo is marked with a star, and landslides as brown points.

5 Results

5.1 Analysis of forest parameters

Figure 12a) displays the amount of landslides and the tree type inside the study area. Both landslide amount and landslide frequency in birch (deciduous) forest far exceeds the other forests and areas without forest. The amount of landslides in birch forest is 116 and the frequency almost reached 4.5. The landslide frequency in the other forests are 1.2 and 1.5. The total amount of landslides is 230, so more than half of the landslides initiated in birch forests.

Figure 12b) illustrates the amount of landslides versus the leaf coverage percentage. The highest landslide frequency (3.2) and landslide initiations (83) occur where the leaf coverage is between 90-100%, indicating a tendency to be more frequent in dense forests. Additionally, another peak in landslide frequency is observed at 30-40% leaf coverage. The low amount of landslides (8) but high landslide frequency (2.9) in the 30-40% leaves coverage range indicate that the area is quite small, furthermore providing a high frequency. Compared to for instance the 40-50%, where the landslide frequency drops down to 0.6, which likely represents a larger area.

(a)

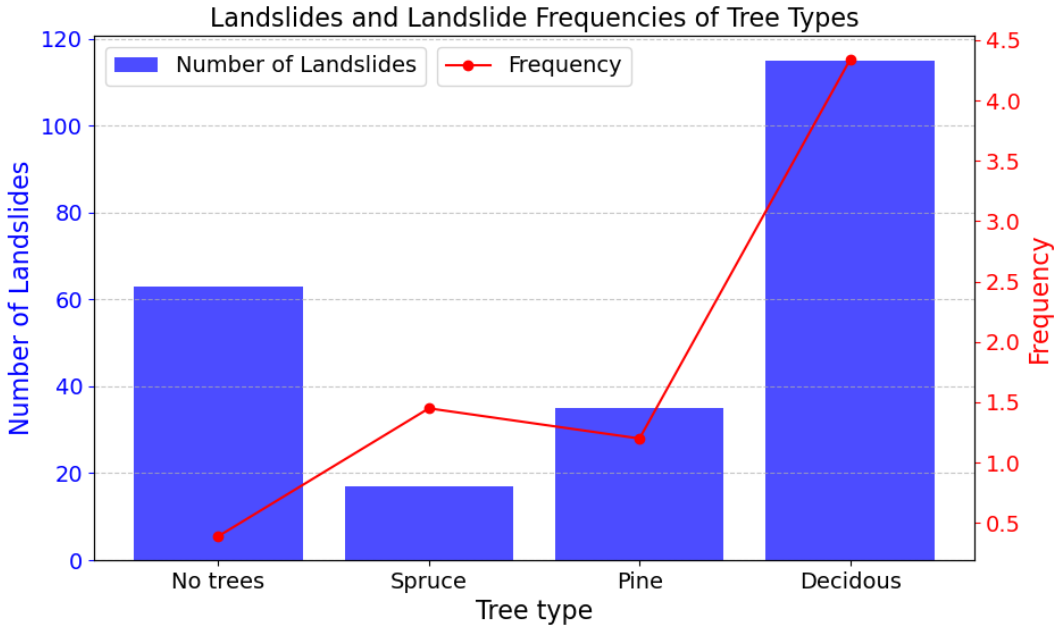

(b)

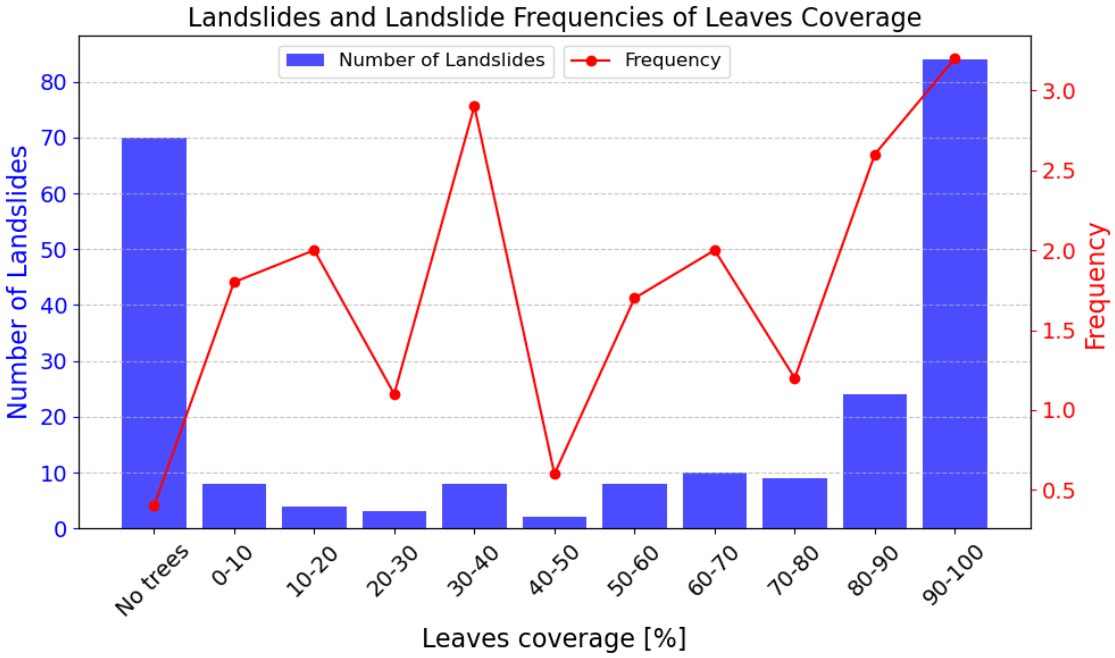

Figure 12: a) is illustrating the number of landslides versus the tree type, while b) is showing the number of landslides versus the leaves coverage. The blue bars are showing the amount of landslides and the red line is showing the landslide frequency, which indicates how "often" landslides initiate for the respective parameters, see Equation 6 for description.

Figure 13a) illustrates the amount of landslides versus the number of trees per hectare with a diameter greater than 5 cm at breast height (1.3 meters above ground). The data reveals a trend of increasing landslide frequency correlating with a higher density of trees per hectare. The highest landslide frequency (7.5) occurs in areas with the greatest tree density, ranging from 2400 to 2800 trees per hectare. Most landslides (34) occur (not considering where there is no trees) when the mean amount of trees ranges between 1600 to 2000 trees per hectare.

The same trend is observed in Figure 13b) which examines trees with a diameter of 16 cm at breast height, indicating larger trees compared to a). The highest landslide frequency (6) again occurs in areas with the greatest tree density, where the mean amount of trees per hectare range from 800 to 900. Additionally, a smaller peak in landslide frequency (3.6) is noted where tree density is between 300 and 400 trees per hectare. The amount of landslides (35) is also highest in this range, not counting areas without trees. The same peak at 300 and 400 trees per hectare is also seen where the leaves coverage is around 30-40% in Figure 12b).

(a)

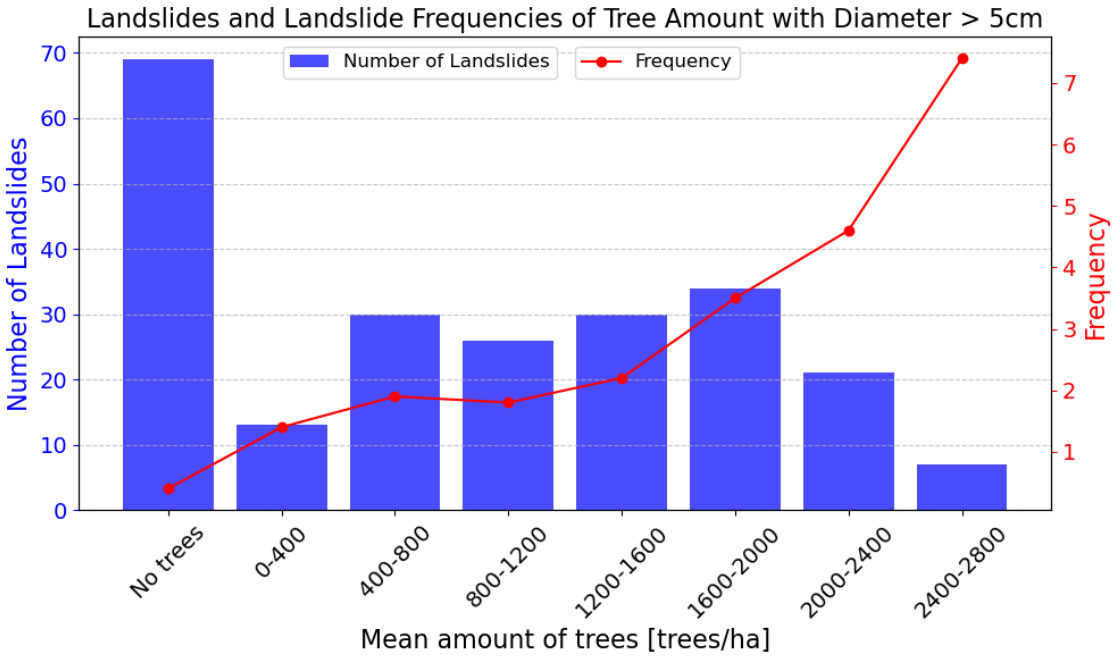

(b)

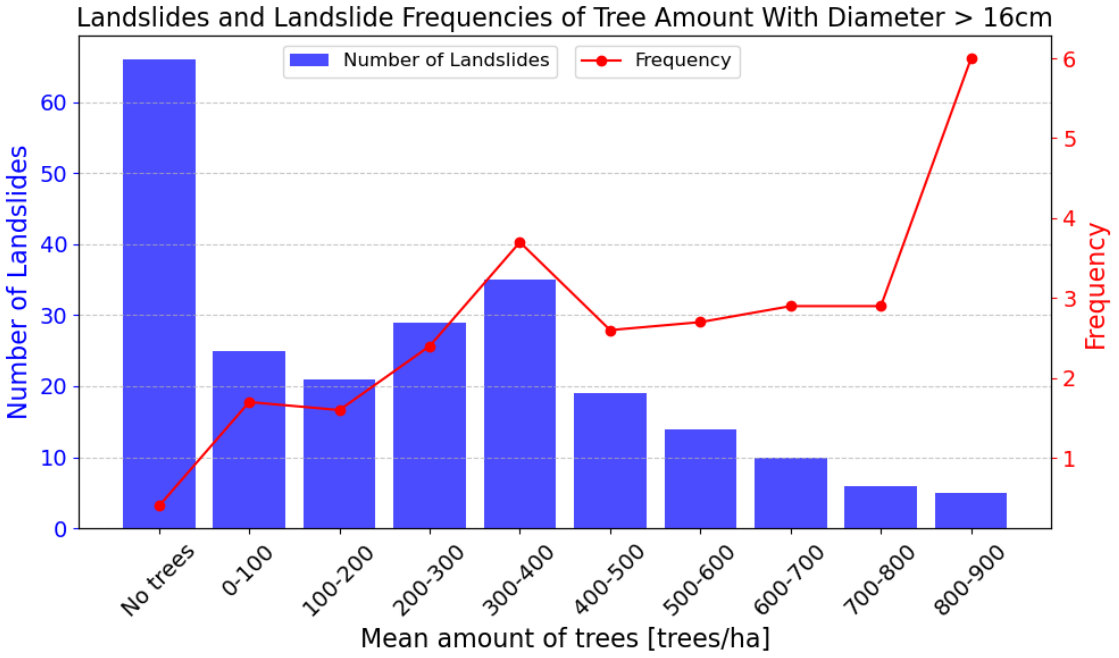

Figure 13: a) shows trees with a diameter at breast height (1.3 meter above ground) bigger than 5 cm and b) shows trees with a diameter bigger than 16 cm at breast height. The blue bars are showing the landslide amount and the red, dotted line is indicating the landslide frequency, which indicates how “often” landslides initiate for the respective parameters, see Equation 6 for description.

Figure 14a) shows the amount of landslides versus the mean tree height (dm). The highest landslide frequency (3.5) is observed when the tree height is between 15-20 meters. Also a high landslide frequency (3.1) is seen where the tree height is between 20-25 meters. The highest amount of landslides (63) is seen when the trees are between 10-15 meters high, again not considering areas without trees. Additionally, a frequency peak (2.8) is observed when trees have a height between 0-5 meters. Overall, the figure indicates highest landslide frequency with greater tree height.

Figure 14b) depicts the amount of landslides versus the mean tree diameter (cm) at breast height. The highest landslide frequency (2.9) occurs where trees have a diameter of 10-20 cm and 30-40 cm. The actual number of landslides is significantly higher in the 10-20 cm range (110) compared to the 30-40 cm range (1), despite similar frequency. This indicates a relatively small area coverage of relatively large trees with a diameter of 30-40 cm.

(a)

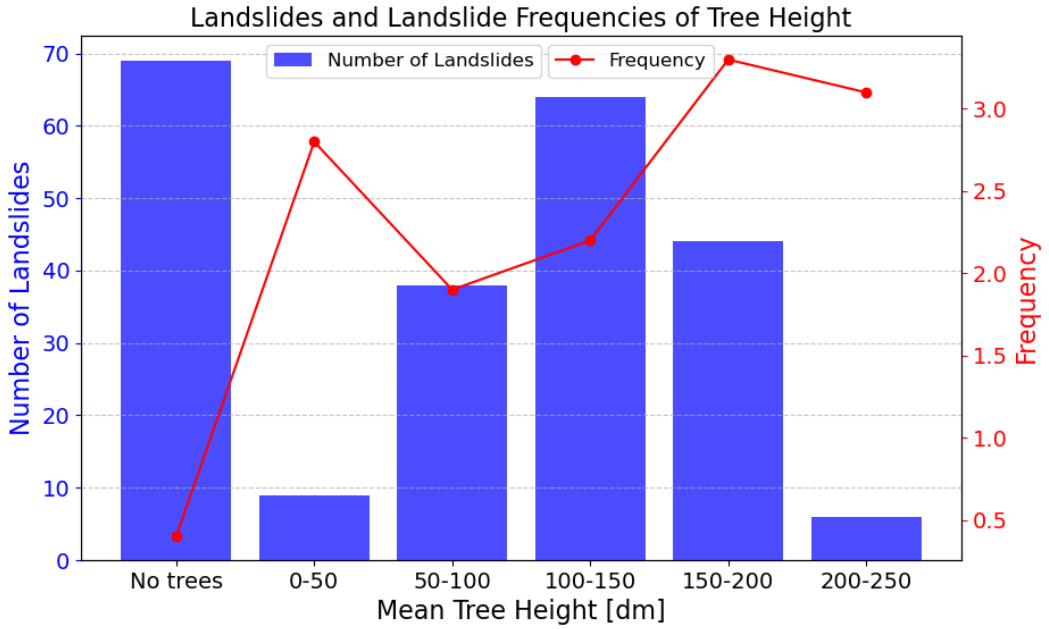

(b)

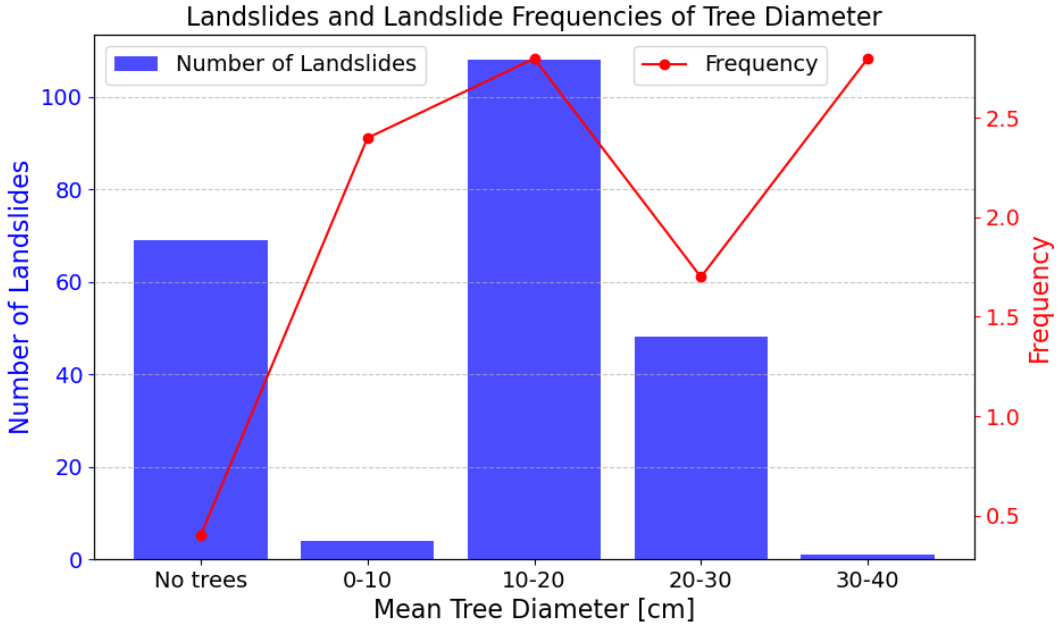

Figure 14: a) is illustrating the number of landslides versus the mean tree height (dm), while b) is showing the number of landslides versus the mean tree diameter (cm) at breast height (1.3 meters above ground). The blue bars are showing the amount of landslides and the red line is showing the landslide frequency, which indicates how “often” landslides initiate for the respective parameters, see Equation 6 for description.

Figure 15 shows the diameter (cm) at breast height and height (m) for the different tree types inside the study area. The x-axis represents the upper limit of each bin. That means a diameter between 11-20 cm is placed in the 20 cm bin. It can be seen that the spruce forest shows a diameter mostly between 10-30 cm, while pine and birch (deciduous) trees shows primarily diameters of 30 and 20 cm, respectively. The tree height distribution shows the spruce ranging mostly around 20 meters but has trees reaching 30 meters. Most pine trees have a tree height of 15 meters , but also 5 meters and 25 meters. The birch trees are mainly around 10 and 15 meters height, with some at 5 and 20 meters. It can also be depicted from the figure that the total area of spruce forest is smaller than the area of pine and birch forests.

(a)

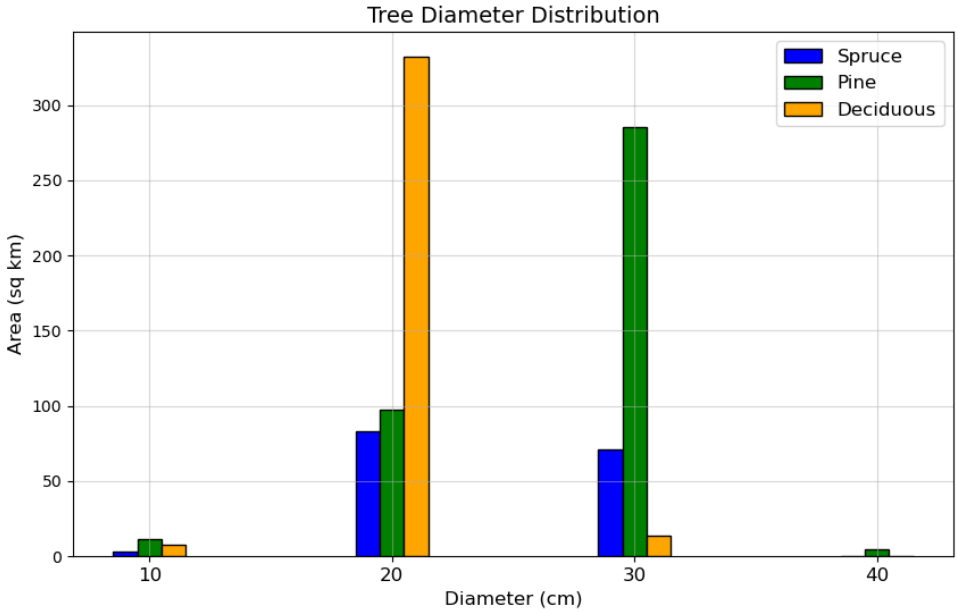

(b)

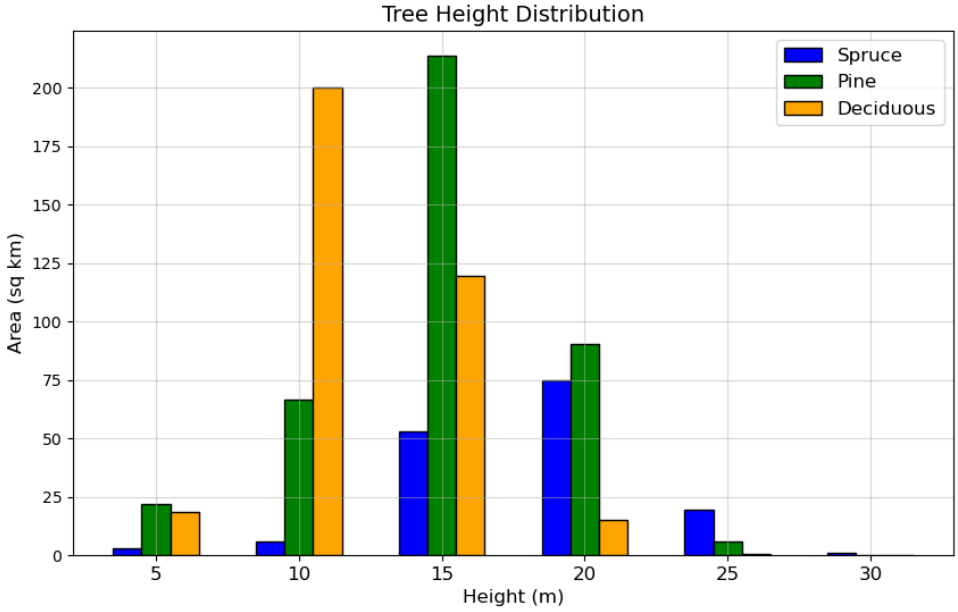

Figure 15: a) shows the mean tree diameter (cm) distribution at breast height (1.3 meters above ground) for the different trees while b) shows the mean tree height (m) distribution. The blue bars shows spruce, the green bars shows pine and the orange bars shows birch (deciduous) inside the study area.

5.2 Results static susceptibility maps

5.2.1 Maps

To be able to compare the two models and the susceptibility maps, an equal break method was utilized. This process involved classifying the map into four probability classes: 0-0.25, 0.25-0.5, 0.5-0.75, and 0.75-1, which indicate the predicted probabilities of landslides from low to high. Low values indicate a "safe area" from mass movement activity and high values indicate a probability of landslide occurrence. The resulting susceptibility map produced by the RF model is shown in Figure 16a) and the map generated from the LR model is shown in Figure 16b).

The area distribution of probabilities in percentages is shown in Figure 17. The figure presents histograms displaying the area percentages for different probability ranges for both RF and LR models. The green bars show the RF model while the red bars show the LR model.

There is a noticeable correlation of susceptibility zones between the two maps. Additionally, the lack of landslides aligns well with the predicted low landslide susceptibility. For both models, all landslide probability zones (except for the 0-0.25 range) are primarily located in the valleys of the study area, matching the actual landslide locations.

Both maps show extensive areas of low landslide susceptibility, with around 80% of the area falling in the 0-0.25 range. RF assigns a higher area percentage (14%) in the 0.25-0.5 probability range compared to the LR (10%). In the 0.5-0.75 range, both models exhibit similar results with around 6% area coverage. A notable difference occurs in the probability range between 0.75-1, where the LR assigns a higher percentage of area compared to the RF, with 4% against 1%.

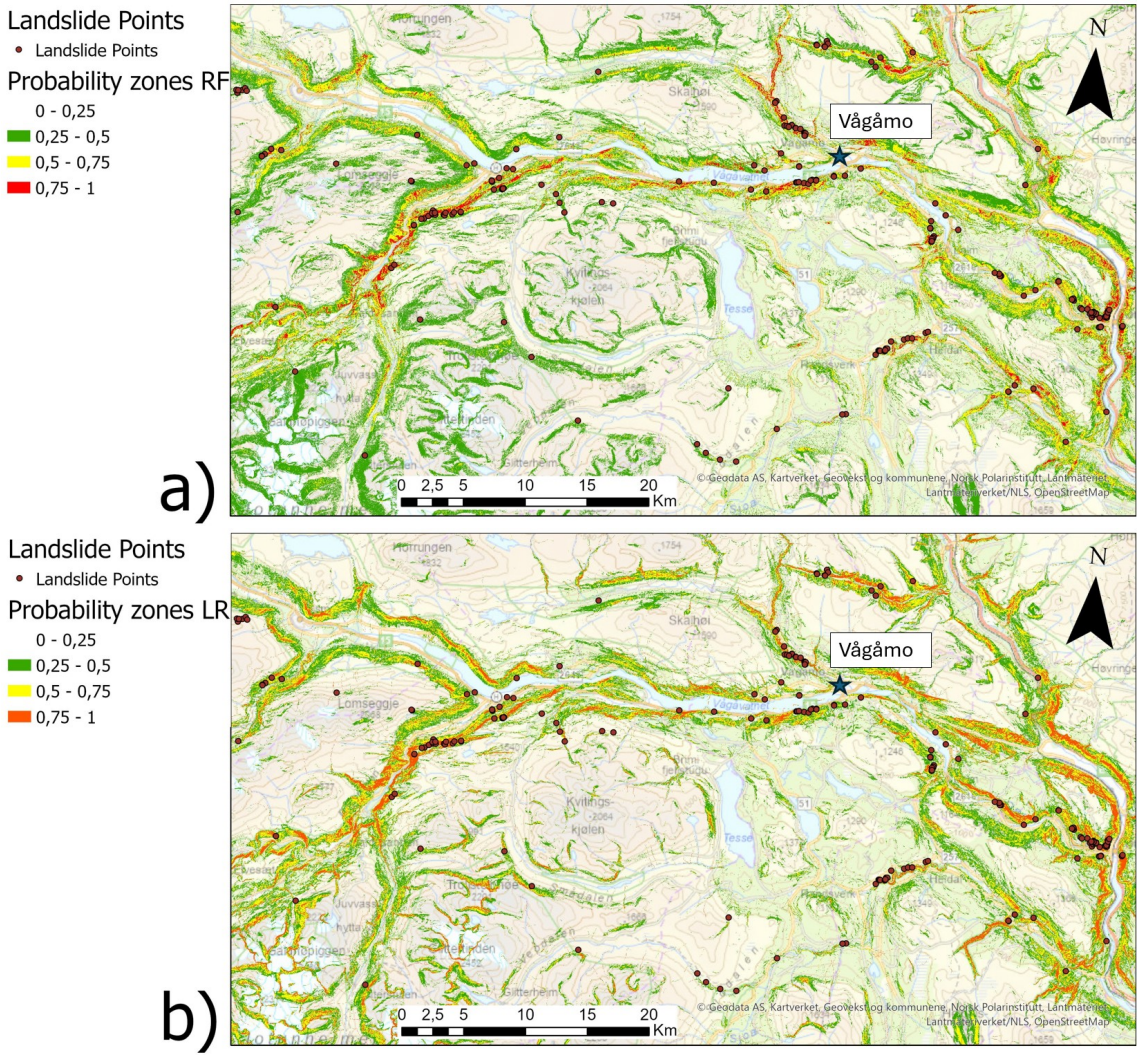

Figure 16: Comparison of susceptibility maps generated from Random Forest (a) and Logistic Regression (b). The range between 0-0.25 probability has no color in the map. This was done to emphasize the other probabilities. Vågåmo is marked with a blue star, and a north arrow and scale bar is placed inside the map. The background map is the OpenStreetMap in ArcGIS Pro.

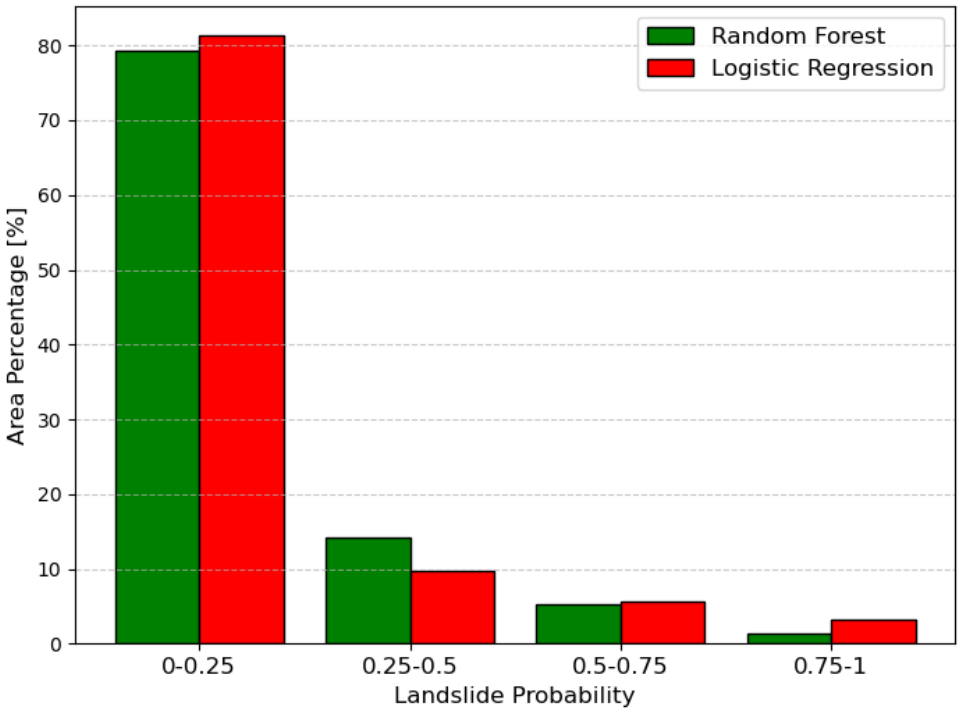

Figure 17: Area percentages of the landslide probabilities shown in Figure 16. The map generated with Random Forest is shown as green bars and the map generated with Logistic Regression is shown as red bars. The respective probability zones are indicated on the x-axis and the area percentages are shown on the y-axis.

5.2.2 Evaluation of model performance

It is observed from Table 9 that the *Flow accumulation* and the *Soil type* is contributing the least to the RF, while the *Slope angle* is the most important. The *Soil type* and *Slope aspect* has the least influence in the LR, with *Slope angle* again being the most important. The VIF varies between 1 and 1.7, indicating no multicollinearity.

Table 9: Values indicating the Variance Inflation Factor (VIF) and the Feature Importance for Random Forest and Logistic Regression.

Parameter	VIF	Random Forest	Logistic Regression
		Feature importance	Feature importance
Slope angle	1.3	0.48	1.49
Root cohesion	1.7	0.21	0.32
Slope aspect	1	0.09	0.15
Tree type	1.7	0.09	0.27
Flow accumulation	1	0.07	0.29
Soil type	1	0.05	0.17

Table 10 shows the TN, FP, FN and TP of both RF and LR. Both models predict almost the same amount of TP (50 and 49). The most considerate difference is that the LR predicts more FN and FP, and less TN compared to the RF. Based on the confusion matrix the performance indicators is shown in Table 11. The RF obtains better scores for all the indicators compared to LR. The ROC curve can be drawn based on the confusion matrix and different thresholds, with a corresponding AUC value. The ROC curve is shown in Figure 18. The curves follow each other closely, with the RF obtaining a slightly higher AUC value compared to the LR, with 0.93 compared to 0.91.

Table 10: Confusion Matrix from Random Forest and Logistic Regression, indicating the amount of landslide pixels predicted as TN, FP, FN, and TP.

	Random Forest		Logistic Regression	
	Predicted Negative	Predicted Positive	Predicted Negative	Predicted Positive
Actual Negative	191	14	185	20
Actual Positive	18	50	19	49

Table 11: Performance indicator values based on the confusion matrix in Table 10.

Performance indicators	Random Forest	Logistic Regression
Accuracy	0.88	0.86
Precision	0.78	0.71
Efficiency Index	0.61	0.56

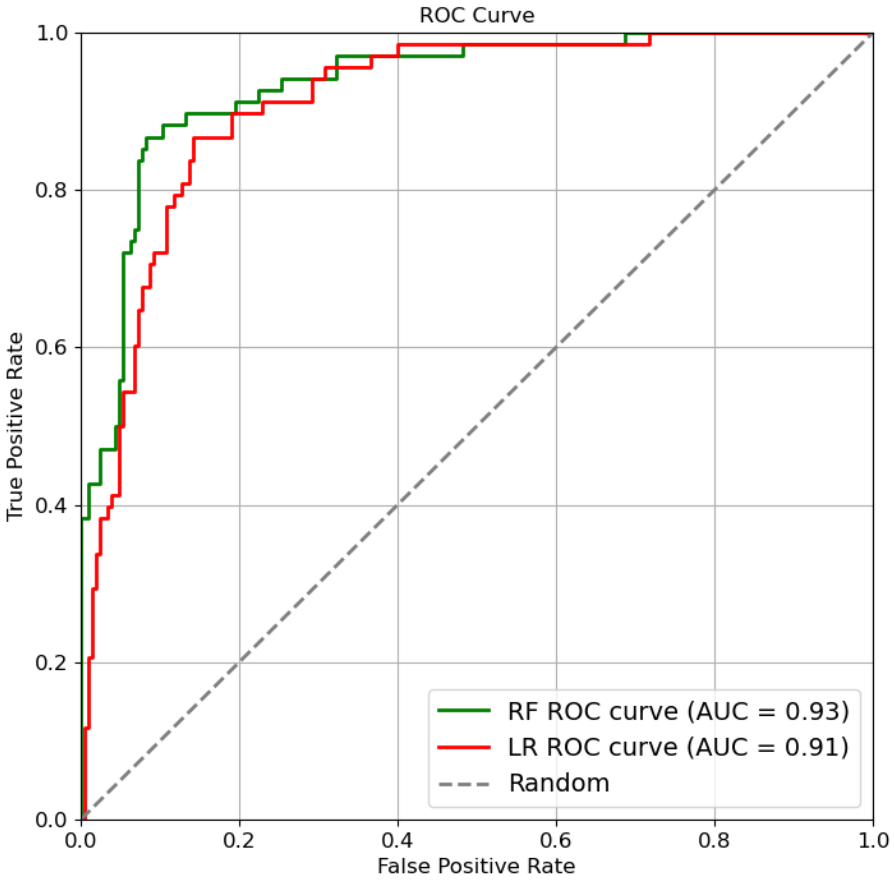

Figure 18: Reciever Operating Characteristic (ROC) curve of Random Forest (green) and Logistic Regression (red) models, indicating the relationship between True Positive Rate and False Positive Rate. The Area Under the Curve (AUC) is indicated in the legend and a random predictor model is shown as a grey, dotted line.

Table 12 shows the actual landslide pixels (227 in total) overlaid on the predicted maps generated by the RF and LR models. The RF assigned 12 actual landslide pixels a prob-

ability between 0-0.25, while the LR assigns 38 landslide pixels to this range. Moreover, the RF and LR assigned 50 and 45 landslide pixels, respectively, a probability between 0.25-0.5. For the probability between 0.5-0.75, the RF assigned 84 landslide pixels and the LR assigned 80 landslide pixels within this range. Finally, in the 0.75-1 probability range, the RF assigned 81 landslide pixels and the LR assigned 64 landslide pixels.

Table 12: Overview of actual landslide pixels overlaid on the predicted maps generated by the Random Forest (RF) and Logistic Regression (LR) models.

Probability zones	Landslides (RF)	Landslides (LR)
0 - 0.25	12	38
0.25 - 0.5	50	45
0.5 - 0.75	84	80
0.75 - 1	81	64

5.3 Results of dynamic susceptibility maps

When reviewing this part of the results, it is important to recognize that the reference times for August 7 to 10 are as outlined in Table 6.

5.3.1 Maps

The spatio-temporal susceptibility maps are displayed in Figure 19 and 20. The equal break method was also utilized for these maps. An additional range of landslide probability between 0-0.1 was included to illustrate the distribution of landslide susceptibility for August 7 and 10 in the maps without covering the area completely. The respective probability zones, ranging from low to high, are therefore defined as 0-0.1, 0.1-0.25, 0.25-0.5, 0.5-0.75 and 0.75-1.

Figure 19 shows the landslide susceptibility maps for August 7 and 8. On August 7 only small patches of green are visible, for instance around the glaciers in the southwestern part of the map. Overall, the probability of landslides is low across the study area. In contrast, on August 8, both the probability of landslides and the affected area is significantly higher.

The landslide susceptibility is highest in the valley areas, but this time to a much wider extent compared to the static maps (Figure 16).

Figure 20 shows the landslide susceptibility maps for August 9 and 10. August 9 also shows high landslide probability over a large area, though not as pronounced as August 8. The probability of landslides on August 9 is more concentrated on the eastern part of the map compared to the western part, but also in the valleys. On August 10, the likelihood of landslides is generally low, mirroring the conditions on August 7. However, there is a larger area displaying a landslide probability between 0.1-0.25 on August 10 compared to August 7. Nonetheless, the overall probability of landslides remains low.

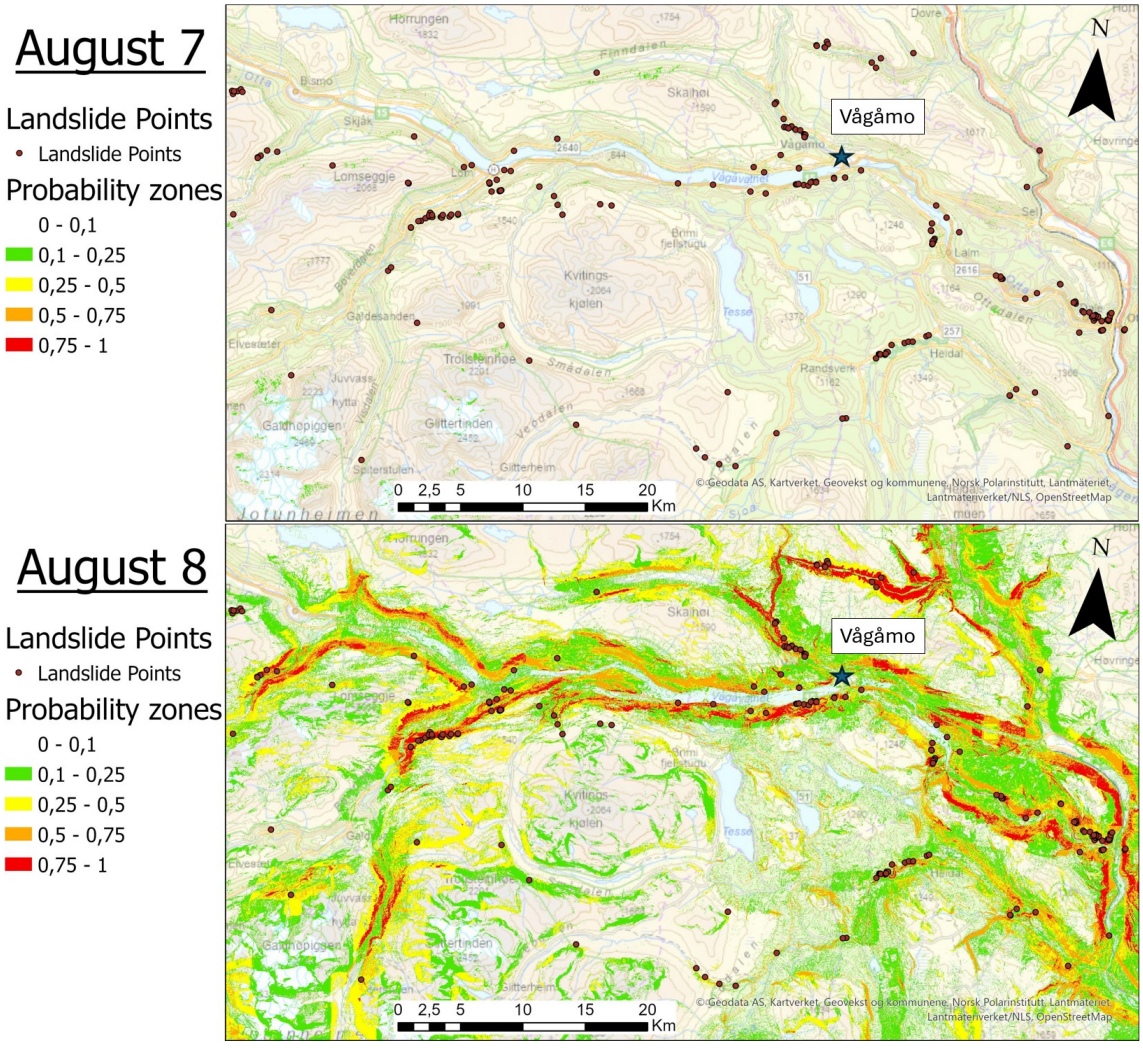

Figure 19: Comparison of susceptibility maps generated from Random Forest model for August 7 and 8. The range between 0-0.1 probability has no color in the map. The background map is the OpenStreetMap in ArcGIS Pro.

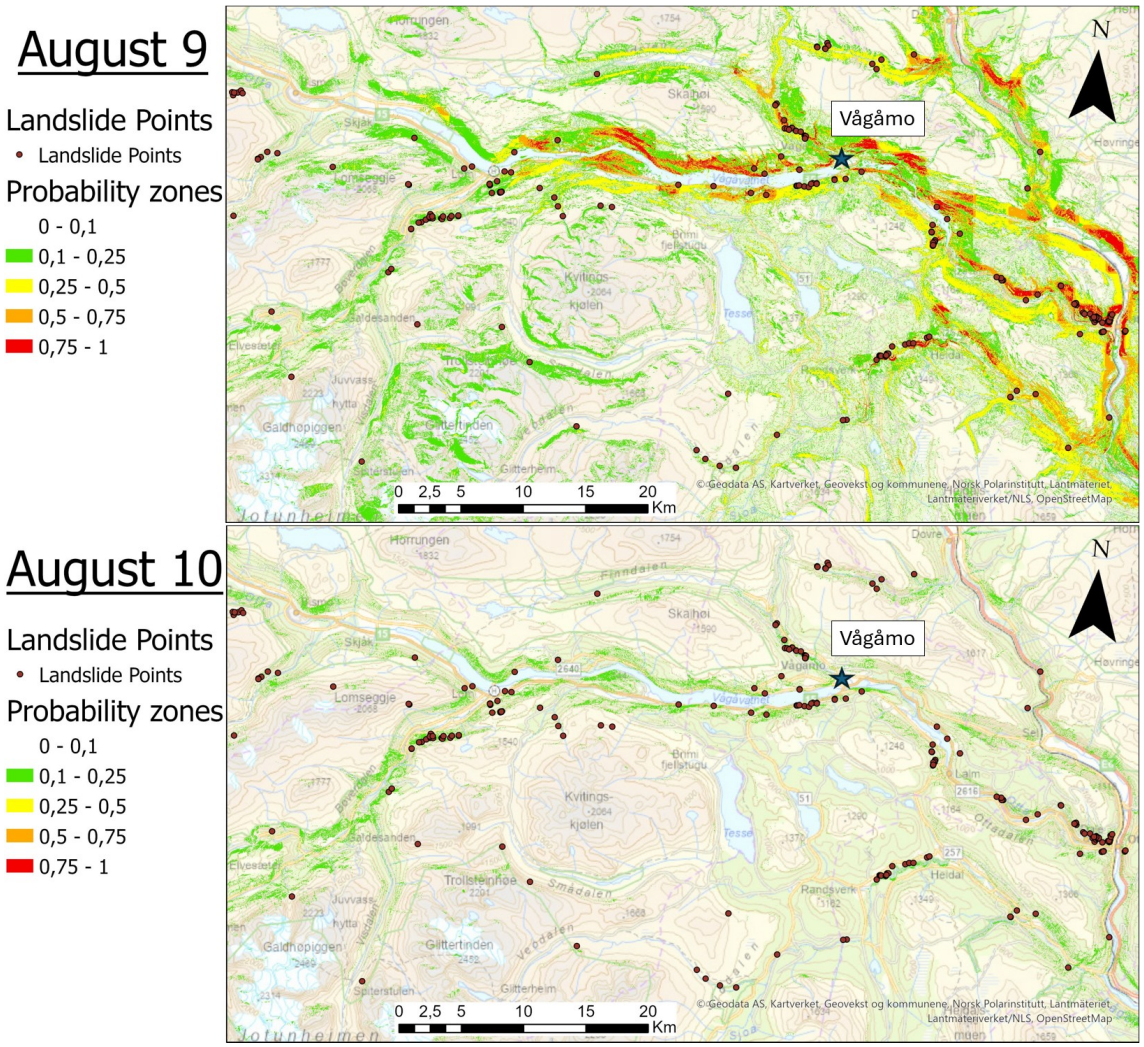

Figure 20: Comparison of susceptibility maps generated from Random Forest model for August 9 and 10. The range between 0-0.1 probability has no color in the map. The background map is the OpenStreetMap in ArcGIS Pro.

Figure 21 shows the area percentage of different probability ranges for each day. Both August 7 and 10 are completely covered in landslide probabilities within the 0-0.25 range. On August 8, 80% of the area falls within this range, while on August 9, it is 92%. All landslide probability ranges are present on August 8 and 9, with August 8 consistently covering a larger area than August 9 across the highest probability ranges. Specifically, in the 0.25-0.5 range, August 8 displays 12% area coverage compared to 5% on August 9. For the 0-5-0.75 range, August 8 covers 5% of the area while August 9 covers 2%. In the highest probability range (0.75-1), August 8 covers 3% whereas August 9 covers 1%.

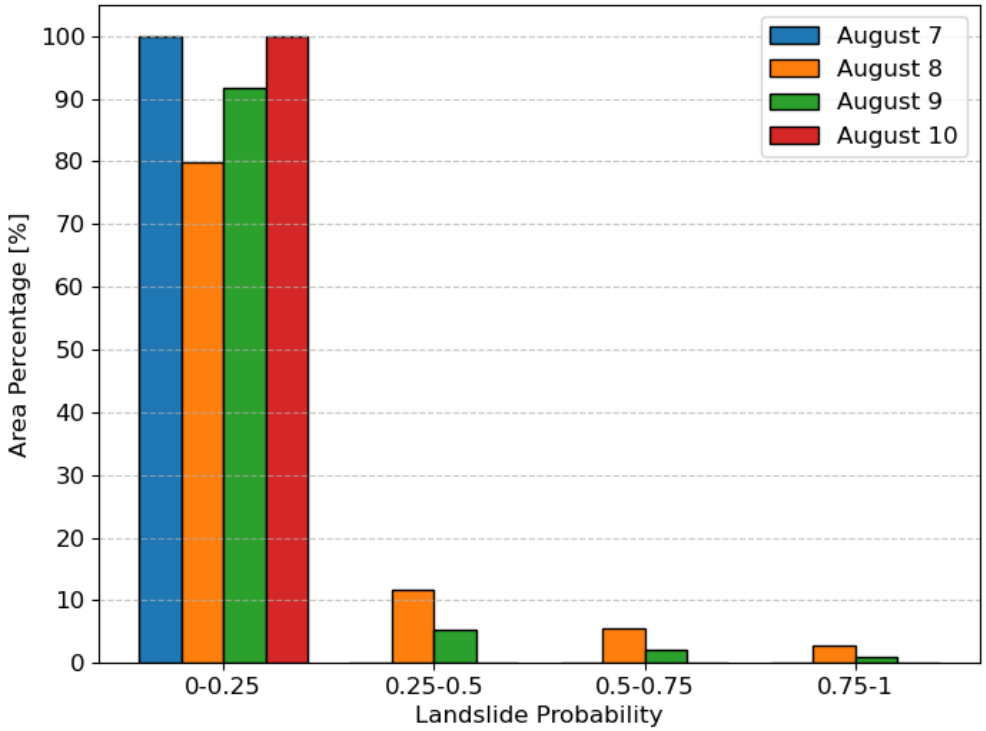

Figure 21: Percentages of the different landslide probabilities during August 7-10. The respective probability zones are indicated on the x-axis and the area percentage is shown on the y-axis.

Figure 22 displays the same susceptibility maps as before for August 8 and 9, but this time representing landslides that initiated on the respective dates. The distribution of landslide probability and landslide initiation points correlate quite well on August 8. The landslide susceptibility covers large areas but seems to follow the pattern of landslide locations. Similarly, on August 9, areas of high predicted landslide probability are primarily concentrated in the eastern part of the map, aligning with the spatial distribution of landslide initiation areas.

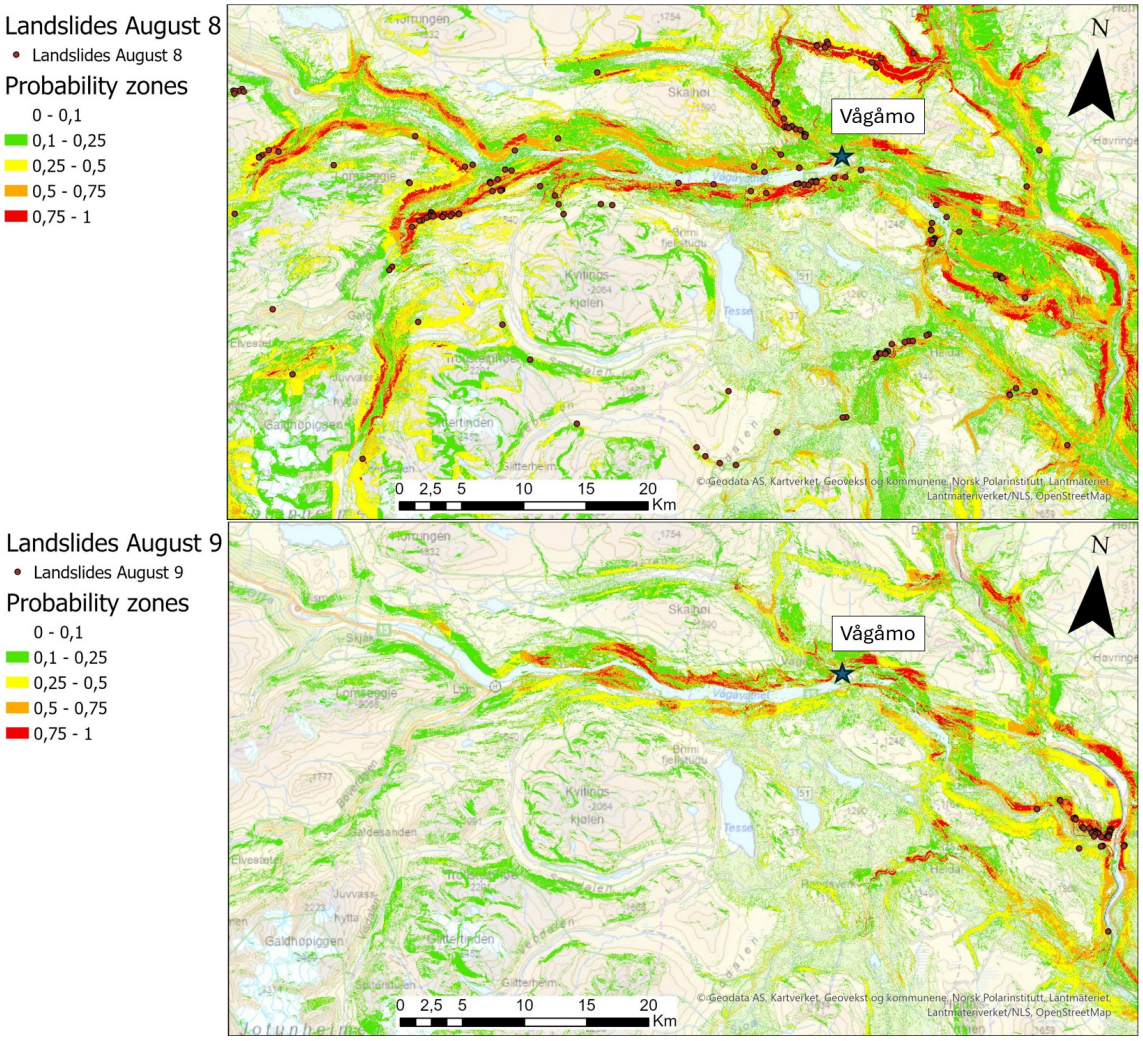

Figure 22: Susceptibility maps and corresponding landslide initiation points on different dates, August 8 and 9. The range between 0-0.1 probability has no color in the map. The background map is the OpenStreetMap in ArcGIS Pro.

5.3.2 Evaluation of model performance

Table 13 shows the feature importance. It is seen that *Tree type*, *Slope Aspect* and *Flow Accumulation* has a much lower value compared to the other features. *Slope angle* was the most important feature followed by *precipitation*. *Soil saturation* and *root cohesion* are equally important. The VIF is not included here as the RF is not affected by multicollinearity in the same way as the LR (Yao et al. 2023). This is because the RF generates an ensemble of decision trees instead of assigning weights to the different parameters (Section 2).

Table 13: Feature importance from Random Forest model with dynamic approach.

Parameter	Feature Importance
Slope angle	0.33
Precipitation	0.26
Root cohesion	0.16
Soil saturation degree	0.16
Tree type	0.05
Slope aspect	0.03
Flow accumulation	0.02

The confusion matrices for August 7 to 10 is shown in Table 14 and 15. August 7 and 9 had 149 and 178 test pixels, respectively, and the model accurately predicted all of them as TN. On August 8 the model correctly predicted 48 TP and 167 TN, but also predicted 17 FP and seven FN. On August 9, it successfully predicted 166 TN and 10 TP, with five occurrences of FP and three occurrences of FN.

Table 14: Confusion Matrix from Random Forest, indicating the amount of landslide pixels predicted either as TN, FP, FN, and TP for August 7 and 8.

	August 7		August 8	
	Predicted Negative	Predicted Positive	Predicted Negative	Predicted Positive
Actual Negative	149	0	167	17
Actual Positive	0	0	7	48

Table 15: Confusion Matrix from Random Forest, indicating the amount of landslide pixels predicted either as TN, FP, FN, and TP for August 9 and 10.

	August 9		August 10	
	Predicted Negative	Predicted Positive	Predicted Negative	Predicted Positive
Actual Negative	166	5	178	0
Actual Positive	3	10	0	0

Performance indicators of August 8 and 9 is given in Table 16. Unfortunately, it cannot be assigned performance indicators for August 7 and 10 since the confusion matrix does not include any TP, FP or FN. It is therefore not feasible to compute the ROC curve either. Considering August 8 and 9, the *precision* and *EI* are higher for August 8 compared to August 9. *Precision* reach a value of 0.74 and 0.67, while the *EI* reach a value of 0.67 and 0.56. The accuracy is relatively high, primarily because of the substantial number of correctly predicted TN. The ROC curve and AUC value for August 8 and 9 are displayed in Figure 23.

Table 16: Performance indicator values of August 8 and 9 based on the confusion matrices in Table 14 and 15.

Performance indicators	August 8	August 9
Accuracy	0.9	0.96
Precision	0.74	0.67
Efficiency Index	0.67	0.56

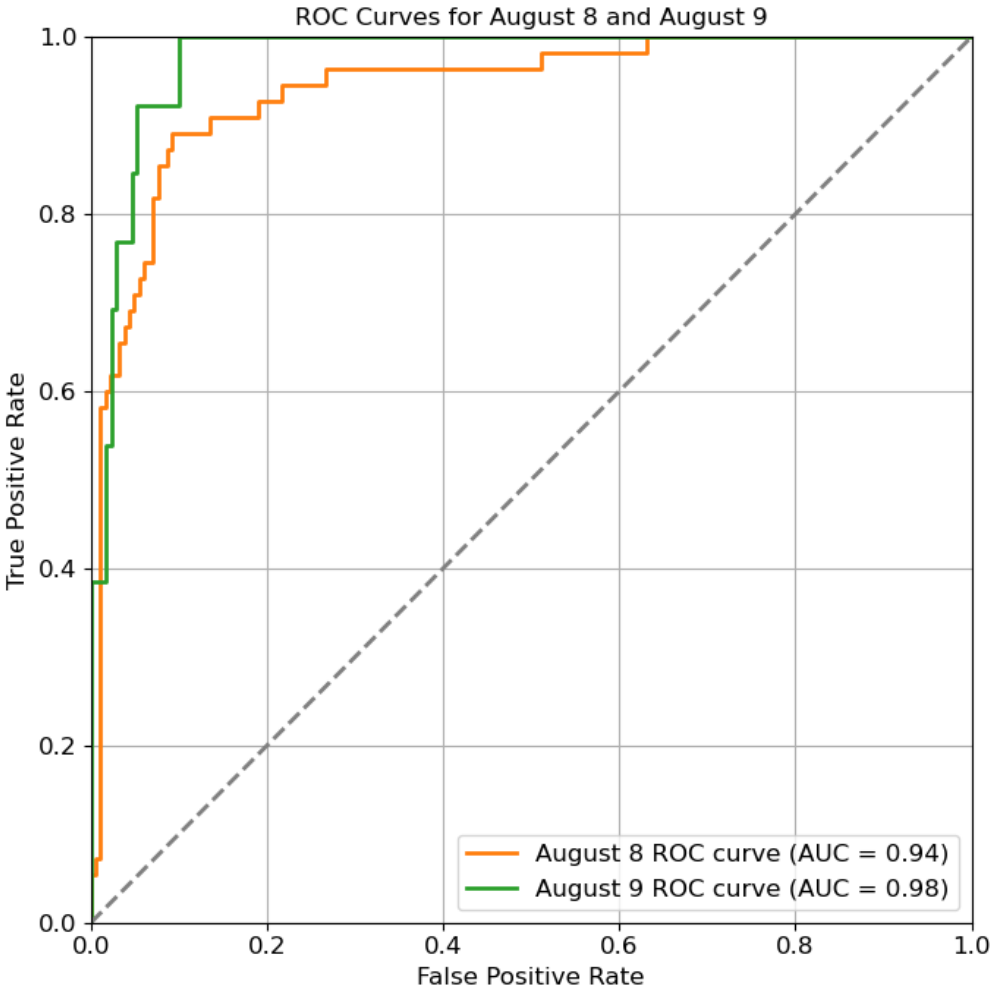

Figure 23: Receiver Operating Characteristic (ROC) curve of August 8 and 9 with Random Forest. The ROC curve is indicating the relationship between True Positive Rate and False Positive Rate. The Area Under the Curve (AUC) is indicated in the legend and a ROC curve equal to 0.5 is shown as a grey, dotted line.

In order to show the performance of the model including August 7 and 10, a discrimination diagram was made (Figure 24). The discrimination diagram plots the likelihood of landslide against the predicted probability for "Observed" cases (Landslide) and "Not Observed" cases (No landslide) (CAWCR 2015). The y-axis represents the likelihood that a given prediction (landslide or no landslide) falls within a specific probability bin. Perfect discrimination would be no overlapping bars, where the "Observed" bars are entirely

separate from “Not Observed”. Overlapping bars indicate some model uncertainty.

Figure 24 shows good results for “Not Observed” cases, with a zero probability of landslide having a likelihood of 0.85. Although bars are present in the probability bins up to 0.8, they have a low likelihood. The “Observed” bins are predominantly located in the higher probability ranges, with the highest likelihood (0.4) occurring at a predicted probability of 0.8. The “Observed” cases are, like the “Not Observed”, spread across the probability ranges but with generally low likelihood. Overall, the discrimination diagram indicates that the model has a high likelihood of correctly predicting TN, and a lower likelihood when predicting TP. This is also evident in the confusion matrices (Table 14 and 15).

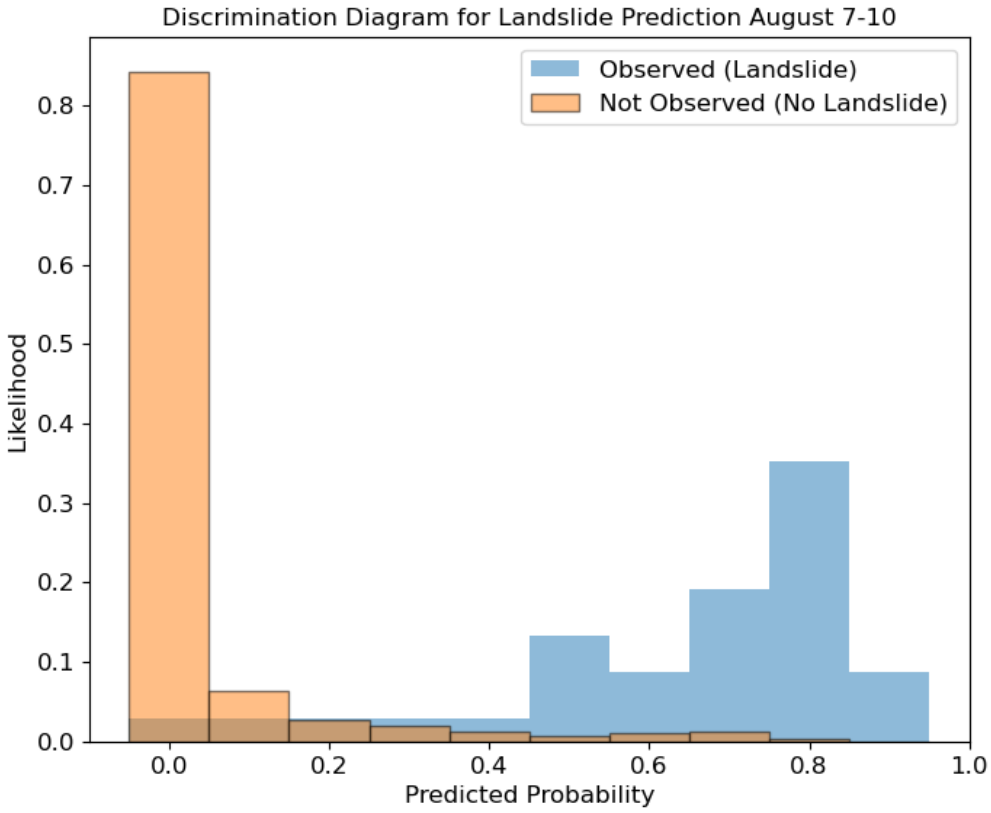

Figure 24: Discrimination Diagram for August 7 to 10. The likelihood represent the probability that a given prediction falls within a specific bin. The specific bins of probability for landslides is shown on the x-axis. The orange bars are cases of “Not Observed” cases (Not landslides). “Observed” cases are shown as blue bars and indicate cases of landslides.

Table 17 shows the actual landslide pixels overlaid on the predicted rasters generated by the RF model for August 8 and 9. August 7 and 10 are excluded since no landslides occurred on these days and the susceptibility maps only showed landslide probabilities in the 0-0.25 probability range. Only the landslides that actually initiated on the respective dates were accounted for (Section 4.1.2), totaling 175 landslides on August 8 and 52 on August 9 (227 in total).

The model predicted eight actual landslide pixels on August 8 and six on August 9 within the 0-0.25 probability range. In the 0.25-0.5 probability range, August 8 assigned 26 landslide pixels and August 9 assigned six. August 8 assigned 39 landslide pixels with a probability between 0.5-0.75, while August 9 assigned 15 within this range. Finally, in the 0.75-1 probability range, August 8 assigned 102 landslide pixels and August 9 assigned 30 landslide pixels.

Table 17: Overview of actual landslide pixels on respective dates from the inventory overlaid on the predicted rasters generated by the Random Forest model for August 8 and 9.

Probability zones	Landslides August 8	Landslides August 9
0 - 0.25	8	1
0.25 - 0.5	26	6
0.5 - 0.75	39	15
0.75 - 1	102	30

6 Discussion

6.1 Forest and terrain influence on landslide initiations

The results indicate that areas with the highest trees per hectare experience the greatest landslide frequency (Figure 13). Furthermore, a leaf coverage of 90-100% is also associated with higher landslide frequencies. This suggests a pattern where denser forests are more prone to landslides, despite the general stabilizing effect of roots on slopes (Section 2.5). Denser forests have more extensive root systems that cross the potential slip surface, thereby increasing stability (Genet, Stokes, Fourcaud et al. 2010). The results could instead possibly be explained by denser forests contributing to a heavier weight on the soil compared to a less dense forest – increasing the driving forces of a possible landslide (Rickli and Graf 2009).

Figure 14a) shows that landslide frequency is highest when the tree height is around 15-25 meters and the tree diameter is between 10-20 cm or 30-40 cm. This indicates quite large trees that weighs more, further enhancing the driving forces behind potential landslides. Ziemer (1981b) argues however that for most mature forests, the weight of the soil overlying a potential failure plane far exceeds the weight of the trees. If weight does become a problem, it is usually in the cohesive soil during heavy rain when the weight of increased soil moisture increases shear stress.

In this study, increased shear stress from the weight of a thick, saturated soil layer is likely not a contributing factor. It is instead presumed that the soil layer where landslides initiated is thin (Hågensen 2023). This was confirmed through site inspections in the field by NGI, and can also be visualized in Figure 25, which is a photo taken from Ottadalen by Anders Kleiven after the storm *Hans*. Additionally, Hågensen (2023) shows that 38 landslides initiated in bedrock (Appendix, Figure 29). Landslides cannot initiate in bedrock due to the absence of soil. Further investigation proved that most of these landslides were in fact located in deciduous forest. Soil is necessary for forest growth. The combination of the field work, NGU classifying forested area as bedrock and that the forest contain deciduous trees with typical shallow roots (Planteportalen n.d.), suggests that the area is covered in a thin soil layer. Root depths in a thin soil layer is generally assumed to be

limited due to the underlying bedrock, not providing further stability (Hasenmueller et al. 2017; Mauer and Palátová 2003).

Figure 25: Picture of a landslide in Ottadalen after *Hans* in August, 2023. The picture is taken by Anders Kleiven, NGI. The thin soil layer on top of bedrock is clearly seen along with quite dense forest in the area.

The immediate risk of shallow landslides depends on how quickly water is supplied and the extent to which the soil is already saturated with water (Crozier 2010; J. Li et al. 2021; NGI 2014). During heavy precipitation events, a thin soil layer on top of an impermeable bedrock cover likely experiences a rapid increase in pore pressures. Furthermore, according to the soil map produced by NGU and the forest resource map (SR16R) produced by NIBIO, bare bedrock is situated higher up, above a lot of the forested areas where landslides initiated. This could contribute to increased flow accumulation into the forests, additionally increasing the pore pressures.

Forests means that there is underground biomass and therefore a presence of root cohesion. Root cohesion enhances the mechanical stabilization of a soil slope, providing

increased resistance against shallow landslides (L. Zhang et al. 2021). The findings from Masi, Tofani et al. (2023), which considers the modelled slope stability effect of plant roots on shallow landslides in Italy, was that root cohesion undoubtedly contributes to higher slope stability. Another finding from Masi, Tofani et al. (2023) however, was that root cohesion had minimal impact particularly when saturated conditions were reached. A storm like *Hans* brought a large amount of precipitation and hence a high soil saturation. The modelled soil saturation reached 110% several places inside the study area (Figure 11 and Appendix, Figure 34a and 35a). That indicates a fully saturated soil, resembling flowing water (Terzaghi et al. 1996). Under such conditions, the stabilizing effect of root cohesion is likely diminished. Also Z. Guo et al. (2023) emphasize that the impact of more intense rainfall is greater than the stabilizing effect of more forests on landslide susceptibility. When rainfall is excessively heavy, the land cover becomes irrelevant because the preventive factors do not have sufficient time to stabilize the slope.

Figure 26 demonstrates the stabilizing influence of forests on slopes. The box plot compares the slope angles where landslides initiated in forested versus non-forested areas. It is observed that slope angles are generally steeper in forested areas than in non-forested areas. This observation aligns with findings from the study by Rickli and Graf (2009), who suggest that the increased slope angles in forested areas are primarily due to soil reinforcement provided by tree roots.

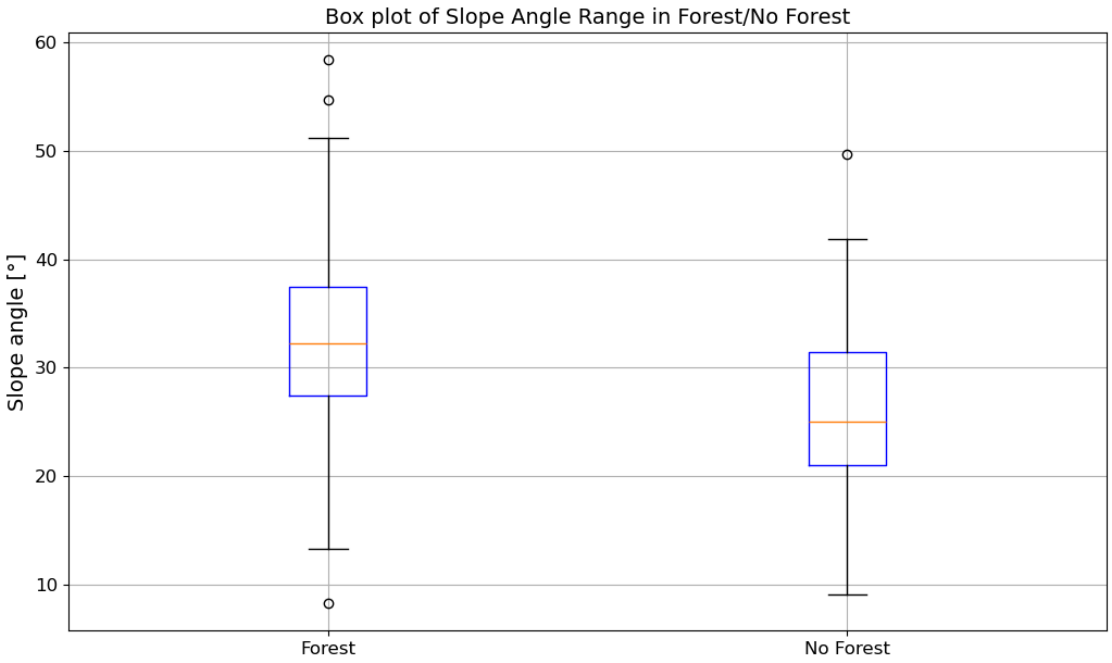

Figure 26: Box plot illustrating the distribution of landslide occurrences based on slope angle, categorized by whether they initiated in forested or non-forested areas. Outliers are represented as dots outside the box, and the orange line indicates the median value.

The initiation of shallow landslides depends on the interactions between soil physical properties, hillslope hydrology, and below-ground ecologic processes (Hwang et al. 2015). The reason for landslide initiation is complex and depend on several different factors. In this case, factors such as a thin soil layer, heavy precipitation increasing pore pressures and reducing root cohesion, additional weight from dense forests and potential increased flow accumulation into forested areas due to overlying bedrock, are all potential factors contributing to the predominance of landslides initiating in forested regions. Despite that forests have been shown to have a stabilizing effect on slopes, this study shows that there are complicating factors where the result is that many shallow landslides happen in densely forested areas.

6.1.1 Birch forests vs. spruce and pine forests

According to Figure 12, most landslides initiated in birch forests compared to non-forested areas and spruce and pine forests. Firstly, a reason could be that the roots of birch devel-

ops long reaching, lateral root systems with age (Mauer and Palátová 2003). Pine, on the other hand, have deep roots if the soil allows for it. Deeper roots anchor through the soil mass into bedrock fractures or more stable soil layers, and contribute with interlocking bindings within weaker soil masses (Ziemer 1981b). Also, the roots produce an apparent cohesion through root fiber reinforcement (Schmidt et al. 2001). This could explain why more landslide initiated in birch forest compared to pine forest. The spruce roots however are also shallow. This means the roots would contribute to slope stability in the same way as birch trees. The total area of spruce is half that of pine and birch trees within the study area. The area covered by spruce, pine and birch forests inside the study area is 157, 399 and 354 square km, respectively. A larger area automatically increase the chance of landslide.

Secondly, unlike spruce and pine trees, which have needles, birch trees bear leaves which make it more susceptible to adverse wind forces. Leaves and a big tree canopy are more easily caught by unfavorable wind forces, possibly moving the tree and exerting shear stress into the soil (Rickli and Graf 2009). During the storm *Hans*, wind speeds reached 15 $\frac{m}{s}$ according to weather stations surrounding the study area (Klimaservicesenter 2023). However, Ziemer (1981b) argues that the shear stress contributed by trees subjected to an 22 $\frac{m}{s}$ wind is not likely to exert a strong influence on slope stability. Despite this, some soil movement due to wind exerting force on the trees is still likely.

Finally, a more speculative argument is proposed. Figure 15 shows the tree height and diameter. The birch trees in the study area have reached their maximum typical size, indicating that this could be an older, mature forest (Grindeland 2023). The pine and spruce on the other hand could reach heights of 40-50 meters, but they only reach 25 meters or below. This could indicate young forests (Aarnes 2014; Sunding et al. 2024). Older trees possess more underground biomass and consequently greater root cohesion (Equation 4, Enquist et al. 2020; Hwang et al. 2015). Thus, landslide probability should decrease with tree age. A possible explanation for more landslides in birch forests could therefore be that older forest contain numerous dead trees. After 15 to 20 years after the tree death, the root system loses most of its soil-stabilizing function because the root strength loss can be assumed proportional to root biomass loss (Ammann et al. 2009; Ziemer 1981a). A healthier tree gives higher tensile strength and therefore a higher contribution from the

roots to the stabilizing of slopes (Ammann et al. 2009; Ziemer 1981a). Dead trees would therefore add weight and contribute with little stabilizing benefit, potentially increasing landslide risk. The amount of dead trees is however unknown.

6.2 Static susceptibility maps

Utilizing ML methods is a growing trend in susceptibility mapping (Ado et al. 2022; Nocentini et al. 2023). Regional landslide susceptibility mapping is a contentious topic due to the ongoing risks it addresses in various regions around the world (Merghadi et al. 2020). ML techniques show significant promise when tackling the challenge of predicting landslides over a large region (Goetz, Brenning et al. 2015). They serve as a good base for mapping large areas that are inaccessible and with limited geological and geotechnical data (Youssef and Pourghasemi 2021). ML models are therefore emerging as cost effective ways to assess landslide susceptibility as an alternative or complementary method to costly and time consuming field mapping.

6.2.1 Model performance

Generally, ensemble algorithms (RF) outperform single-classifier (LR) algorithms (Ado et al. 2022). Based on several studies investigating ML based spatial landslide susceptibility mapping, the AUC of the RF is usually greater than 0.9 while the AUC of the LR is usually greater than 0.8 (Ado et al. 2022; Kavzoglu et al. 2019; Khaliq et al. 2023; Liu et al. 2021; Merghadi et al. 2020; Micheletti et al. 2014; Youssef and Pourghasemi 2021). The RF and LR model obtained an AUC of 0.93 and 0.91 in this study, respectively. An AUC greater than 0.9 indicates excellent model performance, generating highly reliable susceptibility maps (Ado et al. 2022; Çorbacıoğlu and Aksel 2023). Both model performances obtained excellent results (Altexsoft 2022; Bajaj 2023; Barkved 2022), with the RF model doing a bit better than the LR model.

The most important difference in the landslide prediction between the models was in the range of high landslide probability (0.75-1). The LR model predicted around 4% of the study area to be in this category, while the RF model only predicted it for around

1%. Although the difference seems small, a probability range of 0.75-1 suggests a high likelihood of landslides. Relying on the models could necessitate costly preventative measures. This emphasizes the importance of ensuring the model's accuracy for effective prioritization and resource allocation.

Table 12 depicts the distribution of landslide probabilities generated by either the RF or LR model at actual landslide locations. A notable finding from the LR-generated susceptibility map is the high number of landslide pixels (38) having a probability range between 0-0.25. Ideally, an actual landslide should be assigned a probability range of 0.75-1. The RF model demonstrates a better capability in assigning more realistic probabilities to pixels where landslides occurred (12 instead of 38 in the 0-0.25 probability range, and 81 compared to 64 in the probability range 0.75-1). The difference between the two models is likely due to the RF model's ability to capture more complex interactions between input parameters compared to the LR model (Catani et al. 2013; Yao et al. 2023). LR assumes a linear relationship between the input parameters and the log-odds of the outcome, which might not capture the complexity as effectively. Additionally, the feature importance of the *Slope angle* in the LR model is quite high compared to the other parameters, likely resulting in lower probability values for landslides in areas with gentle slopes, even though landslides also occurred there. The table provides an indication of the model performance, further demonstrating the RF models superiority.

It is important to remember that in reality, not one model is correct and several different changes to the process could change the performance (Chowdhury et al. 2024; J. Li et al. 2021; Tehrani et al. 2022). Changes to for instance parameters, model setup, sampling design or pre-processing of data can alter the outcomes (Goetz, Brenning et al. 2015), and care must be taken to assess model performance. The tendency from other studies is to utilize several different models and move on with the model that performs best (Tehrani et al. 2022).

6.2.2 Input parameters

According to Ado et al. (2022), which presents a meta-study that surveys ML models used for landslide susceptibility mapping, commonly used parameters in ML models include

slope degree, slope aspect, curvature, geology, rainfall, distance to rivers, land use land cover, normalized difference vegetation index and distance to roads. The typical amount of input parameters lies between 9-18 parameters (Tehrani et al. 2022). Too many parameters complicates the model and could lead to overfitting (Liu et al. 2021; Micheletti et al. 2014; Zhou et al. 2018). This happens because the model acquires the capacity to fit to a wide variety of data, including the sample noise present in the training data.

This study utilized six parameters for the static approach. An essential part of ML and landslide susceptibility mapping lie in the selection of input data (J. Li et al. 2021; Merghadi et al. 2020). If not all relevant parameters are included, the algorithm identify certain inputs as important without knowing how their significance might change if additional data were included. Parameters that appear crucial could become less significant. One example of this is shown from Table 9, which indicates the feature importance. Landslides occur only within specific slope angles, making this a crucial factor. It is evident that the *Slope angle* is the most critical parameter in both the RF and LR models. However, the feature importance assigned to the slope angle is quite large compared to the other parameters, especially in the LR model. This causes the models to predict a probability of landslides on glaciers, where landslides do not occur. The models currently only differentiate between land covers based on soil and tree type. Incorporating a Land Use and Land Cover (LULC) map could enhance the models' capacity to differentiate between various land use categories, such as urban areas, agricultural zones, and glaciers. This additional parameter might facilitate the identification of areas where landslides are unlikely to occur, such as glaciers (Heggem et al. 2019).

The importance of the soil type feature in both models is interesting. A lot of the landslides in the landslide inventory from this study, and in Norway in general, initiate in valley slopes where the superficial deposits is till (Appendix, Figure 31, NGI 2014). If the soil is till and the slope is greater than 30°, it is an indication that the potential land- or debris flow hazard could be significant (NGI 2014). However, soil type was the least and second least important feature in the RF and LR models, respectively, even though 73% of the landslides in the inventory initiated in either thick or thin till (Appendix, Figure 29). One would expect the model to pick up on this to a larger extent. In the study conducted by Ng et al. (2021), geology performed worst among 15 controlling factors.

They attributed this to the fact that most landslides occurred on geological types that covered large areas, making it difficult to identify specific geological conditions favorable for landslides. Similarly, in this study, thick till covers 1222 km^2 and thin till covers 968 km^2 out of a total of 3071 km^2. This extensive coverage may hinder the model's ability to pinpoint favorable soil types for landslides, as most landslides initiated in till. Also, with the resolution of 1:50,000 in the soil map, the quality could affect model performance.

One solution could be to differentiate the till even further (Ng et al. 2021). Three different tills was distinguished in the area on the basis of textural and structural analyses and an investigation of the till stratigraphy was performed (Bergersen and Garnes 1972; Hole and Bergersen 1981). However, acquiring this detailed information considering the extent of the study area would be extremely time-consuming. It is beyond the scope of this study, but could be an interesting topic for future studies.

6.2.3 Limitations

A notable limitation in this study, which is common for landslide predictions, is imbalance of the datasets. To perform predictions of landslide susceptibility in the study area, the dataset was randomly undersampled from a total of 30 million pixels down to less than 0.1% to prevent excessive computational time. This undersampling involves removing possible critical information regarding the no-landslide pixels. One possible way of minimizing the need for undersampling could be to lower the data resolution. The resolution of the DTM does not necessarily have to be as precise as possible to get the best outcome (Merghadi et al. 2020; Tehrani et al. 2022). A lower resolution would result in less pixels and furthermore less computational demand.

Another way to minimize imbalance of the dataset, which is additionally another significant limitation, is the assumption that the release area of the landslide is only limited to a 10m x 10m area, equivalent to one pixel. Shallow landslides do have a small source area and can be characterized almost as a point (Ruther et al. 2022). However, it must be realized that the release area could be larger or smaller than a 10m x 10m area. If the release area of the landslide is large, it would result in more landslide pixels, increasing the landslide dataset and decreasing the imbalance. Simultaneously, it could complicate

the discrimination process of the models as a larger landslide release area could consist of different types of soil. Previous studies on the same topic use the release area (Liu et al. 2021). The release area information was unfortunately not included in the landslide inventory, only as a combination of release area and run-out area.

Both the ratio $\frac{no-landslide}{landslide}$ and the split ratio between training and testing sets can be sources of error in ML methods. The split ratio 70/30 is used by several studies and have shown good results (Achu et al. 2023; Ado et al. 2022; Liu et al. 2021; Yang et al. 2023). Therefore the use of this split ratio can be supported. However, the $\frac{no-landslide}{landslide}$ ratio is less straightforward. In this study, a ratio of 3:1 was used, although other research has explored various ratios such as 1:1, 2:1, 3:1 and 4:1 (Akinci and Zeybek 2021; Goetz, Brenning et al. 2015; Kavzoglu et al. 2019; Liu et al. 2021; Pourghasemi et al. 2020). The optimal ratio differs between studies since the study areas are different and use different models (Yang et al. 2023). Therefore, it is difficult to obtain the optimal ratio for a specific area from previous studies, and a certain ratio could contribute to inaccuracies (Yang et al. 2023). Deciding on a 3:1 ratio for both RF and LR models was done to be able to compare the models using the same ratio. However, this may bias the results against the LR model, which performed worse than the RF model.

6.3 Dynamic susceptibility maps

In this study, an attempt to integrate dynamic variables such as precipitation and soil saturation into susceptibility modelling is proposed. Since the use of ML-based spatio-temporal landslide susceptibility maps are still in the preliminary phase (Khaliq et al. 2023; Nocentini et al. 2023; Tehrani et al. 2022), comparing the results to other work is difficult. There are, however, studies that apply similar methods as proposed in this study, while other studies use different approaches (Canoglu et al. 2019; J. Li et al. 2021; Ng et al. 2021; Nocentini et al. 2023; Pradhan et al. 2019; Segoni et al. 2018).

6.3.1 Model performance

Considering the performance indicators of the RF model, a slightly lower *precision* is observed when compared to the RF model on static parameters (Table 11 and 16). The *EI* on August 8 is performing better compared to the static approach, but slightly worse again on August 9. The accuracy remains high, and the ROC curve and AUC shows improved results for August 8 and 9 compared to the static ROC curves (Figure 23). AUC values of 0.94 and 0.98 indicates excellent model performance. The discrimination diagram show that the model is good at predicting TN, but not as good at predicting TP. Overall, the model performance is strong.

The generated susceptibility maps highlight the significance of rainfall and soil saturation in the model. Between August 7 and 10, when precipitation amounts were low, the predicted probability of landslides across the study area was also low (Figure 19, 20). This is consistent with observations, as no landslides occurred on these dates. Conversely, on August 8 and 9, the maps show a markedly different scenario. The predicted probability of landslides was much higher and spanned a broader area (Figure 19, 20, 21). The extreme precipitation on these dates corresponded with numerous landslides in the area, and the model's output therefore appears reasonable.

Another interesting feature can be seen by investigating the landslides and corresponding landslide susceptibility map on August 9 (Figure 22). The predicted high-probability landslide areas are primarily located in the southeastern part of the map, which aligns with the region that experienced heavier rainfall (Figure 10). The actual landslide occurrences on August 9 are also concentrated in this area, confirming the alignment between observed and predicted spatial distributions of landslides. The trend is less distinct on August 8 due to a broader spatial distribution of landslides. However, the probability zones are also spread across the study area, indicating a similar trend.

Table 17 depicts the distribution of landslide probabilities generated by the RF model at actual landslide locations for August 8 and 9. In contrast to the static approach (Table 12), where especially the LR model assigned several actual landslides a low probability, the RF model in the dynamic approach provide reasonable probabilities to observed landslides. On August 8, 102 actual landslides were assigned a probability value of 0.75 - 1,

while 30 landslides fell into this range on August 9. Although some landslides received lower probabilities, the numbers were fewer compared to the static approach. This discrepancy could be due to the larger area coverage of higher probabilities for August 8 and 9 compared to the static maps. Additionally, the total amount of landslides are fewer on August 8 and 9 due to the landslide separation based on the landslide initiation dates. However, the results further highlights the high predictive abilities of the RF model.

6.3.2 The role of input parameters

There are several possible dynamic factors that can be considered in a spatio-temporal evaluation (J. Li et al. 2021; Ng et al. 2021; Nocentini et al. 2023; Pradhan et al. 2019; Segoni et al. 2018). For instance, factors such as the 3-hour cumulative rainfall, antecedent rainfall or the sum of cumulative rainfall during a storm or a certain period are all providing information on landslide initiation criteria. The cumulative rainfall would give an indication towards which rainfall thresholds that trigger landslides. An investigation of the 3-hour cumulative rainfall could provide information on what rainfall intensity that affects landslide initiation. The antecedent rainfall provide information on the soil saturation leading up to landslides. For an analysis considering these factors, precise information on the initiation date and time of landslides would be necessary. This information was unavailable for this study. On the other hand, studies that has access to this information showed that either the 2-day cumulative rainfall or the 12-hour rolling (average) rainfall was the most important factor (Ng et al. 2021; Nocentini et al. 2023).

Based on this, the dynamic input of the 24-hour cumulative rainfall and soil saturation used in this study is reasonable. This enhances the model's predictive capabilities regarding landslide probabilities during storm scenarios, where precipitation levels and soil saturation vary. It is important to keep in mind that the extreme event *Hans* is the basis for the model experiments in this study. This corresponds to large rainfall amounts during a short time. It is therefore possible that the model could underestimate the landslide probability of quite large precipitation amounts that are still below *Hans* level, or overestimate landslide probability for precipitation amounts that exceeds *Hans* levels. Training the model on different storm events would provide changing precipitation amounts and soil saturation, making model prediction likely more accurate and realistic. This would, how-

ever, only be relevant for an area with the same local climate as Ottadalen, where precipitation amounts during *Hans* was extreme. It is likely that the model would overestimate landslide probability if applied to western parts of Norway, where average precipitation amounts are considerably higher compared to Ottadalen.

6.3.3 Limitations

Although the results are promising, there are some important considerations to note. One is for instance the 1km x 1km grid size of the precipitation and soil saturation data, which is significantly larger than the other data resolutions (Table 3). When this data is resampled to 10m x 10m, many smaller pixels within the larger grid retain similar values, creating large areas of uniform data. Due to the high feature importance of rainfall and soil saturation, the 1km x 1km squares are visible in the maps as quite distinct breaks or lines. This does not accurately represent real-life conditions, introducing a degree of inaccuracy in the maps.

Also, the ratio $\frac{no-landslide}{landslide}$ for the dynamic approach was specifically important. Based on the inputs, the ML model learns a "rule" that produces the desired outcome (Tehrani et al. 2022). If the ratio was too small, precipitation would exhibit a disproportionately large feature importance compared to the other parameters, even the slope angle. This resulted in flat areas with no inclination being assigned a high landslide probability, which is illogical and not realistic. Changing the ratio allowed for the feature importance of different parameters to be adjusted and determined by the user. In essence, the user could alter the "rules" learned by the algorithm. This emphasizes the structure of a supervised ML model where the inputs and model configuration is important. If the user is inexperienced, this could lead to inaccurate landslide susceptibility maps.

Information on exact landslide initiation time and date is essential to associate each landslide to the respective triggering rainfall (Nocentini et al. 2023). The exact time and date information was not provided for the majority of the landslides in this study. The assumption that landslides initiated during the most intense rainfall aligns with theoretical expectations, but it may not always be accurate or representative of real-life scenarios. Acquiring this information for a large amount of landslides is however difficult, as land-

slides are usually not observed as they happen, storms and heavy rainfall usually bring clouds which makes it hard for determining exact timing of landslides with satellites, and considering the wide spatial distribution of (perhaps small) landslides over large areas (Abanco et al. 2021; Rüther et al. 2024). Developing methods to acquire landslide inventory data fast and gaining information about the timing of landslides is of crucial interest in further spatio-temporal landslide susceptibility mapping. This is, again, beyond the scope of this study. However, satellite images, other aerial images, citizen science, field work, reports from locals, newspapers or in NVE database, or Copernicus rapid mapping commissioned by NVE could provide insights into developing such methods (Rüther et al. 2024).

6.4 Future studies

6.4.1 Future research with significant resources

In a research project with comprehensive funding the following ideas are proposed. The ML models in this study produce quite accurate but probably site-specific susceptibility maps, which are likely to be inaccurate when predicting landslides in different geographical areas. This is an important but often neglected aspect of ML modelling – how the model performs in areas beyond the training area (D. Sun et al. 2020; Tehrani et al. 2022). Many studies, including this one, evaluate the performance indicators of the models in the same area to determine whether the model prediction was a success or not. Developing a well-performing, generalized model across different geographical areas can be challenging due to significant variations in input parameters, which increases complexity and the risk of overfitting. D. Sun et al. (2020) investigates how two supervised model performs on new, unseen area, but for two quite similar areas with respect to input parameters. The model showed good generalizing abilities. A well-performing, generalized model would offer uniform evaluation across areas and optimize resource allocation, reducing the workload and efficiency in practice (D. Sun et al. 2020).

Tehrani et al. (2022) express skepticism about the immediate development of such generalized (almost global coverage) models. However, they emphasize the potential in for instance integrating ML methods with physically-based models, into a hybrid physics-ML

model. Perhaps also supervised models in combination with unsupervised, deep learning, statistical methods or other hybrid methods offers possibilities regarding good generalizing models.

Unsupervised learning methods have been applied less frequently than supervised methods and the unlabeled datasets makes the unsupervised ML methods less popular (Tehrani et al. 2022). Chang et al. (2020) compares two supervised and two unsupervised models, finding that the supervised models perform better, suggesting a potential limitation in the effectiveness of unsupervised methods for this application.

Deep learning models (a sub-set of ML), on the other hand, have shown promising results and often outperform some supervised models (Azarafza et al. 2021; Habumugisha et al. 2022; Mondini et al. 2023; Ngo et al. 2021; Wang, Fang et al. 2019; T. Zhang et al. 2022). Also hybrid methods, which combine different models, generally perform better than standalone models (Ado et al. 2022; X. Chen and W. Chen 2021; Fang et al. 2020; Lv et al. 2022; Mavaie et al. 2023; Nguyen et al. 2019; Su et al. 2023). These models, in combination with physically-based models and heuristic approaches, might provide valuable insights and could be worth exploring further to gain a more robust and generalized assessment of regional landslide susceptibility. The potential of gaining a well generalized model is undoubtedly evident and could enhance the effectiveness and precision of regional landslide susceptibility mapping. The growing interest in tackling these challenges highlights the potential for wider practical application (Tehrani et al. 2022).

6.4.2 Future research (master theses) with limited resources

The above proposed future research requires extensive resources (computing and field work costs) and time, making it challenging for master's students. Instead, students could explore testing deep-learning or hybrid methods – experimenting with several and continuing with the best-performing model – within the study area described in this thesis or in other areas with extensive landslide inventories. They should use both new and perhaps some existing input parameters as used in this study, but also attempt to implement the different types of landslides that occur in the respective areas. This study was not able to implement the different types of landslides, and evaluated every landslide as

the same. For a well-performing generalization model that can distinguish between different geographical areas, the ability to differentiate between types of landslides are of high importance. The differentiation enhances resource allocation and addresses the fact that different types of landslides occur throughout Norway (NVE 2023a). Taalab et al. (2018) attempted this, and the results show that there is significant scope to develop a joint classification-susceptibility model.

Here follows some proposed questions for future studies, that could aid in the generalization process of models:

Are models able to predict not only landslide susceptibility, but also what types of landslides that might occur? Is, for instance, the landslide susceptibility predicted by ML models different in the three till-layers mentioned earlier (Section 3)?

How can we quickly and precisely gather a landslide inventory, which includes information on release areas and the date and time of landslides, to utilize it in a spatio-temporal landslide investigation?

7 Conclusion

Norway is expected to experience more intense precipitation and higher temperatures in a changing climate. *Hans* could thus be considered a "normal" storm in future scenarios, but is such weather even "normal" today? The year 2023 was the most expensive year concerning weather and natural disaster damages so far, reaching 7.4 billion Norwegian Kroner in total (Ruth 2024). The costs related to increased landslide activity in the future is also expected to rise.

This study have investigated different forest parameters to gain a deeper understanding of the forest's role in landslide triggering. Additionally, two different machine learning (ML) models, Logistic Regression (LR) and Random Forest (RF), was utilized to explore the predictive abilities regarding landslides and to allow for a comparison between the two models. The implementation of dynamic parameters such as rainfall and soil saturation in the RF algorithm was additionally carried out, providing a proposed method of generating spatio-temporal landslide susceptibility maps. Based on this study an attempt to answer the research questions are as follows.

- **Is it possible to identify whether certain forests or forest parameters are common for landslide triggering?**

  It is widely known (or perhaps assumed) that trees and roots contribute to the slope stability by reducing the amount of water in the soil and providing additional lateral reinforcement. In this study it is shown that landslide frequency was higher in areas where the forest was larger, thicker and denser. The predominance of landslides initiating in forested regions is most likely because of the additional weight from the forests in combination with a commonly thin soil layer, and high pore pressures during the extreme weather event *Hans*.

  The fact that the birch forest covers a relatively large area, grows shallow roots, has leaves, and is potentially older and therefore containing dead trees, could be reasons for more landslides initiating in this type of forest compared to spruce and pine forests. There are however a lot of uncertainty, and further investigation/field work needs to be conducted to conclude on this.

- **Can machine learning models create efficient, spatio-temporal landslide susceptibility maps?**

  The models in this study show promising results with respect to performance and could therefore be suitable to predict the spatio-temporal distribution of landslides over a large area. On the other hand, several factors necessitate caution when interpreting the results of this study. These include (i) data quality and resolution, (ii) the use of single pixels instead of the actual release areas, (iii) the choice of input parameters, models and ratios as they always vary differently, (iv) the influence of user decisions on feature importance in the models, and (v) the insufficient data on the timing of landslide initiation. It is essential to consider these factors when interpreting the generated spatial and spatio-temporal susceptibility maps.

- **Can machine learning models be utilized for other areas or storm events in Norway to predict landslides?**

  The input parameters in this study are highly site-specific. For areas characterized by the same type of climate, geology and vegetation as the study area, the models could likely generate susceptibility maps for a large region. In a different region, such as the western part of Norway, it is probable that the models would not generate accurate maps. This discrepancy arises from variations in geographical features and corresponding input parameters. If the model was presented to other storm events, it might overestimate or underestimate the probability zoning if the rainfall significantly exceeds or falls short of the levels experienced during the *Hans* storm.

Overall, the most important results of this study are that forest characteristics play an important role in landslide susceptibility. Moreover, ML models are useful tools for creating site-specific and storm-specific susceptibility maps over a large region. They are therefore capable of producing a guide for general planning and assessment purposes. Future work should continue to focus on the potential of utilizing hybrid methods based on supervised, deep-learning, physically-based, heuristic or other statistical methods. Such models potentially offer new possibilities for data management and analysis that could play a crucial role in future landslide susceptibility mapping.

Bibliography

Aarnes, H. (2014). *Gran*. Accessed on 25.05.2024. URL: https://www.mn.uio.no/ibv/tjenester/kunnskap/plantefys/botanikk/gran.html.

Abanco, C. et al. (2021). 'The role of geomorphology, rainfall and soil moisture in the occurrence of landslides triggered by 2018 Typhoon Mangkhut in the Philippines'. In: *Natural Hazards and Earth System Sciences* 21.5, pp. 1531–1550. DOI: 10.5194/nhess-21-1531-2021.

Achu, A. L. et al. (2023). 'Machine-learning based landslide susceptibility modelling with emphasis on uncertainty analysis'. In: *Geoscience Frontiers* 14.6, p. 101657.

Ado, M. et al. (2022). 'Landslide susceptibility mapping using machine learning: A literature survey'. In: *Remote Sensing* 14.13, p. 3029.

Akinci, H. and Zeybek, M. (2021). 'Comparing classical statistic and machine learning models in landslide susceptibility mapping in Ardanuc (Artvin), Turkey'. In: *Natural Hazards* 108.2, pp. 1515–1543.

Altexsoft (2022). *Machine Learning Metrics: How to Measure the Performance of a Machine Learning Model*. Accessed on 25.04.2024. URL: https://www.altexsoft.com/blog/machine-learning-metrics/.

Amazon (2024). *Cross-Validation*. Accessed on 28.05.2024. URL: https://docs.aws.amazon.com/machine-learning/latest/dg/cross-validation.html.

— (n.d.[a]). *What is Hyperparameter Tuning?* Accessed on 11.03.2024. URL: https://aws.amazon.com/what-is/hyperparameter-tuning/.

— (n.d.[b]). *What is Overfitting?* Accessed on 11.03.2024. URL: https://aws.amazon.com/what-is/overfitting/.

Ammann, M. et al. (2009). 'Significance of tree root decomposition for shallow landslides'. In: *For Snow Landsc Res* 82.79-94, p. 79.

Andreassen, H. (2023). *Hvorfor var «Hans» annerledes?* Accessed on 13.11.2023. URL: https://cicero.oslo.no/no/artikler/hvorfor-var-hans-annerledes.

ArcGISPro (n.d.[a]). *How Aspect works*. Accessed on 30.11.2023. URL: https://pro.arcgis.com/en/pro-app/latest/tool-reference/spatial-analyst/how-aspect-works.htm.

ArcGISPro (n.d.[b]). *How Fill works*. Accessed on 15.05.2024. URL: https://pro.arcgis.com/en/pro-app/latest/tool-reference/spatial-analyst/how-fill-works.htm.

— (n.d.[c]). *How Flow Accumulation works*. Accessed on 13.02.24. URL: https://pro.arcgis.com/en/pro-app/latest/tool-reference/spatial-analyst/how-flow-accumulation-works.htm.

— (n.d.[d]). *How Flow Direction works*. Accessed on 13.02.24. URL: https://pro.arcgis.com/en/pro-app/latest/tool-reference/spatial-analyst/how-flow-direction-works.htm.

— (n.d.[e]). *Introducing ArcGIS Pro*. Accessed on 05.03.2024. URL: https://pro.arcgis.com/en/pro-app/latest/get-started/introducing-arcgis-pro.htm.

— (n.d.[f]). *Introduction to ArcGIS Pro*. Accessed on 05.03.2024. URL: https://pro.arcgis.com/en/pro-app/latest/get-started/get-started.htm.

— (n.d.[g]). *Resample (Data Management)*. Accessed on 15.05.2024. URL: https://pro.arcgis.com/en/pro-app/3.1/tool-reference/data-management/resample.htm.

— (n.d.[h]). *Slope function*. Accessed on 15.09.2023. URL: https://pro.arcgis.com/en/pro-app/latest/help/analysis/raster-functions/slope-function.htm.

Azarafza, M. et al. (2021). 'Deep learning-based landslide susceptibility mapping'. In: *Scientific reports* 11.1, p. 24112.

Bækkelund, B. (2024). *brysthøyde*. Accessed on 28.05.2024. URL: https://snl.no/brysth%C3%B8yde.

Bajaj, A. (2023). *Performance Metrics in Machine Learning (Complete Guide)*. Accessed on 25.04.2024. URL: https://neptune.ai/blog/performance-metrics-in-machine-learning-complete-guide.

Baltensweiler, A. et al. (2017). 'Terrestrial laser scanning improves digital elevation models and topsoil pH modelling in regions with complex topography and dense vegetation'. In: *Environmental Modelling and Software* 95, pp. 13–21. DOI: https://doi.org/10.1016/j.envsoft.2017.05.009.

Barcelos, G. (2022). *Understanding Bias in Machine Learning Models*. Accessed on 26.02.2024. URL: https://arize.com/blog/understanding-bias-in-ml-models/.

Barkved, K. (2022). *How To Know if Your Machine Learning Model Has Good Performance*. Accessed on 25.04.2024. URL: https://www.obviously.ai/post/machine-learning-model-performance.

Beldring, S. et al. (2003). 'Estimation of parameters in a distributed precipitation-runoff model for Norway'. In: *Hydrology and Earth System Sciences* 7.3, pp. 304–316.

Bergersen, O. F. and Garnes, K. (1972). 'Ice movements and till stratigraphy in the Gudbrandsdal area. Preliminary results'. In.

Bischetti, G. B. et al. (2007). 'Root strength and root area ratio of forest species in Lombardy (Northern Italy)'. In: *Eco-and Ground Bio-Engineering: The Use of Vegetation to Improve Slope Stability: Proceedings of the First International Conference on Eco-Engineering 13–17 September 2004*. Springer, pp. 31–41.

Bogaard, T. and Greco, R. (2016). 'Landslide hydrology: from hydrology to pore pressure'. In: *WIREs Water* 3, pp. 439–459. DOI: 10.1002/wat2.1126.

Boje, S., Beldring, S. and Engeset, R. (2018). *Hvordan lages vær- og vanndata for seNorge.no og xGeo.no?* https://www.nve.no/media/7502/waterdata_v2_no.pdf. [PDF].

Breiman, L. (2001). 'Random forests'. In: *Machine learning* 45, pp. 5–32.

Brooks-Bartlett, J. (2018). *Probability concepts explained: Maximum likelihood estimation*. Accessed on 15.03.2024. URL: https://towardsdatascience.com/probability-concepts-explained-maximum-likelihood-estimation-c7b4342fdbb1.

Brown, S. (2021). *Machine learning, explained*. Accessed on 15.04.2024. URL: https://mitsloan.mit.edu/ideas-made-to-matter/machine-learning-explained.

Brownlee, J. (2021a). *SMOTE for Imbalanced Classification with Python*. Accessed on 26.02.2024. URL: https://machinelearningmastery.com/smote-oversampling-for-imbalanced-classification/.

— (2021b). *Undersampling Algorithms for Imbalanced Classification*. Accessed on 26.02.2024. URL: https://machinelearningmastery.com/undersampling-algorithms-for-imbalanced-classification/.

Bryhni, I. and Fossen, H. (2023). *Den kaledonske fjellkjeden*. Accessed on 28.05.2024. URL: https://snl.no/Den_kaledonske_fjellkjeden.

Budimir, M. E. A., Atkinson, P. M. and Lewis, H. G. (2015). 'A systematic review of landslide probability mapping using logistic regression'. In: *Landslides* 12, pp. 419–436.

Bugge, S. and Borgmo, J. (2023). *Jernbanebroen over Lågen ved Ringebu har kollapset*. Accessed on 10.11.2023. URL: https://www.vg.no/nyheter/innenriks/i/abBgEO/jernbanebroen-over-laagen-ved-ringebu-har-rast-i-elven.

Canoglu, M. C., Aksoy, H. and Ercanoglu, M. (2019). 'Integrated approach for determining spatio-temporal variations in the hydrodynamic factors as a contributing parameter in landslide susceptibility assessments'. In: *Bulletin of Engineering Geology and the Environment* 78, pp. 3159–3174.

Capobianco, V. et al. (2024). 'A method to derive spatially variable root cohesion maps from underground biomass maps for regional landslide susceptibility models'. In: *Proceedings of the EGU General Assembly 2024*. Vol. EGU24-15976. Vienna, Austria. DOI: 10.5194/egusphere-egu24-15976. URL: https://doi.org/10.5194/egusphere-egu24-15976.

Catani, F. et al. (2013). 'Landslide susceptibility estimation by random forests technique: sensitivity and scaling issues'. In: *Natural Hazards and Earth System Sciences* 13.11, pp. 2815–2831.

CAWCR (2015). *Forecast Verification*. Accessed on 14.05.2024. URL: https://www.cawcr.gov.au/projects/verification/.

Chang, Z. et al. (2020). 'Landslide susceptibility prediction based on remote sensing images and GIS: Comparisons of supervised and unsupervised machine learning models'. In: *Remote Sensing* 12.3, p. 502.

Chawla, N. V. et al. (2002). 'SMOTE: synthetic minority over-sampling technique'. In: *Journal of artificial intelligence research* 16, pp. 321–357.

Chen, W., Sun, Z. and Han, J. (2019). 'Landslide susceptibility modeling using integrated ensemble weights of evidence with logistic regression and random forest models'. In: *Applied sciences* 9.1, p. 171.

Chen, W., Xie, X. et al. (2017). 'A comparative study of logistic model tree, random forest, and classification and regression tree models for spatial prediction of landslide susceptibility'. In: *Catena* 151, pp. 147–160.

Chen, X. and Chen, W. (2021). 'GIS-based landslide susceptibility assessment using optimized hybrid machine learning methods'. In: *Catena* 196, p. 104833.

Chowdhury, M. S. et al. (2024). 'GIS-based landslide susceptibility mapping using logistic regression, random forest and decision and regression tree models in Chattogram District, Bangladesh'. In: *Heliyon* 10.1.

Christensen, A. (2012). *Tørr i toppen, syk i kroppen*. Accessed on 15.04.2024. URL: https://www.forskning.no/skog-skogbruk/torr-i-toppen-syk-i-kroppen/700747.

Cohen, D. and Schwarz, M. (2017). 'Tree-root control of shallow landslides'. In: *Earth Surface Dynamics* 5.3, pp. 451–477.

Çorbacıoğlu, Ş. K. and Aksel, G. (2023). 'Receiver operating characteristic curve analysis in diagnostic accuracy studies: A guide to interpreting the area under the curve value'. In: *Turkish Journal of Emergency Medicine* 23.4, p. 195.

Crosta, G.B. and Frattini, P. (2003). 'Distributed modelling of shallow landslides triggered by intense rainfall'. In: *Natural Hazards and Earth System Sciences* 3.1/2, pp. 81–93.

Crozier, M.J. (2005). 'Multiple-occurrence regional landslide events in New Zealand: Hazard management issues'. In: *Landslides* 2, pp. 247–256. DOI: https://doi.org/10.1007/s10346-005-0019-7.

— (2010). 'Deciphering the effect of climate change on landslide activity: A review'. In: *Geomorphology* 124, pp. 260–267. DOI: https://doi.org/10.1016/j.geomorph.2010.04.009.

Cruden, D.M. and Varnes, D. J. (1996). 'Landslide types and processes'. In: *Transportation research board, US National Academy of Sciences* 247, pp. 36–75.

Dai, F.C., Lee, C.F. and Ngai, Y.Y. (2002). 'Landslide risk assessment and management: an overview'. In: *Engineering geology* 64.1, pp. 65–87.

Dalen, L. S. (2022). *Trærnes ti på topp i Norge*. Accessed on 28.05.2024. URL: https://www.nibio.no/nyheter/traernes-ti-pa-topp-i-norge.

Dannevig, P. and Harstveit, K. (2022). *klima i Norge*. Accessed on 06.12.2023. URL: https://snl.no/klima_i_Norge.

Dorren, L. and Schwarz, M. (2016). 'Quantifying the stabilizing effect of forests on shallow landslide-prone slopes'. In: *Ecosystem-Based Disaster Risk Reduction and Adaptation in Practice*, pp. 255–270.

Ekroll, H. (2023). *Ekstremværet Hans vil trolig koste langt mer enn storflommen i 1995*. Accessed on 10.11.2023. URL: https://www.aftenposten.no/norge/i/76w3oW/ekstremvaeret-hans-vil-trolig-koste-langt-mer-enn-storflommen-i-1995.

El Naqa, I. and Murphy, M. J. (2015). *What is machine learning?* Springer.

Emdal, A. (2022). *Introduksjon til Geoteknikk*. NTNU.

Enquist, B. J. et al. (2020). 'The megabiota are disproportionately important for biosphere functioning'. In: *Nature communications* 11.1, p. 699.

Esri (n.d.). *What is GIS?* Accessed on 28.05.2024. URL: https://www.esri.com/en-us/what-is-gis/overview.

Fang, Z. et al. (2020). 'Integration of convolutional neural network and conventional machine learning classifiers for landslide susceptibility mapping'. In: *Computers & Geosciences* 139, p. 104470.

Fell, R. et al. (2008). 'Guidelines for landslide susceptibility, hazard and risk zoning for land use planning'. In: *Engineering Geology* 8, pp. 85–98. DOI: https://doi.org/10.1016/j.enggeo.2008.03.022.

Feurer, M. and Hutter, F. (2019). 'Hyperparameter optimization'. In: *Automated machine learning: Methods, systems, challenges*, pp. 3–33.

Filho, M. (2023). *How To Get Feature Importance In Logistic Regression*. Accessed on 15.03.2024. URL: https://forecastegy.com/posts/feature-importance-in-logistic-regression/.

Fischer, C., Vestøl, G. I. and Høibø, O. (2016). 'Modelling the variability of density and bending properties of Norway spruce structural timber'. In: *Canadian Journal of Forest Research* 46.7, pp. 978–985.

Fossen, H. (2023a). *Den kaledonske orogenese*. Accessed on 28.05.2024. URL: https://snl.no/Den_kaledonske_orogenese.

— (2023b). *fjellkjededannelse*. Accessed on 28.05.2024. URL: https://snl.no/fjellkjededannelse.

Gariano, S. L. and Guzzetti, F. (2016). 'Landslides in a changing climate'. In: *Earth-Science Reviews* 162, pp. 227–252. DOI: https://doi.org/10.1016/j.earscirev.2016.08.011.

Ge, Q. et al. (2024). 'A comparative evaluation of clustering methods and data sampling techniques in the prediction of reservoir landslide deformation state'. In: *Georisk: Assessment and Management of Risk for Engineered Systems and Geohazards*, pp. 1–17.

GeeksforGeeks (2023). *Cross Validation in Machine Learning*. Accessed on 13.03.2024. URL: https://www.geeksforgeeks.org/cross-validation-machine-learning/.

GeeksforGeeks (2024a). *Feature Importance with Random Forests*. Accessed on 31.05.2024. URL: https://www.geeksforgeeks.org/feature-importance-with-random-forests/.

— (2024b). *ML-Underfitting and Overfitting*. Accessed on 15.04.2024. URL: https://www.geeksforgeeks.org/underfitting-and-overfitting-in-machine-learning/.

Genet, M., Stokes, A., Fourcaud, T. et al. (2010). 'The influence of plant diversity on slope stability in a moist evergreen deciduous forest'. In: *Ecological engineering* 36.3, pp. 265–275.

Genet, M., Stokes, A., Salin, F. et al. (2005). 'The influence of cellulose content on tensile strength in tree roots'. In: *Plant and soil* 278, pp. 1–9.

Goetz, J. N., Brenning, A. et al. (2015). 'Evaluating machine learning and statistical prediction techniques for landslide susceptibility modeling'. In: *Computers and geosciences* 81, pp. 1–11.

Goetz, J. N., Guthrie, R. H. and Brenning, A. (2011). 'Integrating physical and empirical landslide susceptibility models using generalized additive models'. In: *Geomorphology* 129.3-4, pp. 376–386.

Granerød, M. et al. (2023). *Ekstremværet "Hans", ekstremt mye nedbør i deler av Sør-Norge 07.-09. august 2023*. Hendelsesrapport 26. Meteorologisk institutt. URL: https://www.met.no/publikasjoner/met-info/ekstremvaer/_/attachment/inline/c91bde7d-a0a9-4275-a644-5f9470bc27ad:54006df697897306e1b81ead80d74484daa6717e/MET-info-26-2023.pdf.

Grindeland, J. M. (2023). *bjørk (art)*. Accessed on 25.05.2024. URL: https://snl.no/bj%C3%B8rk_-_art.

Grindeland, J. M. and Larsen, Ø. S. (2024). *bjørk*. Accessed on 15.03.2024. URL: https://snl.no/bj%C3%B8rk.

Guo, D. et al. (2014). 'An empirical model for landslide travel distance prediction in Wenchuan earthquake area'. In: *Landslides* 11, pp. 281–291.

Guo, Z. et al. (2023). 'Shallow landslide susceptibility assessment under future climate and land cover changes: A case study from southwest China'. In: *Geoscience Frontiers* 14. DOI: https://doi.org/10.1016/j.gsf.2023.101542.

Gupta, P. (2017). *Cross-Validation in Machine Learning*. Accessed on 28.05.2024. URL: https://towardsdatascience.com/cross-validation-in-machine-learning-72924a69872f.

Guzzetti, F. et al. (2006). 'Estimating the quality of landslide susceptibility models'. In: *Geomorphology* 81.10, pp. 166–184. DOI: https://doi.org/10.1016/j.geomorph.2006.04.007.

Habumugisha, J. M. et al. (2022). 'Landslide susceptibility mapping with deep learning algorithms'. In: *Sustainability* 14.3, p. 1734.

Hågensen, I. (2023). *Assessment of Landslide Initiation in Ottadalen, Norway Following the Storm «Hans»*.

Hales, T. C. (2018). 'Modelling biome-scale root reinforcement and slope stability'. In: *Earth Surface Processes and Landforms* 43.10, pp. 2157–2166.

Hanssen-Bauer, I. et al. (2015). *Klima i Norge 2100*. Tech. rep. 2. NCCS. URL: https://www.miljodirektoratet.no/globalassets/publikasjoner/m406/m406.pdf.

Hasenmueller, E. A. et al. (2017). 'Weathering of rock to regolith: The activity of deep roots in bedrock fractures'. In: *Geoderma* 300, pp. 11–31.

Heggem, E. S. F., Mathisen, H. and Frydelund, J. (2019). *AR50 – Arealressurskart i målestokk 1:50 000*. Beskrivelse 118. NIBIO. URL: http://hdl.handle.net/11250/2626573.

Highland, L. M. and Bobrowsky, P. (2008). *The landslide handbook-A guide to understanding landslides*. 1325. US Geological Survey.

Hole, J. and Bergersen, O. F. (1981). 'Weichselian till stratigraphy and ice movements in Ottadalen, central south Norway'. In.

Hoo, Z. H., Candlish, J. and Teare, D. (2017). *What is an ROC curve?*

Huang, F. et al. (2022). 'Regional rainfall-induced landslide hazard warning based on landslide susceptibility mapping and a critical rainfall threshold'. In: *Geomorphology* 408, p. 108236.

Hungr, O., Leroueil, S. and Picarelli, L. (2013). 'The Varnes classification of landslide types, an update'. In: *Landslides* 11, pp. 167–194. DOI: 10.1007/s10346-013-0436-y.

Hussain, M. A. et al. (2022). 'Landslide susceptibility mapping using machine learning algorithm'. In: *Civ. Eng. J* 8, pp. 209–224.

Hwang, T. et al. (2015). 'Simulating vegetation controls on hurricane-induced shallow landslides with a distributed ecohydrological model'. In: *Journal of Geophysical Research: Biogeosciences* 120.2, pp. 361–378.

Ilinca, V. (2021). 'Using morphometrics to distinguish between debris flow, debris flood and flood (Southern Carpathians, Romania)'. In: *Catena* 197, p. 104982.

Iverson, M. R. (2000). 'Landslide triggering by rain infiltration'. In: *Water Resources Research* 36.7, pp. 1897–1910. DOI: https://doi.org/10.1029/2000WR900090.

Jaedicke, C. et al. (2014). 'Identification of landslide hazard and risk 'hotspots' in Europe'. In: *Bull Eng Geol Environ* 73, pp. 325–339. DOI: https://doi.org/10.1007/s10064-013-0541-0.

Jordan, M. I. and Mitchell, T. M. (2015). 'Machine learning: Trends, perspectives, and prospects'. In: *Science* 349.6245, pp. 255–260.

Kartverket (2023a). *Høgdedata og djupnedata*. Accessed on 05.12.2023. URL: https://www.kartverket.no/api-og-data/terrengdata.

— (2023b). *Nasjonal Høydemodell*. Accessed on 15.09.2023. URL: https://hoydedata.no/LaserInnsyn2/.

Kavzoglu, T., Sahin, E. K. and Colkesen, I. (2015). 'Selecting optimal conditioning factors in shallow translational landslide susceptibility mapping using genetic algorithm'. In: *Engineering Geology* 192, pp. 101–112.

— (2019). 'Machine learning techniques in landslide susceptibility mapping: a survey and a case study'. In: *Landslides: Theory, practice and modelling*, pp. 283–301.

Khaliq, A. H. et al. (2023). 'Spatiotemporal landslide susceptibility mapping using machine learning models: A case study from district Hattian Bala, NW Himalaya, Pakistan'. In: *Ain Shams Engineering Journal* 14.3, p. 101907.

Kildahl, K. (2020). *Nine facts about Norwegian agriculture*. Accessed on 6.06.2024. URL: https://www.nibio.no/en/news/nine-facts-about-norwegian-agriculture.

Kleiven, A. (2022). 'Utløsning av jord- og flomskred - Hvordan skråningens orientering påvirker utløsning av jord- og flomskred i Ottadalen'. MA thesis. NTNU.

Klimaservicesenter (2023). *Observasjoner og værstatistikk*. Accessed on 13.10.2023. URL: https://seklima.met.no/observations/.

Korup, O. and Stolle, A. (2014). 'Landslide prediction from machine learning'. In: *Geology today* 30.1, pp. 26–33.

Kristensen, L. L. et al. (2015). 'Terminologi for naturfare'. In.

Larsson, J. Y. (2024). *lauvskog*. Accessed on 26.02.2024. URL: https://snl.no/lauvskog.

Lasberg, K. (May 2014). 'Chronology of the Weichselian Glaciation in the southeastern sector of the Scandinavian Ice Sheet.' PhD thesis.

Li, J. et al. (2021). 'Spatiotemporal landslide susceptibility mapping incorporating the effects of heavy rainfall: a case study of the heavy rainfall in August 2021 in Kitakyushu, Fukuoka, Japan'. In: *Water* 13.22, p. 3312.

Li, Y. and Mo, P. (2019). 'A unified landslide classification system for loess slopes: A critical review'. In: *Geomorphology* 340, pp. 67–83.

Lindsay, E. et al. (2022). 'Multi-Temporal Satellite Image Composites in Google Earth Engine for Improved Landslide Visibility: A Case Study of a Glacial Landscape'. In: *Remote Sensing* 14.10. DOI: https://www.mdpi.com/2072-4292/14/10/2301.

Liu, Z. et al. (2021). 'Modelling of shallow landslides with machine learning algorithms'. In: *Geoscience Frontiers* 12.1, pp. 385–393.

Lundqvist, J. (1986). 'Late Weichselian glaciation and deglaciation in Scandinavia'. In: *Quaternary Science Reviews* 5, pp. 269–292.

Lussana, C. (2023). *seNorge, RR: daily total precipitation amounts over Norway*. Accessed on 25.03.2024. URL: https://zenodo.org/records/8254460.

Lussana, C. et al. (2019). 'seNorge2018, daily precipitation, and temperature datasets over Norway'. In: *Earth Syst. Sci. Data* 11, pp. 1531–1551. DOI: https://doi.org/10.5194/essd-11-1531-2019.

Lv, L. et al. (2022). 'A hybrid ensemble-based deep-learning framework for landslide susceptibility mapping'. In: *International Journal of Applied Earth Observation and Geoinformation* 108, p. 102713.

Ma, Z., Mei, G. and Piccialli, F. (2021). 'Machine learning for landslides prevention: a survey'. In: *Neural Computing and Applications* 33, pp. 10881–10907.

Mæhlum, L. (2023). *Innlandets geologi*. Accessed on 27.09.2023. URL: https://snl.no/Innlandets_geologi.

Mao, Z. et al. (2012). 'Engineering ecological protection against landslides in diverse mountain forests: choosing cohesion models'. In: *Ecological Engineering* 45, pp. 55–69.

Masi, E. B., Segoni, S. and Tofani, V. (2021). 'Root reinforcement in slope stability models: a review'. In: *Geosciences* 11.5, p. 212.

Masi, E. B., Tofani, V. et al. (2023). 'Effects of roots cohesion on regional distributed slope stability modelling'. In: *Catena* 222, p. 106853.

MathWorks (n.d.). *Compare Deep Learning Models Using ROC Curves*. Accessed on 15.04.2024. URL: https://www.mathworks.com/help/deeplearning/ug/compare-deep-learning-models-using-ROC-curves.html.

Mattia, C., Bischetti, G. B. and Gentile, F. (2005). 'Biotechnical characteristics of root systems of typical Mediterranean species'. In: *Plant and soil* 278, pp. 23–32.

Mauer, O. and Palátová, E. (2003). 'The role of root system in silver birch (Betula pendula Roth) dieback in the air-polluted area of Krušné hory Mts'. In: *J. For. Sci* 49.5, pp. 191–199.

Mavaie, P., Holder, L. and Skinner, M. K. (2023). 'Hybrid deep learning approach to improve classification of low-volume high-dimensional data'. In: *BMC bioinformatics* 24.1, p. 419.

Medina, V. et al. (2021). 'Fast physically-based model for rainfall-induced landslide susceptibility assessment at regional scale'. In: *CATENA* 201. DOI: https://doi.org/10.1016/j.catena.2021.105213.

Melchiorre, C. and Frattini, P. (2012). 'Modelling probability of rainfall-induced shallow landslides in a changing climate, Otta, Central Norway'. In: *Climatic Change* 113, pp. 413–436. DOI: https://doi.org/10.1007/s10584-011-0325-0.

Merghadi, A. et al. (2020). 'Machine learning methods for landslide susceptibility studies: A comparative overview of algorithm performance'. In: *Earth-Science Reviews* 207, p. 103225.

METNorway (2017). *Data og produkter fra MET*. Accessed on 17.09.2023. URL: https://www.met.no/frie-meteorologiske-data/frie-meteorologiske-data.

— (2023). *Dataset*. Accessed on 13.11.2023. URL: https://thredds.met.no/thredds/catalog.html.

Micheletti, N. et al. (2014). 'Machine learning feature selection methods for landslide susceptibility mapping'. In: *Mathematical geosciences* 46, pp. 33–57.

Molnar, C. (2020). *Interpretable machine learning*. Lulu. com.

Mondini, A. C., Guzzetti, F. and Melillo, M. (2023). 'Deep learning forecast of rainfall-induced shallow landslides'. In: *Nature communications* 14.1, p. 2466.

Nahm, F. S. (2022). 'Receiver operating characteristic curve: overview and practical use for clinicians'. In: *Korean journal of anesthesiology* 75.1, p. 25.

NationalGeographic (2023). *Köppen Climate Classification System*. Accessed on 30.11.2023. URL: https://education.nationalgeographic.org/resource/koppen-climate-classification-system/.

Navlani, A. (2019). *Understanding Logistic Regression in Python Tutorial*. Accessed on 05.03.2024. URL: https://www.datacamp.com/tutorial/understanding-logistic-regression-python.

— (2023). *Decision Tree Classification in Python Tutorial*. Accessed on 01.03.2024. URL: https://www.datacamp.com/tutorial/decision-tree-classification-python.

Ng, C. W. W. et al. (2021). 'Spatiotemporal modelling of rainfall-induced landslides using machine learning'. In: *Landslides* 18.7, pp. 2499–2514.

NGI (2014). *SKRED - skredfare og sikringstiltak*. Universitetsforlaget.

Ngo, P. T. T. et al. (2021). 'Evaluation of deep learning algorithms for national scale landslide susceptibility mapping of Iran'. In: *Geoscience Frontiers* 12.2, pp. 505–519.

NGU (2023). *Geologisk kart*. Accessed on 13.09.2023. URL: https://www.ngu.no/geologiske-kart.

— (n.d.). *Kvartærgeologisk kartlegging*. Accessed on 04.12.2023. URL: https://www.ngu.no/geologisk-kartlegging/kvartaergeologisk-kartlegging.

Nguyen, V. V. et al. (2019). 'Hybrid machine learning approaches for landslide susceptibility modeling'. In: *Forests* 10.2, p. 157.

NIBIO (2023). *Produktark: Skogressurskartet SR16*. Product Sheet. https://www.nibio.no/tema/skog/kart-over-skogressurser/skogressurskart-sr16.

— (n.d.). *Treslag i Norge*. Accessed on 15.03.2024. URL: https://www.nibio.no/tema/skog/skoggenetiske-ressurser/treslag-i-norge.

Nocentini, N. et al. (2023). 'Towards landslide space-time forecasting through machine learning: the influence of rainfall parameters and model setting'. In: *Frontiers in Earth Science* 11, p. 1152130.

NVE (2018). *Produktark: Skredhendelser*. Product Sheet. https://www.nve.no/kart/.

— (2022). *Om skred*. Accessed on 30.11.2023. URL: https://www.nve.no/naturfare/laer-om-naturfare/om-skred/.

NVE (2023a). *Skredhendelser*. Accessed on 18.09.2023. URL: https://temakart.nve.no/tema/skredhendelser.

— (2023b). *Veileder for utredning av sikkerhet mot skred i bratt terreng*. Accessed on 11.12.2023. URL: https://www.nve.no/veileder-skredfareutredning-bratt-terreng.

Nystuen, J. P. (2013). 'Jorda skifter ansikt - geologiske prosesser'. In: *Landet blir til - Norges geologi*. Ed. by I.B. Ramberg et al. 2nd ed. Trondheim: Norsk Geologisk Forening, p. 656.

O'brien, R. M. (2007). 'A caution regarding rules of thumb for variance inflation factors'. In: *Quality and quantity* 41, pp. 673–690.

Pedersen, S. et al. (Jan. 2024). *Ansvar, Finansiering og Insentiver: Utredning av Virkemidler for Økt Forebygging mot Vær- og Naturfare i Norge*. 4/2024. With contributions from Finans Norge and Fremtind. Menon Economics.

Planteportalen (n.d.). *bjørk (art)*. Accessed on 22.04.2023. URL: https://planteportalen.no/lovtraer/hengebjork/.

Pourghasemi, H. R. et al. (2020). 'Investigating the effects of different landslide positioning techniques, landslide partitioning approaches, and presence-absence balances on landslide susceptibility mapping'. In: *Catena* 187, p. 104364.

Pradhan, A. M. S., Lee, S-R. and Kim, Y-T. (2019). 'A shallow slide prediction model combining rainfall threshold warnings and shallow slide susceptibility in Busan, Korea'. In: *Landslides* 16, pp. 647–659.

Python (n.d.). *What is Python? Executive Summary*. Accessed on 05.03.2024. URL: https://www.python.org/doc/essays/blurb/.

Ramberg, I. B. et al. (2006). 'Landet blir til'. In: *Norges geologi: Norsk Geologisk Forening, Trondheim*.

Ravindranath, N.H. and Ostwald, M. (2008). 'Methods for below-ground biomass'. In: *Carbon inventory methods handbook for greenhouse gas inventory, carbon mitigation and roundwood production projects*, pp. 149–156.

Reichenbach, P. et al. (2018). 'A review of statistically-based landslide susceptibility models'. In: *Earth-Science Reviews* 180, pp. 60–91. DOI: https://doi.org/10.1016/j.earscirev.2018.03.001.

Ren, T., Gao, L. and Gong, W. (2024). 'An ensemble of dynamic rainfall index and machine learning method for spatiotemporal landslide susceptibility modeling'. In: *Landslides* 21.2, pp. 257–273.

Revheim-Rafaelsen, M. et al. (2023). *Så raset velte mot huset: – Helt surrealistisk*. Accessed on 13.11.2023. URL: https://www.nrk.no/norge/nesten-2900-evakuert-etter-_hans__-_-en-krisesituasjon-1.16509958.

Rickli, C. and Graf, F. (2009). 'Effects of forests on shallow landslides–case studies in Switzerland'. In: *Forest Snow and Landscape Research* 82.1, pp. 33–44.

Romundset, A. et al. (2023). 'Early Holocene thinning and final demise of the Scandinavian Ice Sheet across the main drainage divide of southern Norway'. In: *Quaternary Science Reviews* 317, p. 108274.

Ruth, K. (2024). *Verdien av forebygging, og hva koster det om vi ikke gjør det?* PowerPoint presentation. Presented at "I hardt vær"' Conference, Oslo, May, 2024.

Ruther, D. C., Hefre, H. and Rubensdotter, B.L.E.F (2022). 'Extreme precipitation-induced landslide event on 30th July 2019 in Jølster, western Norway'. In.

Rüther, D. C., Lindsay, E. and Slåtten, M. S. (2024). *Landslide inventory:'Hans' storm southern Norway, August 7–9, 2023*.

Saito, H. et al. (2017). 'Effect of forest clear-cutting on landslide occurrences: Analysis of rainfall thresholds at Mt. Ichifusa, Japan'. In: *Geomorphology* 276, pp. 1–7.

Sandersen, F. et al. (1997). 'The influence of meteorological factors on the initiation of debris flows, rockfalls, rockslides and rockmass stability'. In: *Publikasjon-Norges Geotekniske Institutt* 201, pp. 97–114.

Schmidt, K.M. et al. (2001). 'The variability of root cohesion as an influence on shallow landslide susceptibility in the Oregon Coast Range'. In: *Canadian Geotechnical Journal* 38.5, pp. 995–1024.

Schuster, R. L. and Wieczorek, G. F. (2018). 'Landslide triggers and types'. In: *Landslides*, pp. 59–78.

ScikitLearn (n.d.[a]). *Feature importances with a forest of trees*. Accessed on 26.04.2024. URL: https://scikit-learn.org/stable/auto_examples/ensemble/plot_forest_importances.html.

— (n.d.[b]). *LogisticRegression*. Accessed on 29.05.2024. URL: https://scikit-learn.org/stable/modules/generated/sklearn.linear_model.LogisticRegression.html.

ScikitLearn (n.d.[c]). *RandomForestClassifier*. Accessed on 06.03.2024. URL: https://scikit-learn.org/stable/modules/generated/sklearn.ensemble.RandomForestClassifier.html.

— (n.d.[d]). *User Guide - 3. Model selection and evaluation*. Accessed on 5.06.2024. URL: https://scikit-learn.org/stable/modules/cross_validation.html#cross-validation.

Segoni, S. et al. (2018). 'Combination of rainfall thresholds and susceptibility maps for dynamic landslide hazard assessment at regional scale'. In: *Frontiers in Earth Science* 6, p. 85.

SeNorge (2023). *Temperatur/Nedbør 1991-2020*. Accessed on 13.11.2023. URL: https://senorge.no/.

— (n.d.). *Water related maps*. Accessed on 05.12.2023. URL: https://www.senorge.no/WaterMap?lang=en.

Shafi, A. (2023). *Random Forest Classification with Scikit-Learn*. Accessed on 01.03.2024. URL: https://www.datacamp.com/tutorial/random-forests-classifier-python.

Shen, P. et al. (2017). 'Role of vegetation restoration in mitigating hillslope erosion and debris flows'. In: *Engineering Geology* 216, pp. 122–133.

Shin, T. (2023). *Understanding Feature Importance in Machine Learning*. Accessed on 26.04.2024. URL: https://builtin.com/data-science/feature-importance.

Sidle, R. C. et al. (2006). 'Erosion processes in steep terrain—Truths, myths, and uncertainties related to forest management in Southeast Asia'. In: *Forest ecology and management* 224.1-2, pp. 199–225.

Smith, A. (2020). 'Characterizing individual tree biomass for improved biomass estimation in Norwegian forests'. In.

Smolic, H. (2023). *A Comprehensive Guide to Random Forest: How It Works and Its Applications*. Accessed on 26.02.2024. URL: https://graphite-note.com/a-comprehensive-guide-to-random-forest-how-it-works-and-its-applications.

StatensKartverk (2018). *Produktspesifikasjon, Nasjonal modell for høydedata fra laserskanning (FKB-Laser)*. Accessed on 05.12.2023. URL: https://register.geonorge.no/data/documents/Produktspesifikasjoner_FKB-Laser_v1_fkb-laser-v30-2018-01-01_.pdf.

Su, C. et al. (2023). 'Improved landslide susceptibility mapping using unsupervised and supervised collaborative machine learning models'. In: *Georisk: Assessment and Management of Risk for Engineered Systems and Geohazards* 17.2, pp. 387–405.

Sun, D. et al. (2020). 'An optimized random forest model and its generalization ability in landslide susceptibility mapping: application in two areas of Three Gorges Reservoir, China'. In: *Journal of Earth Science* 31, pp. 1068–1086.

Sunding, P., Larsen, Ø. and Aune, E. (2024). *furu*. Accessed on 26.02.2024. URL: https://snl.no/furu.

Taalab, K., Cheng, T. and Zhang, Y. (2018). 'Mapping landslide susceptibility and types using Random Forest'. In: *Big Earth Data* 2.2, pp. 159–178.

Tavasoli, S. (2024). *Top 10 Machine Learning Algorithms For Beginners: Supervised, and More*. Accessed on 06.03.2024. URL: https://www.simplilearn.com/10-algorithms-machine-learning-engineers-need-to-know-article.

Tehrani, F. S. et al. (2022). 'Machine learning and landslide studies: recent advances and applications'. In: *Natural Hazards* 114.2, pp. 1197–1245.

Tenge, I. (2016). *Arealressurskart AR5*. Brochure. http://hdl.handle.net/11250/2415670.

Terzaghi, K., Peck, R. B. and Mesri, G. (1996). *Soil mechanics in engineering practice*. John wiley and sons.

Thorsnæs, G. (2023). *Gudbrandsdalen*. Accessed on 27.09.2023. URL: https://snl.no/Gudbrandsdalen.

Tofani, V. et al. (2017). 'Soil characterization for shallow landslides modeling: a case study in the Northern Apennines (Central Italy)'. In: *Landslides* 14, pp. 755–770.

Torkelsen, E. et al. (2023). *Kommunene får 1,7 milliarder etter ekstremværet «Hans»: – Gladmelding*. Accessed on 26.04.2024. URL: https://www.nrk.no/norge/regjeringen-bevilger-1_7-milliarder-kroner-til-kommunene-etter-ekstremvaeret-_hans_-1.16649493.

Vakhshoori, V. et al. (2019). 'Landslide susceptibility mapping using GIS-based data mining algorithms'. In: *Water* 11.11, p. 2292.

Varnes, D. J. (1978). 'Slope movement types and processes'. In: *Special report* 176, pp. 11–33.

Vorren, T. and Mangerud, J. (2013). 'Istider kommer og går'. In: *Landet blir til - Norges geologi*. Ed. by I.B. Ramberg et al. 2nd ed. Trondheim: Norsk Geologisk Forening, p. 656.

Wang, Y., Fang, Z. and Hong, H. (2019). 'Comparison of convolutional neural networks for landslide susceptibility mapping in Yanshan County, China'. In: *Science of the total environment* 666, pp. 975–993.

Wang, Y., Wen, H. et al. (2021). 'Quantitative assessment of landslide risk based on susceptibility mapping using random forest and geodetector'. In: *Remote Sensing* 13.13, p. 2625.

Wieczorek, G. F. and Glade, T. (2005). 'Climatic factors influencing occurence of debris flows'. In: *Springer Berlin Heidelberg* 8, pp. 325–362. DOI: 10.1007/3-540-27129-5_14.

Wu, T. H., McKinnell III, W. P. and Swanston, D. N. (1979). 'Strength of tree roots and landslides on Prince of Wales Island, Alaska'. In: *Canadian Geotechnical Journal* 16.1, pp. 19–33.

Wubalem, A. (2021). 'Landslide susceptibility mapping using statistical methods in Uatzau catchment area, northwestern Ethiopia'. In: *Geoenviron Disasters* 8. DOI: https://doi.org/10.1186/s40677-020-00170-y.

Xgeo (n.d.). https://www.xgeo.no/. Accessed: 23.04.2024.

Yang, C et al. (2023). 'Machine learning-based landslide susceptibility assessment with optimized ratio of landslide to non-landslide samples'. In: *Gondwana Research* 123, pp. 198–216.

Yao, J. et al. (2023). 'Performance comparison of landslide susceptibility mapping under multiple machine-learning based models considering InSAR deformation: A case study of the upper Jinsha River'. In: *Geomatics, Natural Hazards and Risk* 14.1, p. 2212833.

Youssef, A. M. and Pourghasemi, H. R. (2021). 'Landslide susceptibility mapping using machine learning algorithms and comparison of their performance at Abha Basin, Asir Region, Saudi Arabia'. In: *Geoscience Frontiers* 12.2, pp. 639–655.

Zhang, L., Yan, W. M. and Leung, F. T. Y. (2021). 'Probabilistic estimation of root cohesion in regards to intra-specific variability of root system'. In: *Catena* 196, p. 104898.

Zhang, T. et al. (2022). ‘Evaluation of different machine learning models and novel deep learning-based algorithm for landslide susceptibility mapping’. In: *Geoscience Letters* 9.1, p. 26.

Zhou, C. et al. (2018). ‘Landslide susceptibility modeling applying machine learning methods: A case study from Longju in the Three Gorges Reservoir area, China’. In: *Computers and geosciences* 112, pp. 23–37.

Ziemer, R. R. (Jan. 1981a). ‘Roots and the Stability of Forested Slopes’. In: vol. 132.

— (1981b). ‘The role of vegetation in the stability of forested slopes’. In: 1, pp. 297–308.

8 Appendix

Figures from the "Engineering geology, Specialization Project", TGB 4575 are placed here in the Appendix in addition to more frequency and landslide plots. This is because the figures are relevant for this study as well, but not directly corresponding to answering the research questions. Further information regarding the figures is found in Hågensen (2023).

8.1 Study area with 4 points

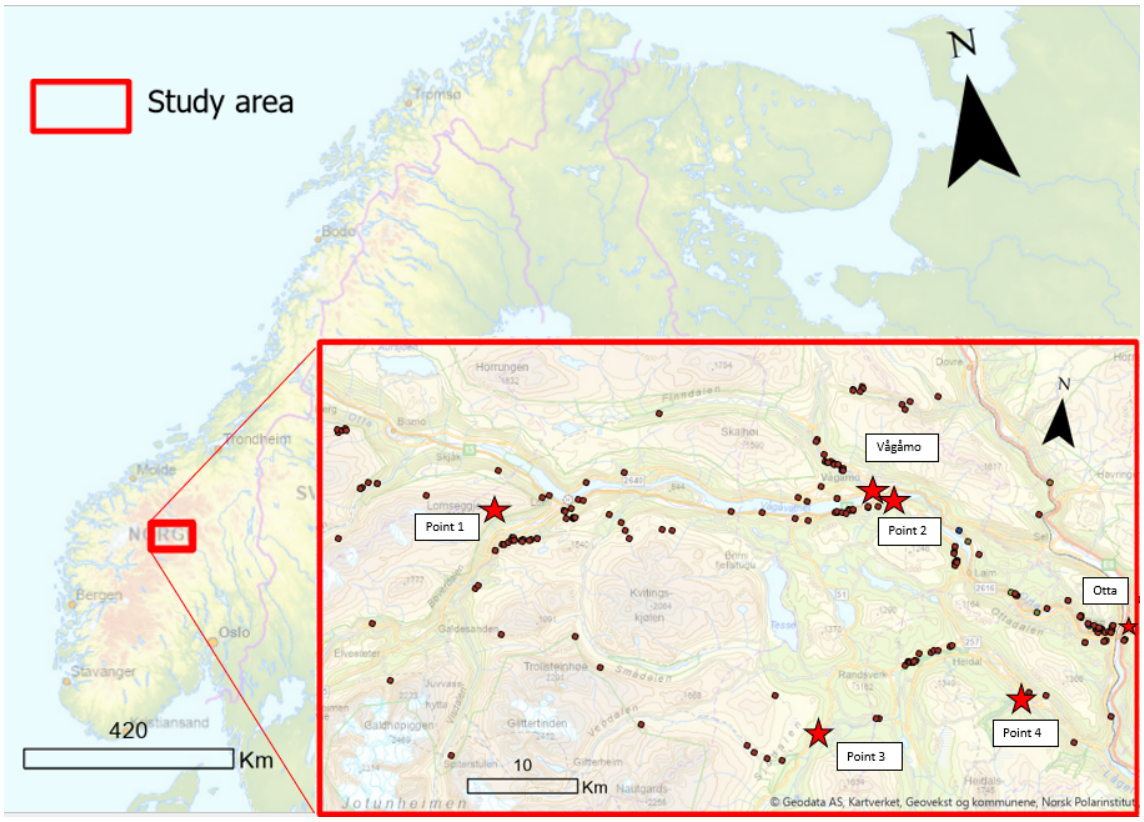

Figure 27: Map of the study area. The study area is in Ottadalen, indicated by the red square. The brown dots are release points of landslides. North arrow and scale bar is added to both maps. Vågåmo, Otta and point 1-4 is marked with a red star. This is because the locations and points are used later in the report. The background map is the OpenStreetMap from ArcGIS.

8.2 Analysis of landslide inventory data and terrain conditions

Table 18: Different landslide types that initiated inside the study area. The landslide types and amount was extracted from the landslide inventory. The landslide types are also classified in Hungr et al. (2013).

Landslide types	Amount
Debris flow	134
Debris slide	48
Debris avalanche	23
Debris flood	4
Landslide, unspecified	21
Total	230

(a)

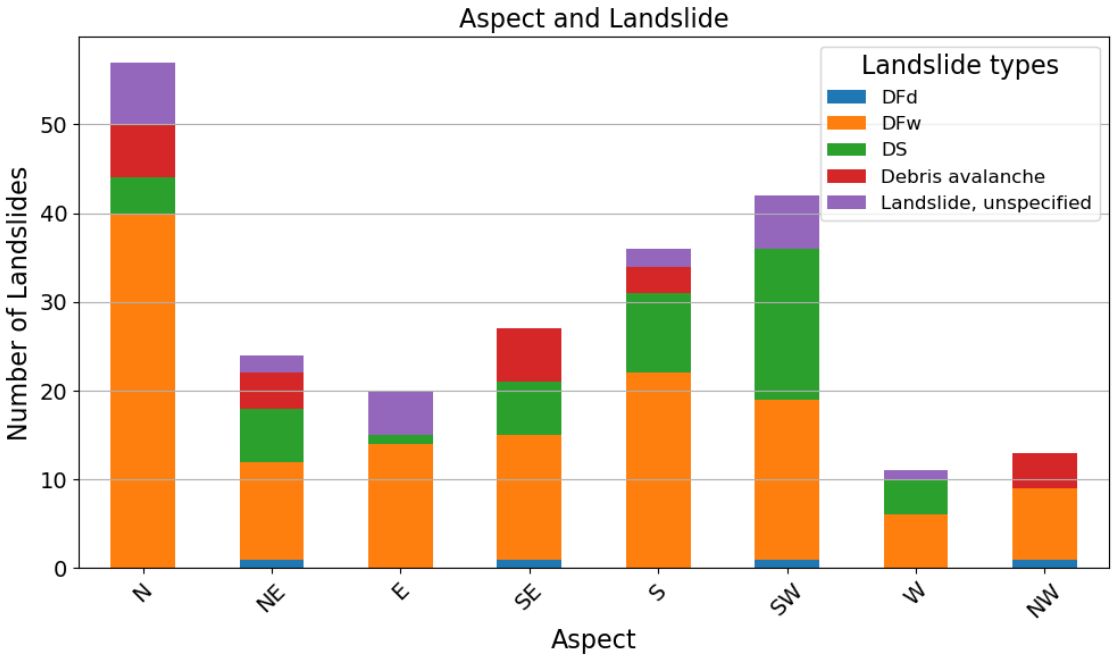

(b)

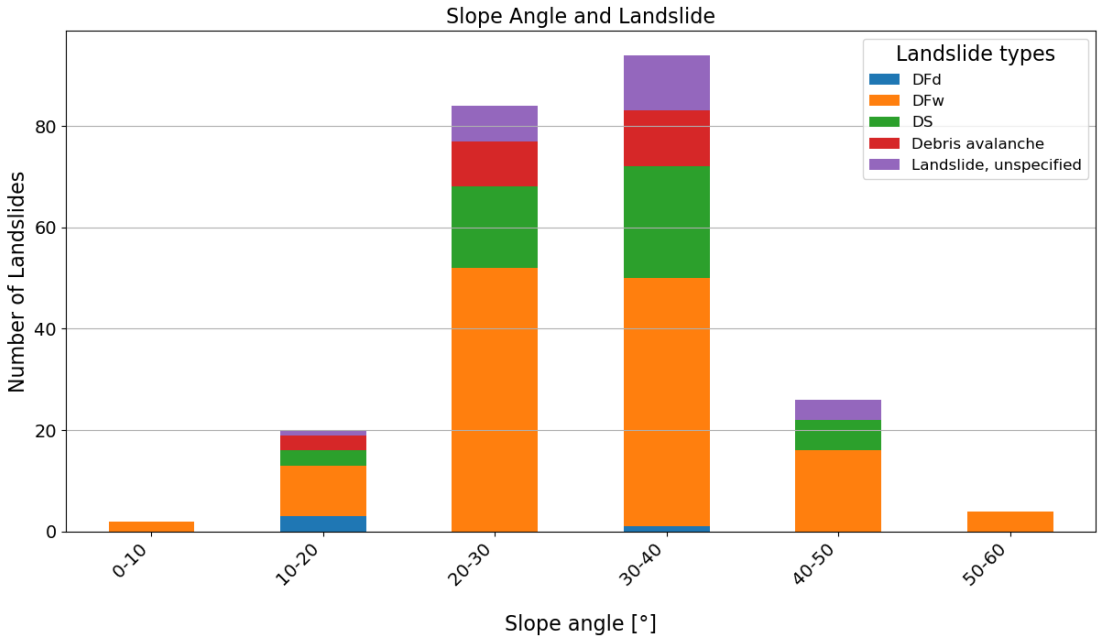

Figure 28: Stack bar showing amount and type of landslides based on slope aspect or slope angle. Abbreviations: DFd - debris flood, DFw - debris flow, DS - debris slide. Overview of aspect division is found in Table 7.

(a)

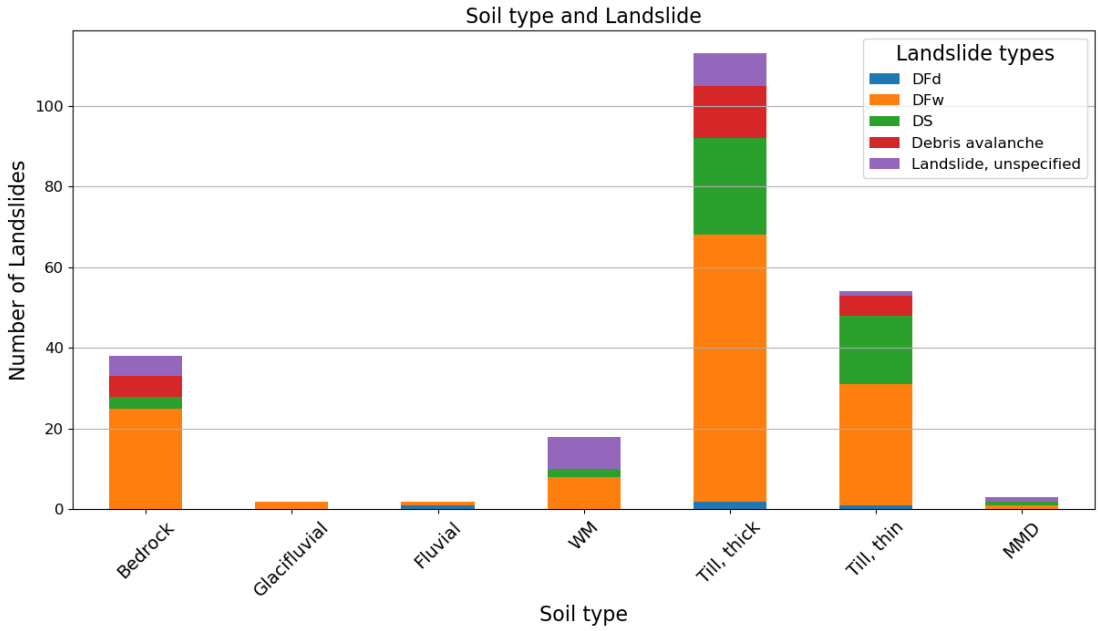

(b)

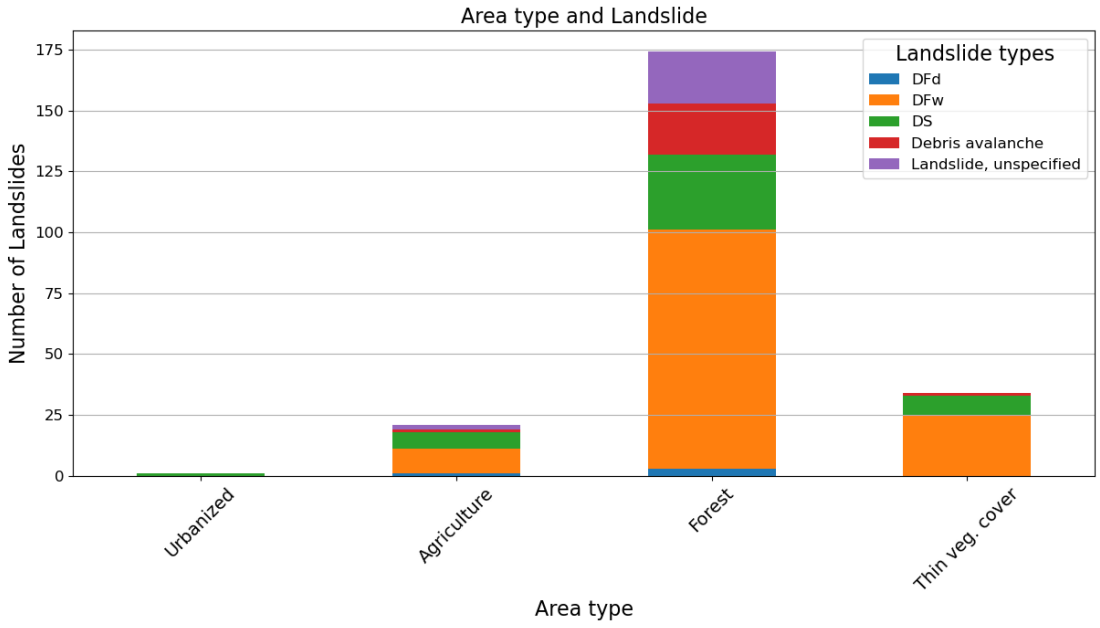

Figure 29: Stack bar showing amount and type of landslides based on soil type or area type. Abbreviations: DFd - debris flood, DFw - debris flow, DS - debris slide, WM - weathered material, MMD - mass movement deposits, Thin veg. cover - thin vegetation cover.

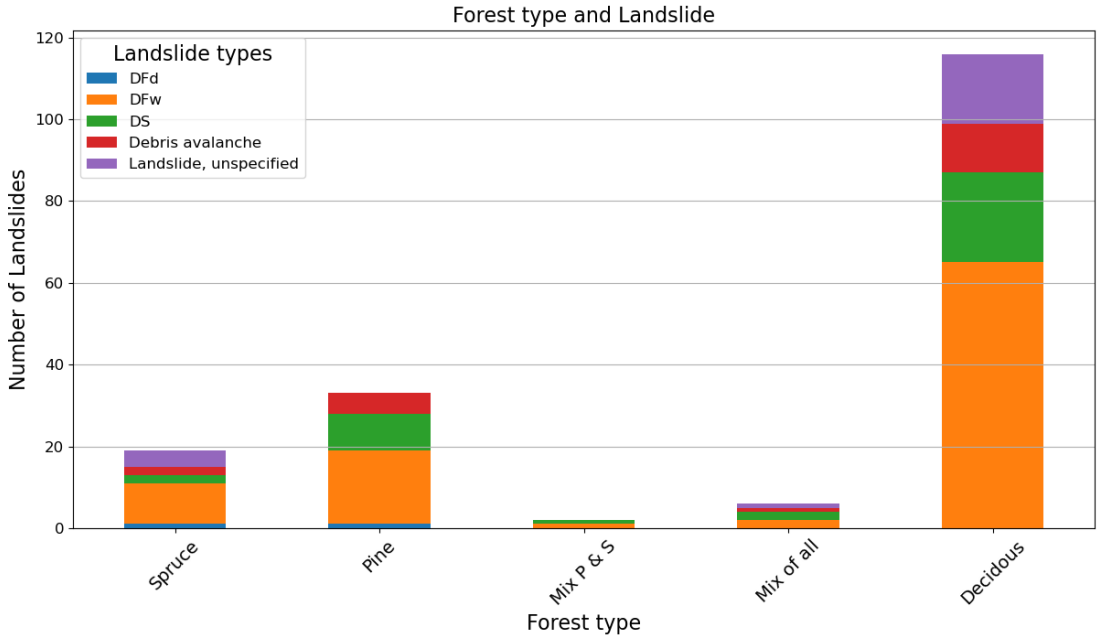

Figure 30: Stack bar showing amount and type of landslides based on forest type. Abbreviations: DFd - debris flood, DFw - debris flow, DS - debris slide, Mix P & S - mix of pine and spruce.

Table 19 is showing the frequency of landslides and is generated from Equation 6. “Class 1” and “Area 1” in Equation 6 refers to the different rows under column “LULC”, “Soil type” or “Forest type” in Table 19. Equation 7 gives an example of the determination of landslide frequency in thick till.

$$\text{Frequency} = \frac{\left(\frac{113}{230}\right)}{\left(\frac{1222.34}{3070.85}\right)} = 1.23 \tag{7}$$

Table 19: The frequency of landslides is shown for LULC, soil type and forest type.

LULC; Frequency	Soil type; Frequency	Forest type; Frequency
Forest; 2.53	Till, thick; 1.23	Deciduous; 4.48
Thin vegetation cover; 0.29	Till, thin; 0.75	Pine; 1.12
Agriculture; 1.96	Bedrock; 0.91	Spruce; 2.05
Urbanized; 0.88	Weathered material; 5.33	Mix of all; 3.48
	Glacifluvial; 0.32	Mix of pine and spruce; 1.17
	Fluvial; 0.36	
	Mass movement deposits; 1.49	

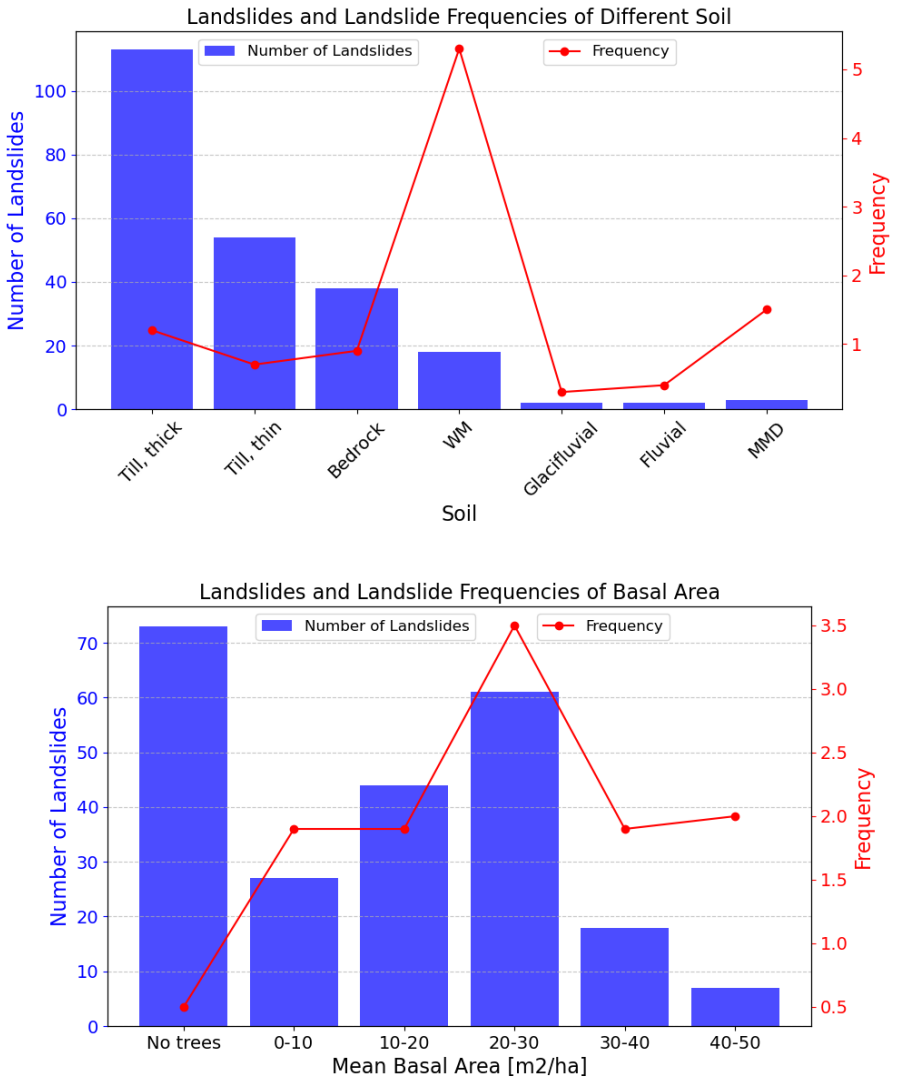

Figure 31: Graphs showing landslide amount and landslide frequencies of soil type and tree basal area at breast height. Blue bars are showing the amount of landslides and the red line is showing the frequency of the landslides.

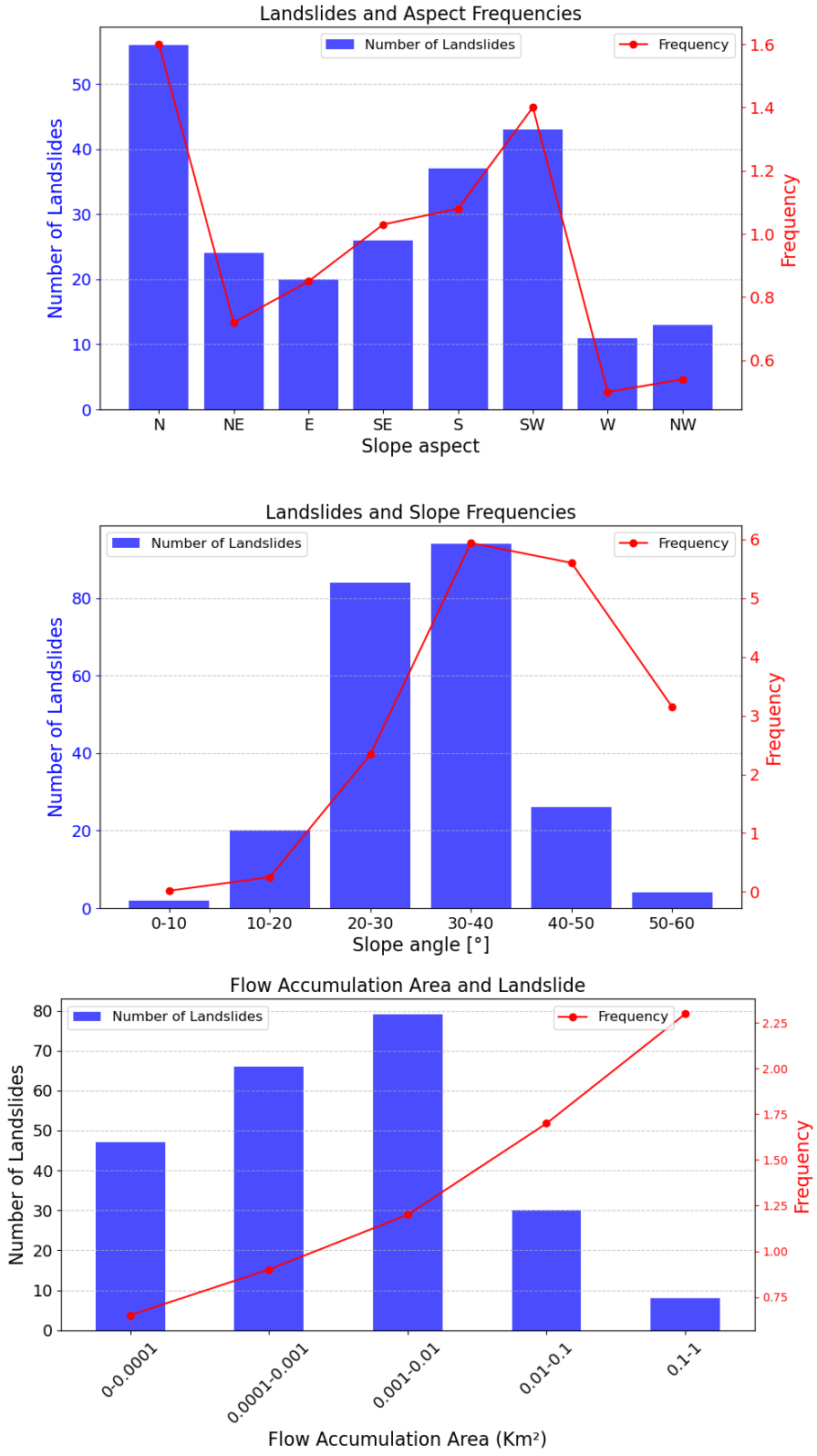

Figure 32: Graphs showing landslide amount and landslide frequencies of slope aspect, slope angle and flow accumulation. Blue bars are showing the amount of landslides and the red line is showing the frequency of the landslides.

8.3 Analysis of the hydrometeorological conditions leading to landslides

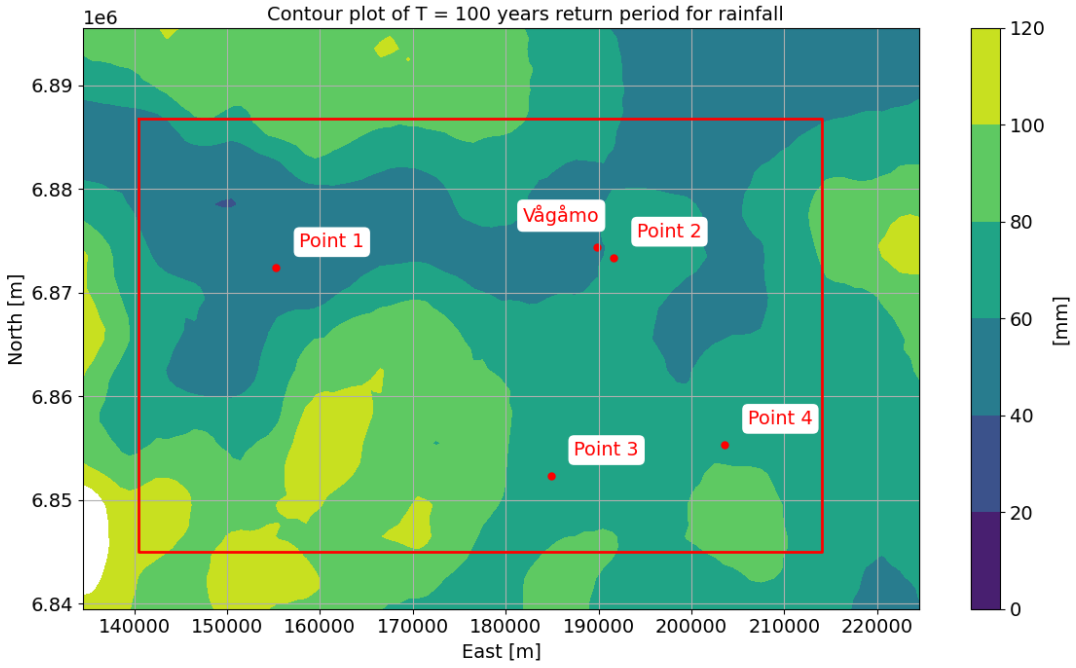

Figure 33: Figure showing the 100 year return period for a duration of 24 hours in the study area. The four NGI points and Vågåmo is marked as red dots and can also be seen in Figure 27. The red square is the study area. Northing and easting are shown on the y- and x- axis, respectively. Amount of precipitation [mm] is shown in the colorbar.

(a)

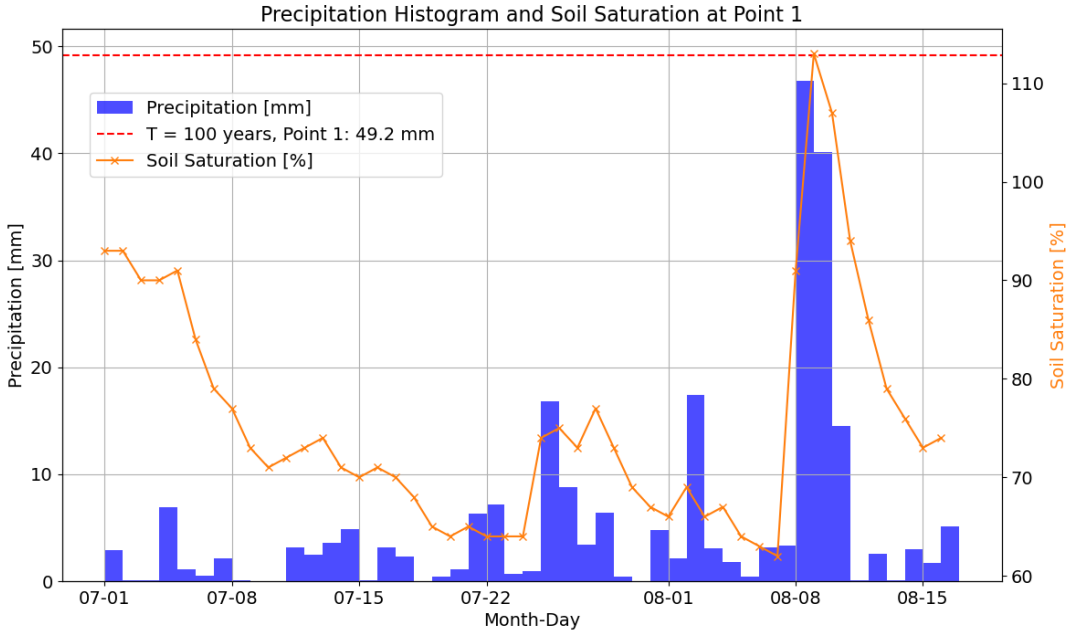

(b)

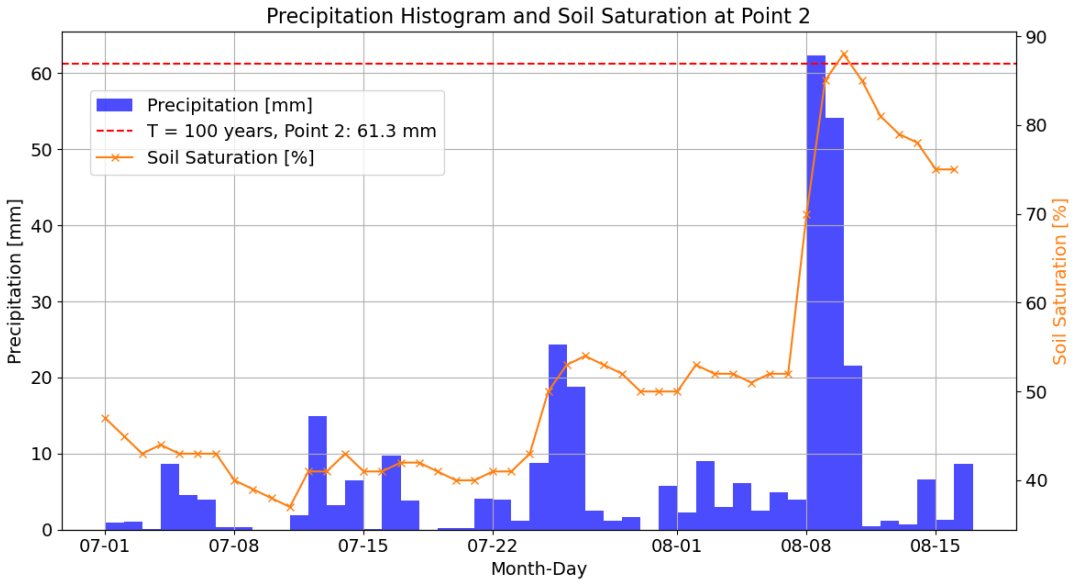

Figure 34: Figure showing precipitation in mm as histograms, soil saturation degree in % as orange line and the T = 100 years as a red, dotted line which indicates the 100 year return period for the specific point. The time period is starting from 1 July and going until 16 August 2023 at 24 hours. Time is spanning from 00:00 until 24:00 for each day. The plots are representing points 1 and 2 from Figure 33.

(a)

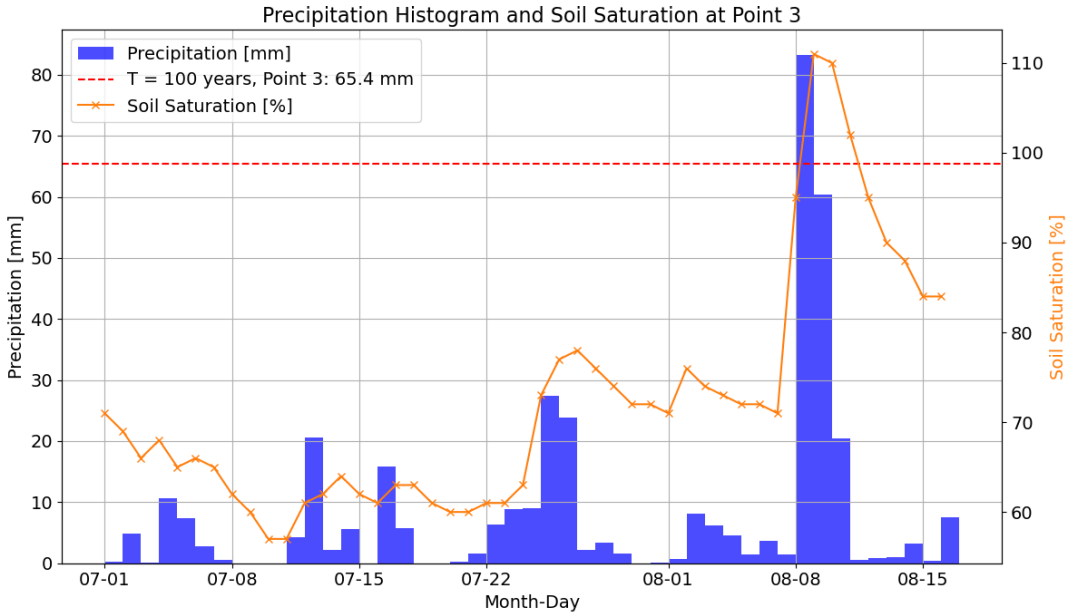

(b)

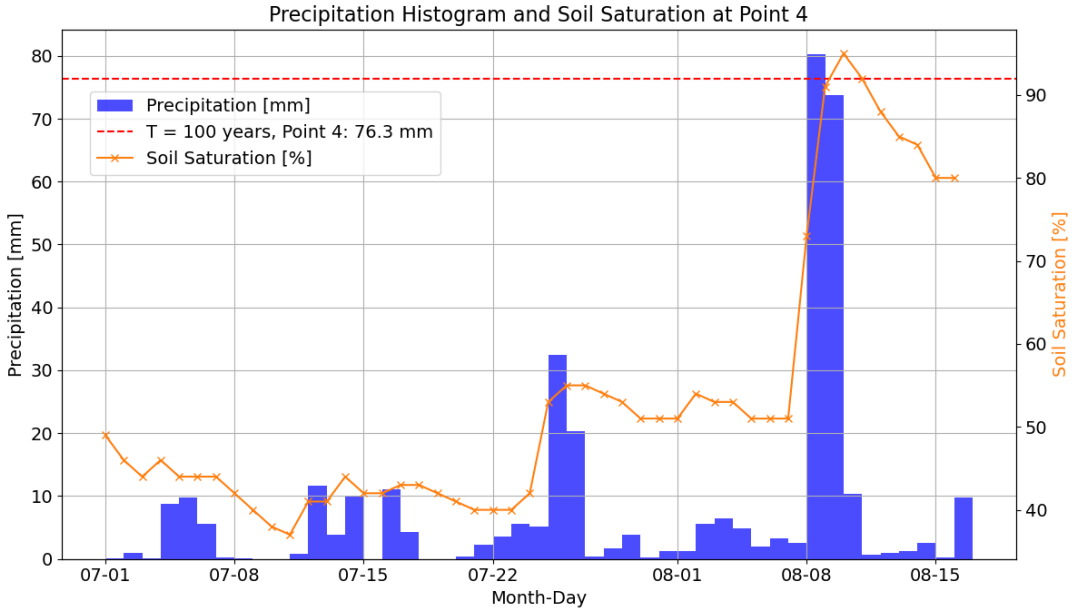

Figure 35: Figure showing precipitation in mm as histograms, soil saturation degree in % as orange line and the T = 100 years as a red, dotted line which indicates the 100 year return period for the specific point. The time period is starting from 1 July and going until 16 August 2023. Time is spanning from 00:00 until 24:00 for each day. The plots are representing points 3 and 4 from Figure 33.

Figure 36: Soil legend from NGU part 1

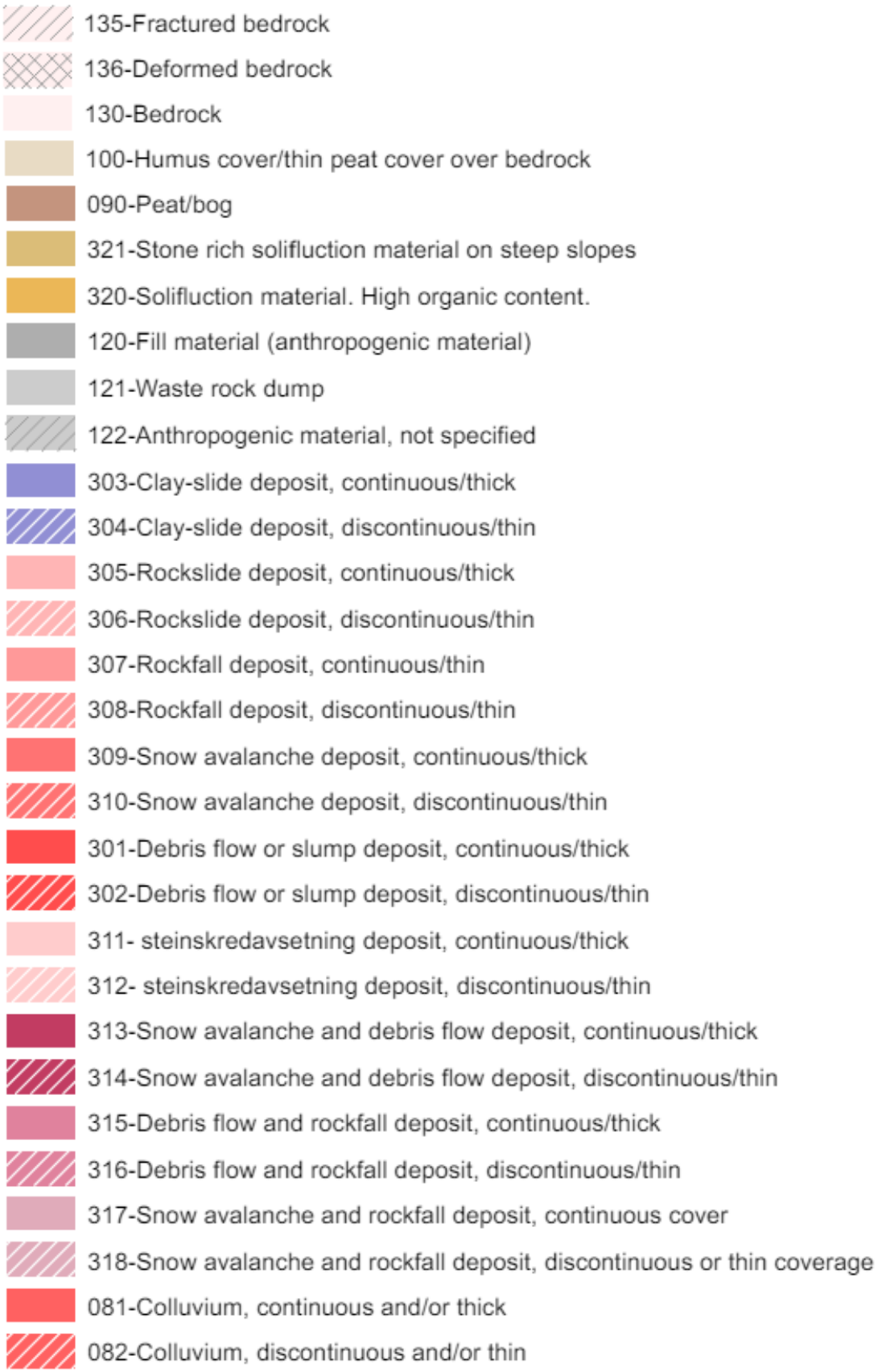

Figure 37: Soil legend from NGU part 2

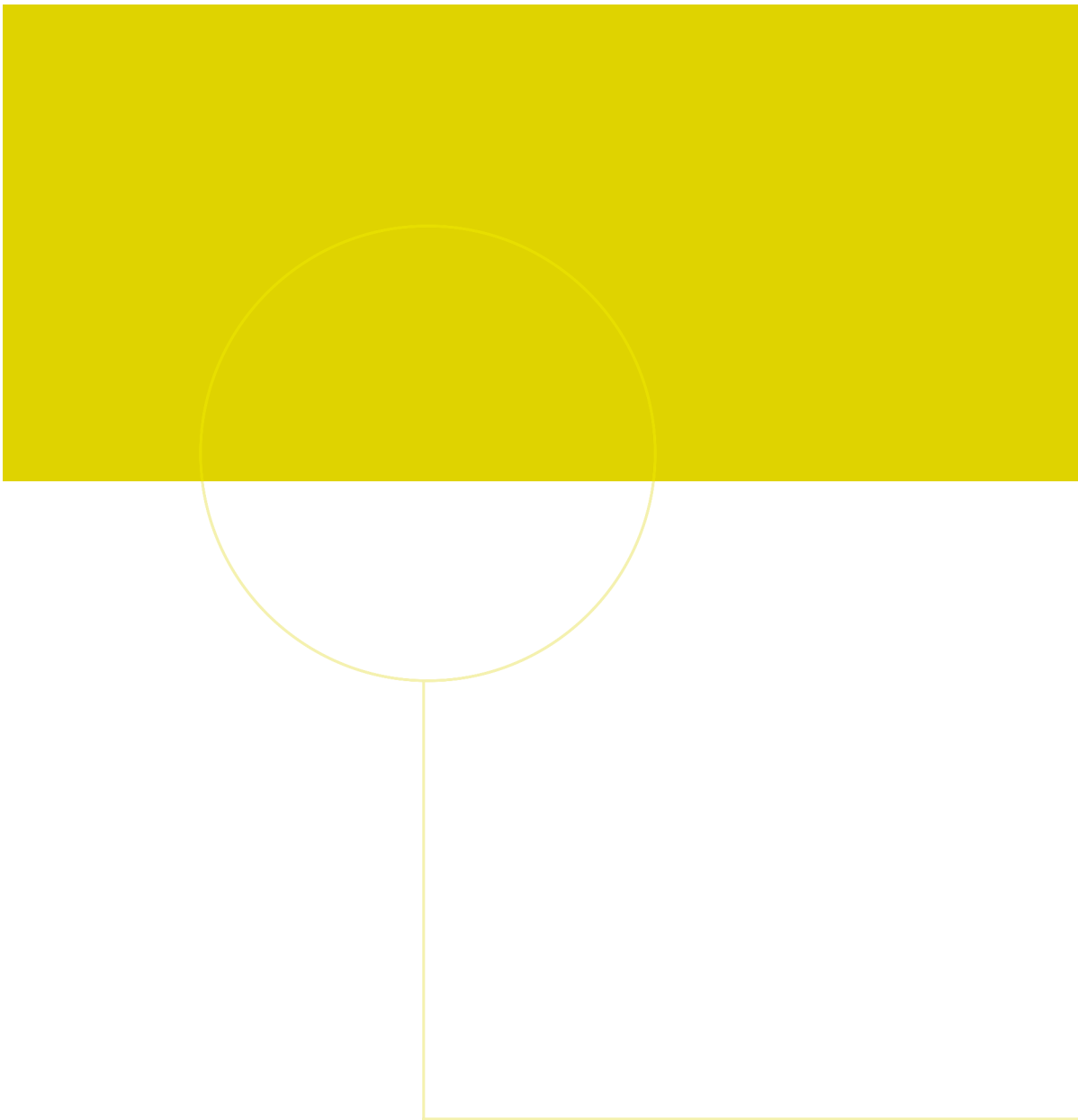

NTNU

Norwegian University of
Science and Technology